Progress in Materials Science 61 (2014) 1–93

Contents lists available at ScienceDirect

Progress in Materials Science

journal homepage: www.elsevier.com/locate/pmatsci

Microstructures and properties of high-entropy alloys

Yong Zhang [a,*], Ting Ting Zuo [a], Zhi Tang [b], Michael C. Gao [c,d], Karin A. Dahmen [e], Peter K. Liaw [b], Zhao Ping Lu [a]

[a] State Key Laboratory for Advanced Metals and Materials, University of Science and Technology Beijing, Beijing 100083, China
[b] Department of Materials Science and Engineering, The University of Tennessee, Knoxville, TN 37996, USA
[c] National Energy Technology Laboratory, 1450 Queen Ave SW, Albany, OR 97321, USA
[d] URS Corporation, PO Box 1959, Albany, OR 97321-2198, USA
[e] Department of Physics, University of Illinois at Urbana-Champaign, 1110 West Green Street, Urbana, IL 61801-3080, USA

ARTICLE INFO

Article history:
Received 26 September 2013
Accepted 8 October 2013
Available online 1 November 2013

ABSTRACT

This paper reviews the recent research and development of high-entropy alloys (HEAs). HEAs are loosely defined as solid solution alloys that contain more than five principal elements in equal or near equal atomic percent (at.%). The concept of high entropy introduces a new path of developing advanced materials with unique properties, which cannot be achieved by the conventional micro-alloying approach based on only one dominant element. Up to date, many HEAs with promising properties have been reported, e.g., high wear-resistant HEAs, $Co_{1.5}CrFeNi_{1.5}Ti$ and $Al_{0.2}Co_{1.5}CrFeNi_{1.5}Ti$ alloys; high-strength body-centered-cubic (BCC) AlCoCrFeNi HEAs at room temperature, and NbMoTaV HEA at elevated temperatures. Furthermore, the general corrosion resistance of the $Cu_{0.5}NiAlCoCrFeSi$ HEA is much better than that of the conventional 304-stainless steel. This paper first reviews HEA formation in relation to thermodynamics, kinetics, and processing. Physical, magnetic, chemical, and mechanical properties are then discussed. Great details are provided on the plastic deformation, fracture, and magnetization from the perspectives of crackling noise and Barkhausen noise measurements, and the analysis of serrations on stress–strain curves at specific strain rates or testing temperatures, as well as the serrations of the magnetization hysteresis loops. The comparison between conventional and high-entropy bulk metallic glasses is analyzed from the viewpoints of eutectic composition, dense atomic packing, and entropy of

* Corresponding author. Tel.: +86 010 62333073; fax: +86 010 62333447.
E-mail address: drzhangy@ustb.edu.cn (Y. Zhang).

0079-6425/$ - see front matter © 2013 Elsevier Ltd. All rights reserved.
http://dx.doi.org/10.1016/j.pmatsci.2013.10.001

mixing. Glass forming ability and plastic properties of high-entropy bulk metallic glasses are also discussed. Modeling techniques applicable to HEAs are introduced and discussed, such as *ab initio* molecular dynamics simulations and CALPHAD modeling. Finally, future developments and potential new research directions for HEAs are proposed.

© 2013 Elsevier Ltd. All rights reserved.

Contents

1. Introduction . . . 3
   1.1. Four core effects . . . 4
      1.1.1. High-entropy effect . . . 4
      1.1.2. Sluggish diffusion effect . . . 5
      1.1.3. Severe lattice-distortion effect . . . 6
      1.1.4. Cocktail effect . . . 7
   1.2. Key research topics . . . 9
      1.2.1. Mechanical properties compared with other alloys . . . 10
      1.2.2. Underlying mechanisms for mechanical properties . . . 11
      1.2.3. Alloy design and preparation for HEAs . . . 11
      1.2.4. Theoretical simulations for HEAs . . . 12
2. Thermodynamics . . . 12
   2.1. Entropy . . . 13
   2.2. Thermodynamic considerations of phase formation . . . 15
   2.3. Microstructures of HEAs . . . 18
3. Kinetics and alloy preparation . . . 23
   3.1. Preparation from the liquid state . . . 24
   3.2. Preparation from the solid state . . . 29
   3.3. Preparation from the gas state . . . 30
   3.4. Electrochemical preparation . . . 34
4. Properties . . . 34
   4.1. Mechanical behavior . . . 34
      4.1.1. Mechanical behavior at room temperature . . . 35
      4.1.2. Mechanical behavior at elevated temperatures . . . 38
      4.1.3. Mechanical behavior at cryogenic temperatures . . . 45
      4.1.4. Fatigue behavior . . . 46
      4.1.5. Wear behavior . . . 48
      4.1.6. Summary . . . 49
   4.2. Physical behavior . . . 50
   4.3. Biomedical, chemical and other behaviors . . . 53
5. Serrations and deformation mechanisms . . . 55
   5.1. Serrations for HEAs . . . 56
   5.2. Barkhausen noise for HEAs . . . 58
   5.3. Modeling the Serrations of HEAs . . . 61
   5.4. Deformation mechanisms for HEAs . . . 66
6. Glass formation in high-entropy alloys . . . 67
   6.1. High-entropy effects on glass formation . . . 67
      6.1.1. The best glass former is located at the eutectic compositions . . . 67
      6.1.2. The best glass former is the composition with dense atomic packing . . . 67
      6.1.3. The best glass former has high entropy of mixing . . . 67
   6.2. GFA for HEAs . . . 68
   6.3. Properties of high-entropy BMGs . . . 70
7. Modeling and simulations . . . 72
   7.1. DFT calculations . . . 73
   7.2. AIMD simulations . . . 75
   7.3. CALPHAD modeling . . . 80
8. Future development and research . . . 81

8.1. Fundamental understanding of HEAs . . . 82
8.2. Processing and characterization of HEAs . . . 83
8.3. Applications of HEAs . . . 83
9. Summary . . . 84
Disclaimer . . . 85
Acknowledgements . . . 85
References . . . 85

1. Introduction

Recently, high-entropy alloys (HEAs) have attracted increasing attentions because of their unique compositions, microstructures, and adjustable properties [1–31]. They are loosely defined as solid solution alloys that contain more than five principal elements in equal or near equal atomic percent (at.%) [32]. Normally, the atomic fraction of each component is greater than 5 at.%. The multi-component equi-molar alloys should be located at the center of a multi-component phase diagram, and their configuration entropy of mixing reaches its maximum ($R\,\mathrm{Ln}\,N$; R is the gas constant and N the number of component in the system) for a solution phase. These alloys are defined as HEAs by Yeh et al. [2], and named by Cantor et al. [1,33] as multi-component alloys. Both refer to the same concept. There are also some other names, such as multi-principal-elements alloys, equi-molar alloys, equi-atomic ratio alloys, substitutional alloys, and multi-component alloys.

Cantor et al. [1,33] pointed out that a conventional alloy development strategy leads to an enormous amount of knowledge about alloys based on one or two components, but little or no knowledge about alloys containing several main components in near-equal proportions. Theoretical and experimental works on the occurrence, structure, and properties of crystalline phases have been restricted to alloys based on one or two main components. Thus, the information and understanding are highly developed on alloys close to the corners and edges of a multi-component phase diagram, with much less knowledge about alloys located at the center of the phase diagram, as shown schematically for ternary and quaternary alloy systems in Fig. 1.1. This imbalance is significant for ternary alloys but becomes rapidly much more pronounced as the number of components increases. For most quaternary and other higher-order systems, information about alloys at the center of the phase diagram is virtually nonexistent except those HEA systems that have been reported very recently.

In the 1990s, researchers began to explore for metallic alloys with super-high glass-forming ability (GFA). Greer [29] proposed a confusion principle, which states that the more elements involved, the lower the chance that the alloy can select viable crystal structures, and thus the greater the chance of glass formation. Ma et al. [3] found that the best glass former is not exactly at the eutectic composition, and has a shift towards the high-entropy zone in the phase diagram. Recently, Takeuchi et al. [34] reported a high-entropy bulk metallic glass (BMG), which can have a critical size over 10 mm. Zhao et al. [35] and Gao et al. [36] reported a high-entropy BMG, which can be plastically deformed at room temperature. However, for some HEAs, their GFA is rather low, and they can only form

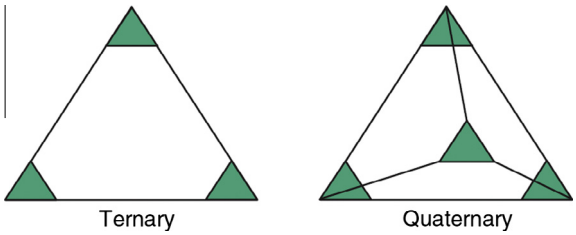

Fig. 1.1. Schematic ternary and quaternary alloy systems, showing regions of the phase diagram that are relatively well known (green) near the corners and relatively less well known (white) near the center [33].

solid-solutions even though the cooling rate is very high, e.g., alloys of CuCoNiCrAlFeTiV, FeCrMnNiCo, CoCrFeNiCu, AlCoCrFeNi, NbMoTaWV, etc. [1,2,12–14].

The yield strength of the body-centered cubic (BCC) HEAs can be rather high [12], usually comparable to BMGs [12]. Moreover, the high strength can be kept up to 800 K or higher for some HEAs based on 3d transition metals [14]. In contrast, BMGs can only keep their high strength below their glass-transition temperature.

1.1. Four core effects

Being different from the conventional alloys, compositions in HEAs are complex due to the equi-molar concentration of each component. Yeh [37] summarized mainly four core effects for HEAs, that is: (1) Thermodynamics: high-entropy effects; (2) Kinetics: sluggish diffusion; (3) Structures: severe lattice distortion; and (4) Properties: cocktail effects. We will discuss these four core effects separately.

1.1.1. High-entropy effect

The high-entropy effects, which tend to stabilize the high-entropy phases, e.g., solid-solution phases, were firstly proposed by Yeh [9]. The effects were very counterintuitive because it was expected that intermetallic compound phases may form for those equi- or near equi-atomic alloy compositions which are located at the center of the phase diagrams (for example, a monoclinic compound AlCeCo forms in the center of Al–Ce–Co system [38]). According to the Gibbs phase rule, the number of phases (P) in a given alloy at constant pressure in equilibrium condition is:

$$P = C + 1 - F \tag{1-1}$$

where C is the number of components and F is the maximum number of thermodynamic degrees of freedom in the system. In the case of a 6-component system at given pressure, one might expect a maximum of 7 equilibrium phases at an invariant reaction. However, to our surprise, HEAs form solid-solution phases rather than intermetallic phases [1,2,4,17]. This is not to say that all multi-components in equal molar ratio will form solid solution phases at the center of the phase diagram. In fact, only carefully chosen compositions that satisfy the HEA-formation criteria will form solid solutions instead of intermetallic compounds.

The solid-solution phase, according to the classical physical-metallurgy theory, is also called a terminal solid solution. The solid-solution phase is based on one element, which is called the solvent, and contains other minor elements, which are called the solutes. In HEAs, it is very difficult to differentiate the solvent from the solute because of their equi-molar portions. Many researchers reported that the multi-principal-element alloys can only form simple phases of body-centered-cubic (BCC) or face-centered-cubic (FCC) solid solutions, and the number of phases formed is much fewer than the maximum number of phases that the Gibbs phase rule allows [9,23]. This feature also indicates that the high entropy of the alloys tends to expand the solution limits between the elements, which may further confirm the high-entropy effects.

The high-entropy effect is mainly used to explain the multi-principal-element solid solution. According to the maximum entropy production principle (MEPP) [39], high entropy tends to stabilize the high-entropy phases, i.e., solid-solution phases, rather than intermetallic phases. Intermetallics are usually ordered phases with lower configurational entropy. For stoichiometric intermetallic compounds, their configurational entropy is zero.

Whether a HEA of single solid solution phase is in its equilibrium has been questioned in the scientific community. There have been accumulated evidences to show that the high entropy of mixing truly extends the solubility limits of solid solution. For example, Lucas et al. [40] recently reported absence of long-range chemical ordering in equi-molar FeCoCrNi alloy that forms a disordered FCC structure. On the other hand, it was reported that some equi-atomic compositions such as AlCoCrCuFeNi contain several phases of different compositions when cooling slowly from the melt [15], and thus it is controversial whether they can be still classified as HEA. The empirical rules in guiding HEA formation are addressed in Section 2, which includes atomic size difference and heat of mixing.

1.1.2. Sluggish diffusion effect

The sluggish diffusion effect here is compared with that of the conventional alloys rather than the bulk-glass-forming alloys. Recently, Yeh [9] studied the vacancy formation and the composition partition in HEAs, and compared the diffusion coefficients for the elements in pure metals, stainless steels, and HEAs, and found that the order of diffusion rates in the three types of alloy systems is shown below:

$$\text{HEAs} < \text{stainless steels} < \text{pure metals}$$

The sluggish diffusion effect is usually used to explain the formation of nano-sized precipitations, because the nuclei are easier to form but grow slowly, as shown in Fig. 1.2 on an as-cast CuCoNiCrFe alloy [2]. In the figure, nano-precipitates with a size of 7–50 nm in diameter, close to the FCC phase in a spinodal plate appear, as shown in Fig. 1.2B(b). Fig. 1.2 also shows that the microstructures of certain HEAs are usually very complicated, which can include nano-precipitates, ordered solid-solution phases, disordered solid-solution phases, and even amorphous phases. This feature is due to the fact that the interactions between the principal elements and the content of all the elements are very high.

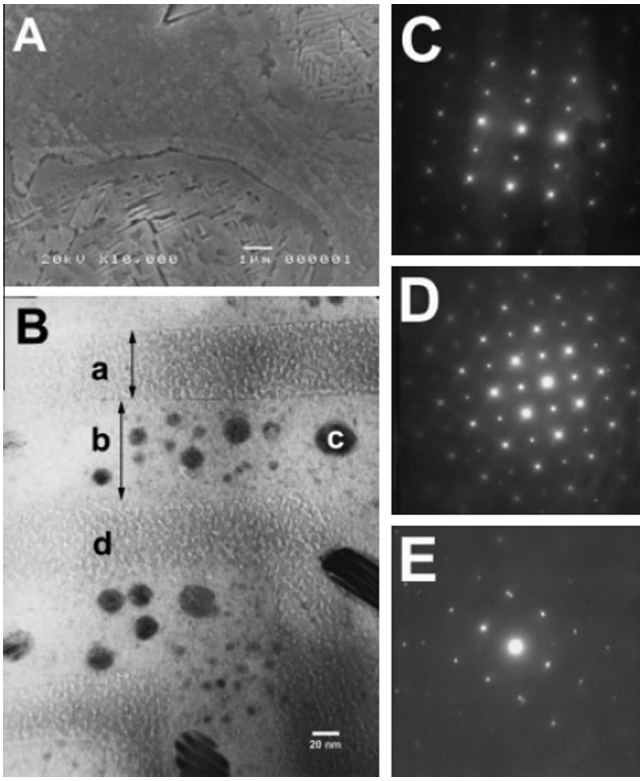

Fig. 1.2. Microstructures of an as-cast CuCoNiCrAlFe alloy. (A) SEM micrograph of an etched alloy with dendrites (a spinodal structure of disordered BCC and ordered BCC phases) and interdendrite (an FCC phase) structures. (B) TEM bright-field image; (B-a) an inter-spinodal plate, 70-nm wide, a disordered BCC phase (A2), lattice constant, 2.89 A; (B-b) a spinodal plate, 100-nm wide, an ordered BCC phase (B2), lattice constant, 2.89 A; (B-c) nanoprecipitation in a spinodal plate, 7 nm to 50 nm in diameter, close to the FCC phase; (B-d) nanoprecipitation in an interspinodal plate, 3 nm in diameter, a disordered BCC phase (A2). (C–E) Corresponding selected area diffraction (SAD) patterns of B, Ba, and Bb with zone axes of BCC [011], BCC [001] + (010) superlattice, and FCC [011], respectively [2].

1.1.3. Severe lattice-distortion effect

The severe lattice-distortion effect is usually compared with the one dominant element alloys, where the lattice site is occupied mainly by the dominant constituent. For HEAs, each element has the same possibility to occupy the lattice site, if ignoring chemical ordering. Since the size of different elements can be very different in some cases, this can lead to the severe lattice distortion. This effect is well confirmed by the ultrahigh strength of the BCC HEAs [11]. Yeh et al. [41] studied the anomalous decrease in X-ray diffraction (XRD) intensities of the CuNiAlCoCrFeSi alloy systems with multi-principal elements. A series of CuNiAlCoCrFeSi alloys with a systematic addition of principal elements from pure element to seven elements was investigated for the quantitative analysis of XRD intensities. The variation of XRD peak intensities of the alloy system is similar to that caused by thermal effects, but

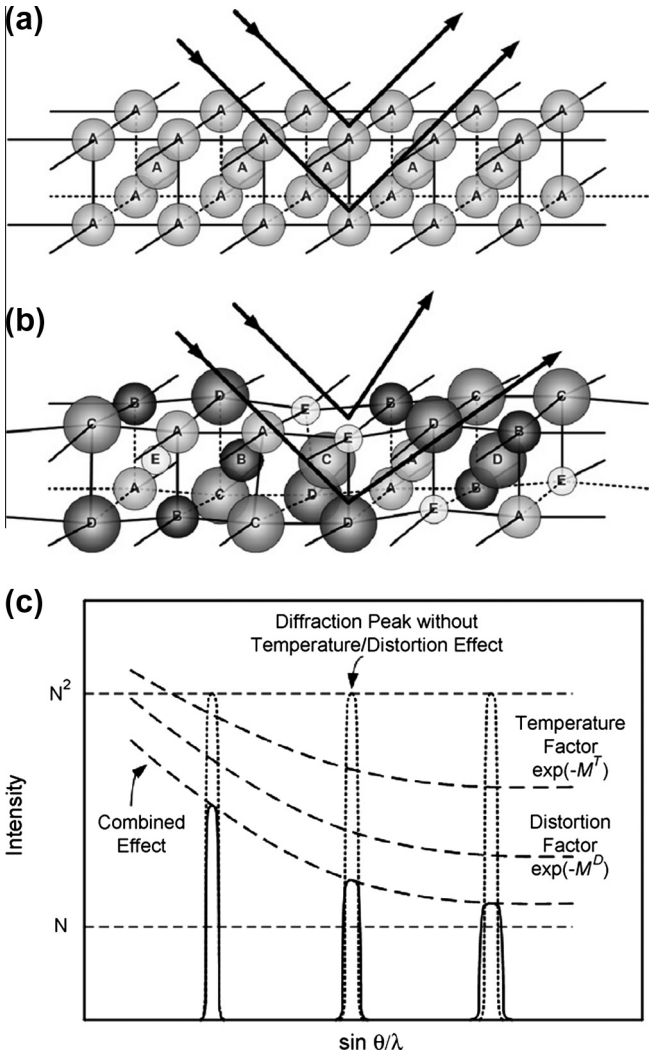

Fig. 1.3. Schematic illustration of intrinsic lattice distortion effects on Bragg diffraction: (a) perfect lattice with the same atoms; (b) distorted lattice with solid solutions of different-sized atoms, which are expected to randomly distribute in the crystal lattice according to a statistical average probability of occupancy; (c) temperature and distortion effects on the XRD intensity [41].

the intensities further drop beyond the thermal effect with increasing the number of constituent principal elements. An intrinsic lattice distortion effect caused by the addition of multi-principal elements with different atomic sizes is expected for the anomalous decrease in the XRD intensities. The mathematical treatment of this distortion effect for the modification of the XRD structure factor is formulated to be similar to that of the thermal effect, as shown in Fig. 1.3 [41]. The larger roughness of the atomic planes makes the intensity of the XRD for HEAs much lower than that for the single-element solid.

The severe lattice distortion is also used to explain the high strength of HEAs, especially the BCC-structured HEAs [4,12,23]. The severe lattice-distortion effect is also related to the tensile brittleness and the slower kinetics of HEAs [2,9,11]. However, the authors also noticed that single-phase FCC-structured HEAs have very low strength [7], which certainly cannot be explained by the severe lattice distortion argument. Fundamental studies in quantification of lattice distortion of HEAs are needed.

1.1.4. Cocktail effect

The cocktail-party effect was usually used as a term in the acoustics field, which have been used to describe the ability to focus one's listening attention on a single talker among a mixture of conversations and background noises, ignoring other conversations. For metallic alloys, the effect indicates that the unexpected properties can be obtained after mixing many elements, which could not be obtained from any one independent element. The cocktail effect for metallic alloys was first mentioned by Ranganathan [42], which has been subsequently confirmed in the mechanical and physical properties [12,13,15,18,35,43].

The cocktail effect implies that the alloy properties can be greatly adjusted by the composition change and alloying, as shown in Fig. 1.4, which indicates that the hardness of HEAs can be dramatically changed by adjusting the Al content in the $CoCrCuNiAl_x$ HEAs. With the increase of the Al content, the phases change from FCC to BCC + FCC and then to BCC structures. As a result, the lattice constants for both the BCC and FCC structures increase, and the hardness of the alloys increases. Fig. 1.5 presents the change of hardness as a function of the Al content for the Cu-free $CoCrFeNiAl_x$ HEAs [44]. The hardness of the FCC phase does not vary too much with changing the Al content from 0 to 0.45, while the hardness of the BCC phase decreases from about HV 538 to HV 480 as the Al content increases from 0.88 to 2.0. Moreover, the two phase region of FCC + BCC structures becomes much narrower for $CoCrFeNiAl_x$ than $CoCrCuFeNiAl_x$ indicating that Cu stabilizes the FCC phase. But caution should be addressed here for Cu: Cu tends to segregate and form very Cu-rich phase(s) in

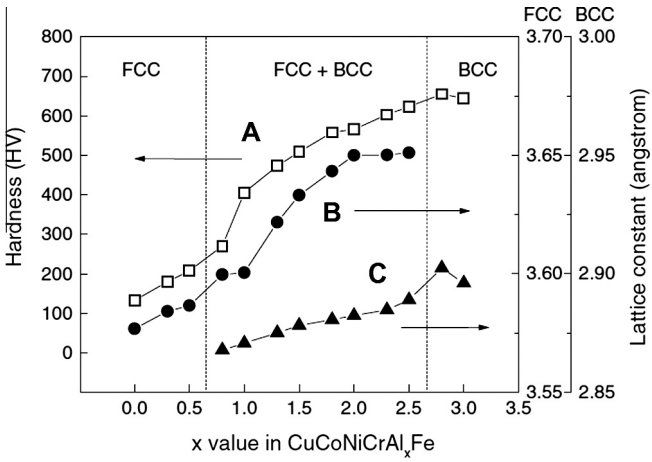

Fig. 1.4. Hardness and lattice constants of a $CuCoNiCrAl_xFe$ alloy system with different *x* values: (A) hardness of $CuCoNiCrAl_xFe$ alloys, (B) lattice constants of an FCC phase, (C) lattice constants of a BCC phase [2].

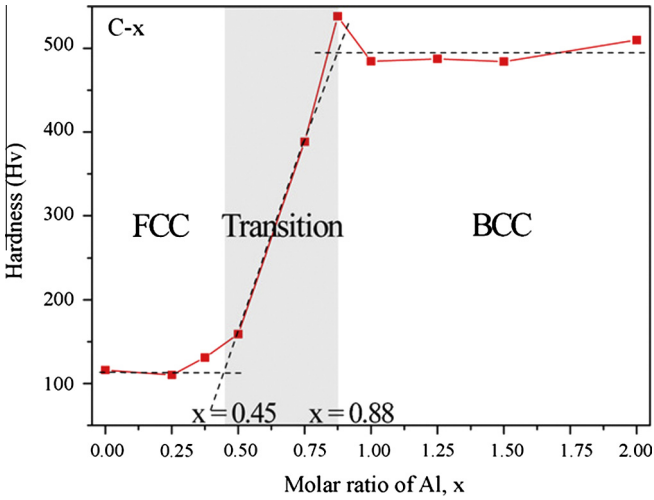

Fig. 1.5. Hardness of a $CoNiCrAl_xFe$ alloy system with different x values, the Cu-free alloy has lower hardness than that of the $CuCoCrAl_xFe$ alloy [44].

$CoCrCuFeNiAl_x$ [15,45]. Cu forms isomorphous solid solution with Ni but it is insoluble in Co, Cr and Fe; it dissolves about 20 at.% Al but also forms various stable intermetallic compounds with Al.

Fig. 1.6 exhibits the hardness of some reported HEAs in the descending order with stainless steels as benchmark. The MoTiVFeNiZrCoCr alloy has a very high value of hardness of over 800 HV while CoCrFeNiCu is very soft with a value of less than 200 HV. Fig. 1.7 compares the specific strength, which is defined by the yield strength over the density of the materials, and the density among HEAs, BMGs, conventional alloys, polymers and foam materials [5]. We can see that HEAs have densities close to the steel but have high values of specific strength (yield strength/density). This is partially because our recently-reported HEAs usually contain mainly the late transitional elements whose density is on the high side. The lightweight HEAs have much more potential because lightweight elements can be used and the density of the resultant alloys will be lowered significantly. Fig. 1.8 shows the specific-yield strength of HEAs vs. Young's modulus compared with conventional alloys. As can be seen, HEAs exhibit the highest specific strength and their Young's modulus can be varied in a very large

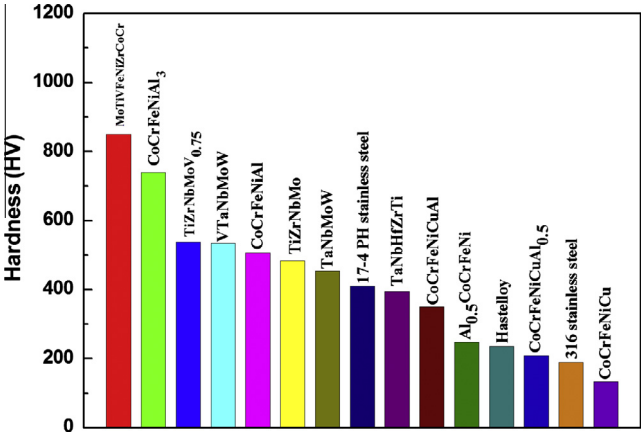

Fig. 1.6. Wide range of hardness for HEAs, compared with 17–4 PH stainless steel, Hastelloy, and 316 stainless steel.

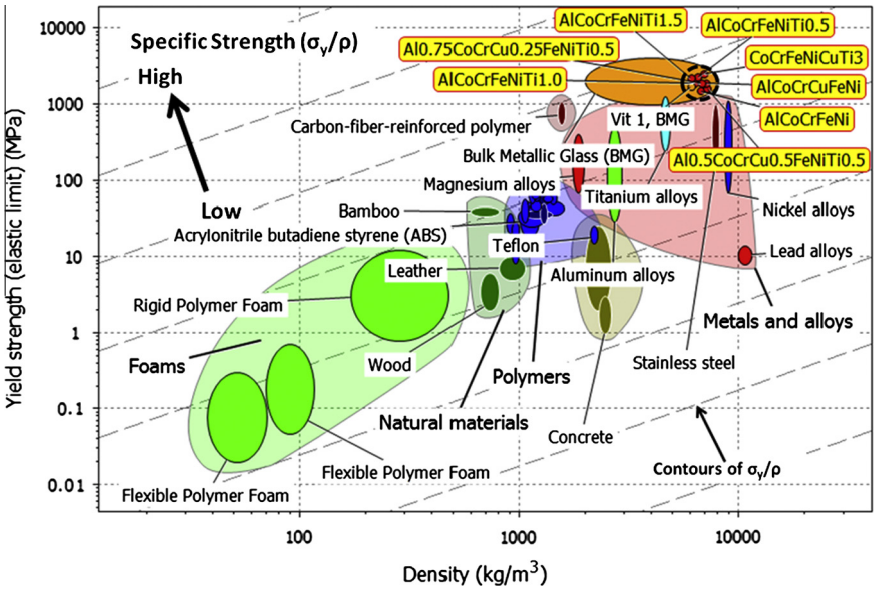

Fig. 1.7. Yield strength, σ_y, vs. density, ρ. HEAs (dark dashed circle) compared with other materials, particularly structural alloys. Grey dashed contours (arrow indication) label the specific strength, σ_y/ρ, from low (right bottom) to high (left top). HEAs are among the materials with highest strength and specific strength [5].

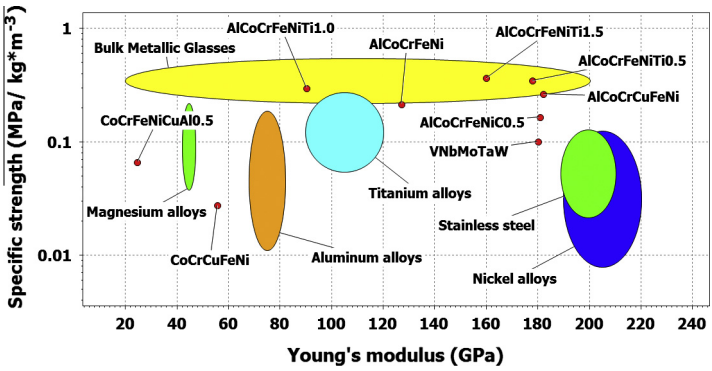

Fig. 1.8. Specific-yield strength vs. Young's modulus: HEAs compared with other materials, particularly structural alloys. HEAs are among the materials with highest specific strength and with a wide range of Young's modulus [5].

range. This observation may indicate that the modulus of HEAs can be more easily adjusted than conventional alloys. In addition to the high specific strength, other properties such as high hydrogen storage property are also reported [46].

1.2. Key research topics

To understand the fundamentals of HEAs is a challenge to the scientists in materials science and related fields because of lack of thermodynamic and kinetic data for multi-component systems in the center of phase diagrams. The phase diagrams are usually available only for the binary and ternary alloys. For HEAs, no complete phase diagrams are currently available to directly assist designing the

alloy with desirable micro- and nanostructures. Recently, Yang and Zhang [28] proposed the Ω parameter to design the solid-solution phase HEAs, which should be used combing with the parameter of atomic-size difference. This strategy may provide a starting point prior to actual experiments. The plastic deformation and fracture mechanisms of HEAs are also new because the high-entropy solid solutions contain high contents of multi-principal elements. In single principal-element alloys, dislocations dominate the plastic behavior. However, how dislocations interact with highly-disordered crystal lattices and/or chemical disordering/ordering will be an important factor responsible for plastic properties of HEAs. Interactions between the other crystal defects, such as twinning and stacking faults, with chemical/crystal disordering/ordering in HEAs will be important as well.

1.2.1. Mechanical properties compared with other alloys

For conventional alloys that contain a single principal element, the main mechanical behavior is dictated by the dominant element. The other minor alloying elements are used to enhance some special properties. For example, in the low-carbon ferritic steels [47–59], the main mechanical properties are from the BCC Fe. Carbon, which is an interstitial solute element, is used for solid-solution strengthened steels, and also to enhance the martensite-quenching ability which is the phase-transformation strengthening. The main properties of steels are still from Fe. For aluminum alloys [60] and titanium alloys [61], their properties are mainly related to the dominance of the elemental aluminum and titanium, respectively.

Intermetallic compounds are usually based on two elements, e.g., Ti–Al, Fe_3Al, and Fe_3Si. Intermetallic compounds are typically ordered phases and some may have strict compositional range. The Burgers vectors of the ordered phases are too large for the dislocations to move, which is the main reason why intermetallic phases are usually brittle. However, there are many successful case studies to improve the ductility of intermetallic compound by micro-alloying, e.g., micro-alloying of B in Ni_3Al [62], and micro-alloying of Cr in Fe_3Al [63,64].

Amorphous metals usually contain at least three elements although binary metallic glasses are also reported, and higher GFA can be obtained with addition of more elements, e.g., ZrTiCuNiBe (Vit-1), PdNiCuP, LaAlNiCu, and CuZrAlY alloys [65–69]. Amorphous metals usually exhibit ultrahigh yield strength, because they do not contain conventional any weakening factors, such as dislocations and grain boundaries, and their yield strengths are usually three to five times of their corresponding crystalline counterpart alloys. There are several models that are proposed to explain the plastic deformation of the amorphous metal, including the free volume [70], a shear-transformation-zone (STZ) [71], more recently a tension-transition zone (TTZ) [72], and the atomic-level stress [73,74]. The micromechanisms of the plastic deformation of amorphous metals are usually by forming shear bands, which is still an active research area till today. However, the high strength of amorphous alloys can be sustained only below the glass-transition temperature (T_g). At temperatures immediately above T_g, the amorphous metals will transit to be viscous liquids [68] and will crystallize at temperatures above the first crystallization onset temperature. This trend may limit the high-temperature applications of amorphous metals. The glass forming alloys often are chemically located close to the eutectic composition, which further facilitates the formation of the amorphous metal–matrix composite. The development of the amorphous metal–matrix composite can enhance the room-temperature plasticity of amorphous metals, and extend application temperatures [75–78].

For HEAs, their properties can be different from any of the constituent elements. The structure types are the dominant factor for controlling the strength or hardness of HEAs [5,12,13]. The BCC-structured HEAs usually have very high yield strengths and limited plasticity, while the FCC-structured HEAs have low yield strength and high plasticity. The mixture of BCC + FCC is expected to possess balanced mechanical properties, e.g., both high strength and good ductility. Recent studies show that the microstructures of certain "HEAs" can be very complicated since they often undergo the spinodal decomposition, and ordered, and disordered phase precipitates at lower temperatures. Solution-strengthening mechanisms for HEAs would be much different from conventional alloys. HEAs usually have high melting points, and the high yield strength can usually be sustained to ultrahigh temperatures, which is shown in Fig. 1.9 for refractory metal HEAs. The strength of HEAs are sometimes better than those of conventional superalloys [14].

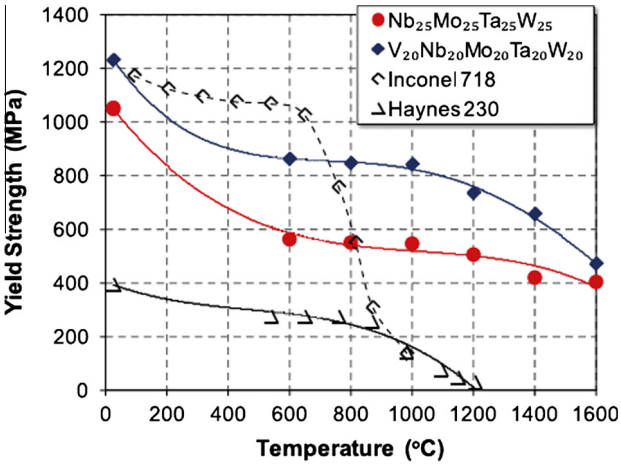

Fig. 1.9. Temperature dependence of NbMoTaW, VNbMoTaW, Inconel 718, and Haynes 230 alloys [14].

1.2.2. Underlying mechanisms for mechanical properties

Mechanical properties include the Young's modulus, yield strength, plastic elongation, fracture toughness, and fatigue properties. For the conventional one-element principal alloys, the Young's modulus is mainly controlled by the dominant element, e.g., the Young's modulus of Fe-based alloys is about 200 GPa, that of Ti-based alloys is approximately 110 GPa, and that of Al-based alloys is about 75 GPa, as shown in Fig. 1.8.

In contrast, for HEAs, the modulus can be very different from any of the constituent elements in the alloys [79], and the moduli of HEAs are scattered in a wide range, as shown in Fig. 1.8. Wang et al. [79] reported that the Young's modulus of the $CoCrFeNiCuAl_{0.5}$ HEA is about 24.5 GPa, which is much lower than the modulus of any of the constituent elements in the alloy. It is even lower than the Young's modulus of pure Al, about 69 GPa [80]. On the other hand, this value needs to be verified using other methods including impulse excitation of vibration.

It has been reported that the FCC-structured HEAs exhibit low strength and high plasticity [13], while the BCC-structured HEAs show high strength and low plasticity at room temperature [12]. Thus, the structure types are the dominant factor for controlling the strength or hardness of HEAs. For the fracture toughness of the HEAs, there is no report up to date.

1.2.3. Alloy design and preparation for HEAs

It has been verified that not all the alloys with five-principal elements and with equi-atomic ratio compositions can form HEA solid solutions. Only carefully chosen compositions can form FCC and BCC solid solutions. Till today there is no report on hexagonal close-packed (HCP)-structured HEAs. One reason is probably due to the fact that a HCP structure is often the stable structure at low temperatures for pure elements (applicable) in the periodic table, and that it may transform to either BCC or FCC at high temperatures. Most of the HEA solid solutions are identified by trial-and-error experiments because there is no phase diagram on quaternary and higher systems. Hence, the trial-and error approach is the main way to develop high-performance HEAs. However, some parameters have been proposed to predict the phase formation of HEAs [17,22,28] in analogy to the Hume-Rothery rule for conventional solid solution.

The fundamental thermodynamic equation states:

$$G = H - TS \tag{1-2}$$

where H is the enthalpy, S is the entropy, G is the Gibbs free energy, and T is the absolute temperature. From Eq. (1-2), the TS term will become significant at high temperatures. Hence, preparing HEAs from the liquid and gas would provide different kinds of information. These techniques may include sput-

tering, laser cladding, plasma coating, and arc melting, which will be discussed in detail in the next chapter. For the atomic-level structures of HEAs, the neutron and synchrotron diffraction methods are useful to detect ordering parameters, long-range order, and short-range ordering [81].

1.2.4. Theoretical simulations for HEAs

For HEAs, entropy effects are the core to their formation and properties. Some immediate questions are: (1) How can we accurately predict the total entropy of HEA phase? (2) How can we predict the phase field of a HEA phase as a function of compositions and temperatures? (3) What are the proper modeling and experimental methods to study HEAs? To address the phase-stability issue, thermodynamic modeling is necessary as the first step to understand the fundamental of HEAs. The typical modeling techniques to address thermodynamics include the calculation of phase diagram (CALPHAD) modeling, first-principle calculations, molecular-dynamics (MD) simulations, and Monte Carlo simulations.

Kao et al. [82] using MD to study the structure of HEAs, and their modeling efforts can well explain the liquid-like structure of HEAs, as shown in Fig. 1.10. Grosso et al. [83] studied refractory HEAs using atomistic modeling, clarified the role of each element and their interactions, and concluded that 4- and 5-elements alloys are possible to quantify the transition to a high-entropy regime characterized by the formation of a continuous solid solution.

2. Thermodynamics

Thermodynamics mainly addresses the relationship among the macroscopic variables, such as temperature, volume, and pressure, which describes physical properties of material bodies and heat radiation. The chemical thermodynamics study the role of entropy in chemical reactions. Statistical thermodynamics or statistical mechanics give explanations of macroscopic thermodynamics by statistical predictions of the collective motion of particles based on the mechanics of their microscopic behavior [84].

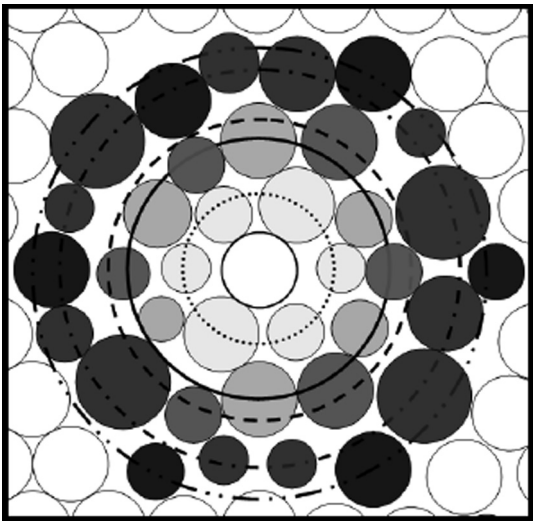

Fig. 1.10. A hard ball model of a liquid-like atomic-packing structure using multiple elements of different sizes. The circles represent the first, second, third, fourth, and fifth shells, respectively, but the second and third shells are indistinguishable due to the large atomic-size difference and thus the large fluctuation in occupation of different atoms. The fourth and fifth shells are also indistinguishable [82].

2.1. Entropy

Entropy is a thermodynamic property that can be used to determine the energy available for the useful work in a thermodynamic process, such as in energy-conversion devices, engines, or machines. The following equation is the definition of entropy:

$$dS = \frac{\Delta Q}{T} \tag{2-1}$$

where S is the entropy, Q is the heat flow, and T is the absolute temperature. Thermodynamic entropy has the dimension of energy divided by temperature, and a unit of Joules per Kelvin (J/K) in the International System of Units.

The statistical-mechanics definition of entropy was developed by Ludwig Boltzmann in the 1870s [85] and by analyzing the statistical behavior of the microscopic components of the system [86]. Boltzmann's hypothesis states that the entropy of a system is linearly related to the logarithm of the frequency of occurrence of a macro-state or, more precisely, the number, W, of possible micro-states corresponding to the macroscopic state of a system:

$$S = k \operatorname{Ln} W \tag{2-2}$$

where $k = 1.38 \times 10^{-23}$ J/K is Boltzmann's constant, and the logarithm is taken to be the natural base, "e".

For the alloy system, the Gibbs free energy of mixing can be expressed as follows:

$$\Delta G_{\text{mix}} = \Delta H_{\text{mix}} - T\Delta S_{\text{mix}} \tag{2-3}$$

where ΔG_{mix} is the Gibbs free energy of mixing, ΔH_{mix} is the enthalpy of mixing, ΔS_{mix} is the entropy of mixing, and T is the absolute temperature. From Eq. (2-3), we can see that if the ΔH_{mix} is kept constant, a higher entropy of mixing will lead to a lower Gibbs free energy, and make the alloy system more stable.

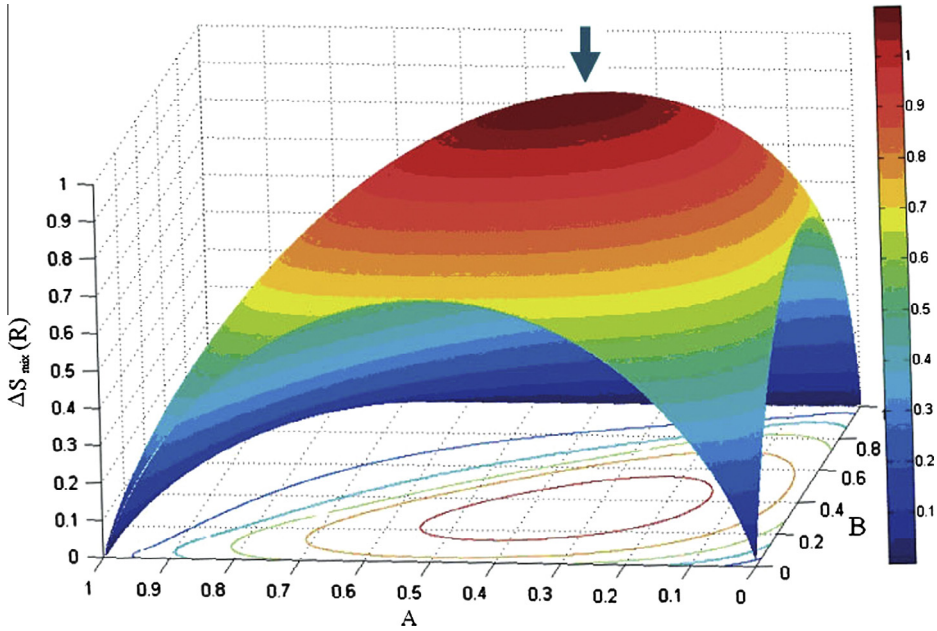

Fig. 2.1. Illustration of the ΔS_{mix} for ternary alloy system with the composition change [17].

Thus, we may wonder what kind of alloys has a high entropy of mixing. For a random solid solution with N component, the configurational entropy of mixing is:

$$\Delta S_{mix} = -R\sum_i c_i \ln c_i \tag{2-4}$$

where R (= 8.31 J/K mol) is the gas constant, and c_i is the molar content of the ith component. For the equi-atomic or equi-molar ratio alloys, the configurational entropy of mixing reaches its maximum, and Eq. (2-4) can be written as follows:

$$\Delta S_{\mathrm{mix}} = R \ln N \tag{2-5}$$

Fig. 2.1 presents the entropy of mixing as a function of composition in a ternary alloy system [17]. For the equi-molar ratio ternary alloy, $\Delta S_{\mathrm{mix}} = 1.1R$, reaching the maximum for the ternary alloy system.

The entropy of fusion is the increase in entropy when melting a substance. This value is always positive, since the degree of disorder increases in the transition from a long-range-ordered solid to a disordered structure of a liquid. The entropy of fusion is denoted as ΔS_f and normally expressed in J/mol K. A natural process, such as a phase change, will occur when the associated change in the Gibbs free energy is negative. It follows that the entropy of fusion is related to the melting point and the heat of fusion:

$$\Delta S_f = \frac{\Delta H_L}{T_f} \tag{2-6}$$

where ΔH_L is the heat of fusion or the latent heat of fusion, and T_f is the melting point. However, for the pure metal or the pure substance, T_f is one point, while for the alloys, there is a temperature range except those alloys that involve invariant reactions such as the congruent melting point or eutectic point: the solidus temperature (T_s) at which the melting starts, the liquidus temperature (T_l) at which melting finishes. In between the two temperatures, the alloy is in a state of mixture of solid and liquid phases.

For a quinary equi-molar ratio alloy, $\Delta S_{\mathrm{mix}} = 1.6R$. For pure metals or traditional metallic alloys, the fusion entropy usually is about $1R$ [86]. Hence, the entropy of mixing for a ternary equi-molar ratio element alloy is usually higher than that of the fusion entropy, and the difference between them become even larger for the higher-order HEAs.

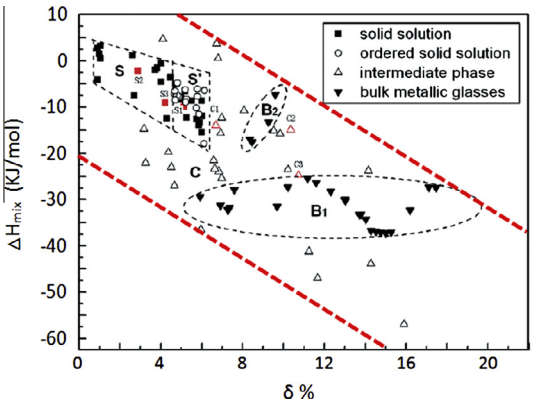

Fig. 2.2. A phase formation map based on the enthalpy of mixing ΔH_{mix} and the atomic size difference Delta, for the formation of random solid solution, $-15 < \Delta H_{\mathrm{mix}} < 5$ kJ/mol, $\delta < 5\%$. A transition zone with the mixture of ordered solid-solution and random solid-solution, in which: $-20 < \Delta H_{\mathrm{mix}} < 0$ kJ/mol, $5\% < \delta < 6.6\%$. The zones for B1 and B2 are glass formation zones, the other zone is for the intermetallic compounds [17].

Table 1
Atomic radius of some selected elements [88,89].

Element	Radius (nm)	Element	Radius (nm)	Element	Radius (nm)
O	0.07300	Sc	0.16410	Mg	0.16013
N	0.07500	Mo	0.13626	Zr	0.16025
C	0.07730	W	0.13670	Ca	0.19760
B	0.08200	Re	0.13750	Sn	0.16200
S	0.10200	Pd	0.13754	La	0.18790
P	0.10600	Pt	0.13870	Nd	0.16400
Be	0.11280	Ga	0.13920	Sc	0.16410
Si	0.11530	Zn	0.13945	Pr	0.16500
Ge	0.12400	Se	0.14000	In	0.16590
Fe	0.12412	U	0.14200	Mg	0.16013
Ni	0.12459	Nb	0.14290	Li	0.15194
Cr	0.12491	Ta	0.14300	Pb	0.17497
Co	0.12510	Al	0.14317	Th	0.18000
Cu	0.12780	Au	0.14420	Gd	0.18013
V	0.13160	Ag	0.14447	Y	0.18015
Mn	0.13500	Ti	0.14615	Hf	0.15775
Sn	0.16200	Gd	0.18013	Sm	0.18100
Nd	0.16400	Ce	0.18247		

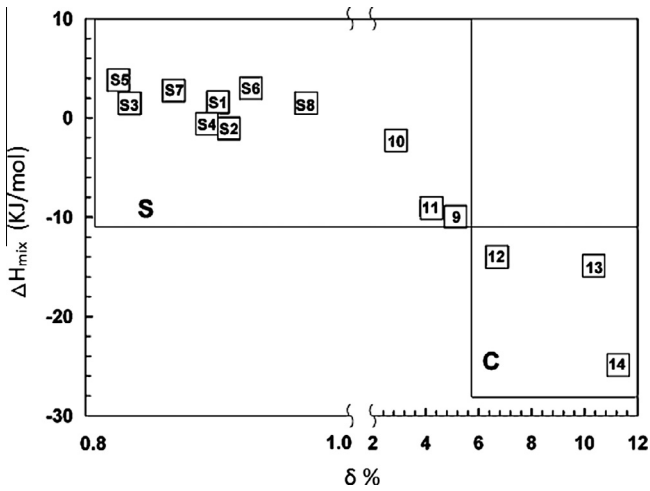

Fig. 2.3. Relationship between Delta, δ (here δ is amplified by 100 times for convenience) and ΔH_{mix} in some HEAs (S: indicates the alloy containing only solid solutions; C: indicates the alloy containing intermetallics; S1–S8: Ref. [2]; 9: CrFeCoNiAlCu0.25, 10: VCuFeCoNi, 11: Al0.5CrFeCoNi, 12:Ti2CrCuFeCoNi, 13: AlTiVYZr, 14: ZrTiVCuNiBe [93]).

However, the above analysis only considers random solid solution. For the real solution, the entropy of mixing can be much more complicated since the excess entropy of mixing needs to be considered. The excess entropy of mixing comes from existence of chemical ordering or segregation, and vibrational, magnetic, and electronic contributions. It can be negative or positive, depending on each individual system, as detailed in a review article by Oriani [87].

2.2. Thermodynamic considerations of phase formation

For alloy development of HEAs, a challenging question is how to predict phase stability (e.g., the number of equilibrium phases and the mole fractions) as a function of temperature and composition.

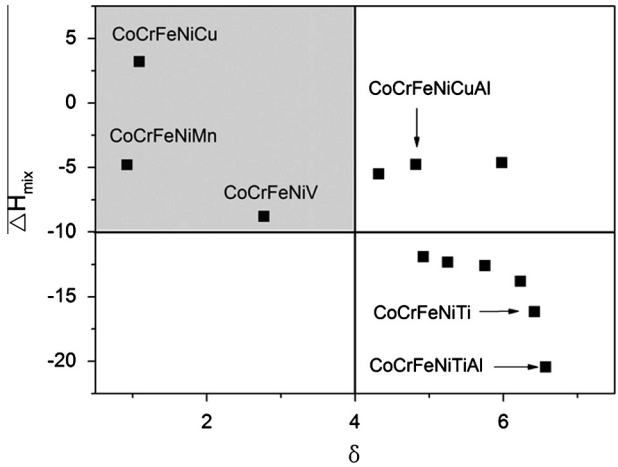

Fig. 2.4. Relationship between ΔH_{mix} and δ values of some HEA systems [94].

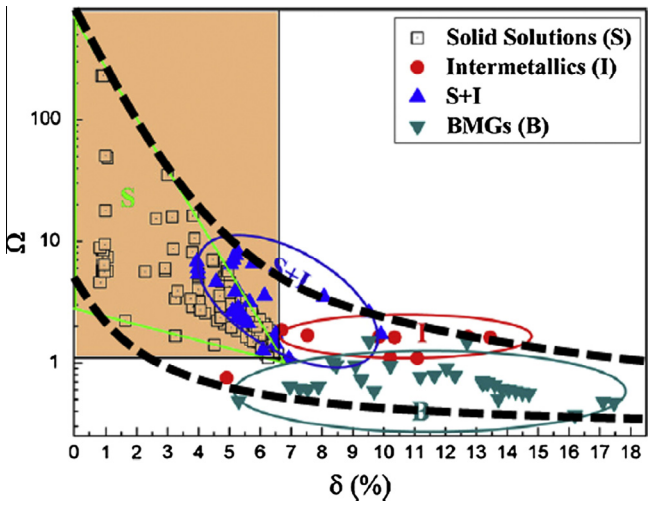

Fig. 2.5. Phase-formation map based on the Ω and δ for the multi-component alloys. For the formation of solid-solutions, $\Omega > 1.1$ and $\delta < 6.6\%$. The zone marked B means the zone mainly forms BMGs, and marked I mainly forms intermetallics compounds, also there is a transition zone which forms both the random solid solution and the intermetallic compound [28].

According to the Hume-Ruthery rule, the atomic-size difference (δ) and the enthalpy of mixing (ΔH_{mix}) are two dominant factors. For a HEA, the two parameters are defined as follows [88,89]:

$$\delta = \sqrt{\sum_{i=1}^{N} c_i \left(1 - r_i \Big/ \left(\sum_{i=1}^{N} c_i r_i\right)\right)^2} \tag{2-7}$$

$$\Delta H_{mix} = \sum_{i=1, i\neq j}^{N} 4\Delta H_{AB}^{mix} c_i c_j \tag{2-8}$$

where r_i is the atomic radius of the ith component, and ΔH_{AB}^{mix} is the enthalpy of mixing for the binary A and B elements. By summarizing the data from the literature, a diagram with $\Delta H_{mix} \sim \delta$ can be plotted, as shown in Fig. 2.2 [17]. It is known that the atomic size of an element is affected by the surrounding atoms. Here the Goldschmidt atomic size which is the atomic size when the coordination number is 12, is used. The typical data for most elements are listed in Table 1 [90,91]. For the enthalpy of mixing, only the binary data is available. Eq. (2-8) can be employed to evaluate the enthalpy of mixing for the multi-components alloys by the binary data, and some typical data for the binary enthalpy of mixing are available from Refs. [88,92].

Fig. 2.2 shows that ΔH_{mix} roughly decreases to more negative values with the increase of δ. For the random solid solutions, the ΔH_{mix} is in the range from −15 to 5 kJ/mol, while δ is in the range from 1% to 5%. Ren et al. [93] also summarized a similar $\Delta H_{mix} \sim \delta$ plot with their results, as shown in Fig. 2.3 which correlates very well with Fig. 2.2. Zhang and Fu [94] employed various HEA systems to explore the quantitative criterion for phase formation. The values of ΔS_{mix}, ΔH_{mix}, and δ for these HEA systems were also calculated from Eqs. (2-4), (2-7), and (2-8) and plotted in Fig. 2.4. It is clear that CoCrFeNiCu, CoCrFeNiMn, and CoCrFeNiV HEAs can form simple solid-solution phases. The ΔH_{mix} and δ values of these alloys approach zero as their positions are located at the upper-left corner of Fig. 2.4. However, the other alloys with ΔH_{mix} and δ values beyond the upper-left corner contain not only solid-solution phases but also intermetallic compounds. Therefore, criterion for simple solid solutions in HEAs should be the ΔH_{mix} and δ values falling into the upper-left district in Fig. 2.4 under the fulfillment of high entropy of mixing ($\Delta S_{mix} = 1.61R$). To be specific, the quantitative criterion for the formation of simple solid solutions is:

$$\Delta S_{mix} > 13.38\ \mathrm{J/K\ mol},\ -10\ \mathrm{kJ/mol} < \Delta H_{mix} < 5\ \mathrm{kJ/mol},\ \text{and}\ \delta < 4\%$$

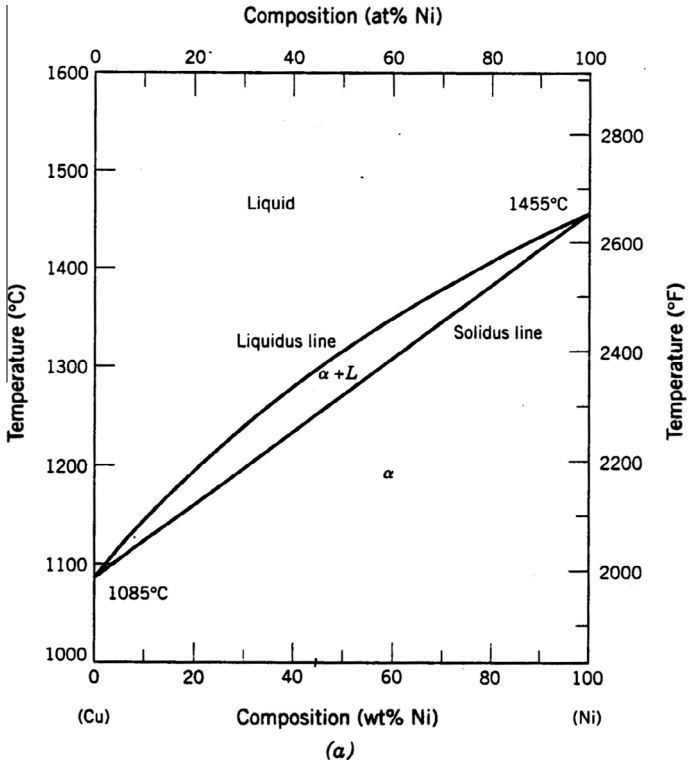

Fig. 2.6. Cu–Ni binary phase diagram [96].

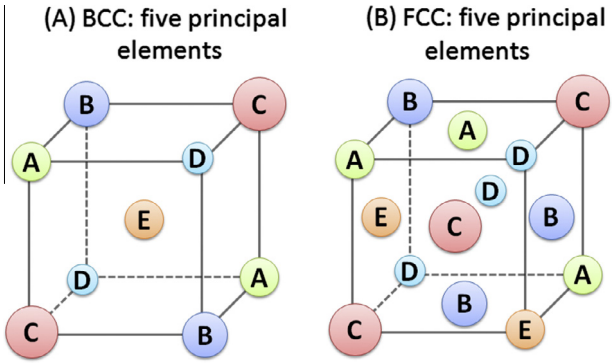

Fig. 2.7. Schematic illustrations of crystalline structures of (a) BCC and (b) FCC solid solutions composed of multi-principal elements [11].

While from Eq. (2-3), there are two parts for the Gibbs free energy of mixing. The first part, ΔH_{mix}, is mainly contributed by the interaction between different elements, while for the same element, $\Delta H_{mix} = 0$. For the binary system of A and B, ΔH_{AB} is negative if the A and B elements are attractive to each other. ΔH_{AB} is positive, if the interaction is repulsive.

For the multi-component system, ΔH_{mix} is the average value of the alloy system. The second part of Eq. (2-3) is $-T\Delta S_{mix}$. This part is usually negative, which decreases the Gibbs free energy of the alloy system. Thus, the ratio, $T\Delta S_{mix}/\Delta H_{mix}$, would be more important, and thus, a parameter Ω can be defined:

$$\Omega = T_m \Delta S_{mix} / |\Delta H_{mix}| \tag{2-9}$$

here T_m is the average melting point of the alloy system. According to Eq. (2-9), $\Omega > 1$ means that the effect of the mixing entropy is greater than that of the enthalpy of mixing at the melting temperature, and the high-entropy phase tends to form. To give a definition for the high entropy, we first need a benchmark: either the fusion entropy of the metallic alloys or the enthalpy of mixing at the melting point. Yeh et al. [2] selected the fusion entropy and the entropy of mixing for the five elements at an equi-atomic ratio is greater than the fusion entropy. The essence of this criterion, as shown in Eq. (2-9), is that high-entropy solid solution phase may form as long as $\Omega > 1$ is satisfied, which implies that the requirement of five principal elements to form HEAs may not be necessary. Theoretically speaking, three elements might form HEAs. The more elements in an equi-molar HEA, the higher entropy of mixing is. However, the content of each element should be higher than 5 at.%. The relation between Ω and δ is shown in Fig. 2.5. The plot suggests that the requirements for the solid-solution formation are $\Omega \geqslant 1.1$ and $\delta \leqslant 6.6\%$. Moreover, Ω and δ obey a hyperbolic relation, which indicates that $\delta \times \mathrm{Ln}\,\Omega = \text{constant}$ [28].

2.3. Microstructures of HEAs

Hume-Rothery [95] generalized several rules on substitutional solid solutions in alloy systems, including: (1) the difference in the atomic size between the solute and solvent atoms must be less than 15%, (2) the crystal structures of the solute and solvent must match, (3) there are the same valence states between the solvent and solute, and (4) the solute and solvent should have similar electronegativity. For generations, Hume-Rothery rules have been used in the traditional alloying design. Generally, a solid solution is often observed when the two elements (generally metals) involved are from the same family in the periodic table (i.e., the same column). Conversely, a chemical compound forms when the Hume-Rothery rules are not satisfied. Mind that Hume-Rothery rules only address substitutional solid solution. The solute may be incorporated into the solvent crystal lattice substitutionally, by replacing a solvent atom in the lattice, or interstitially, by fitting into the space between solvent

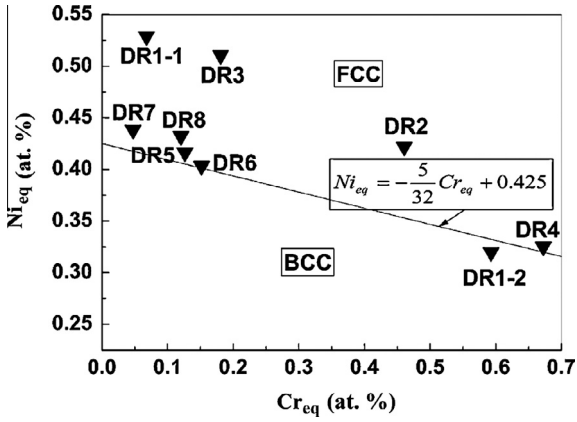

Fig. 2.8. The relationship among the microstructure, Ni_{eq} and Cr_{eq} of CuCrFeNiMn alloy system [93].

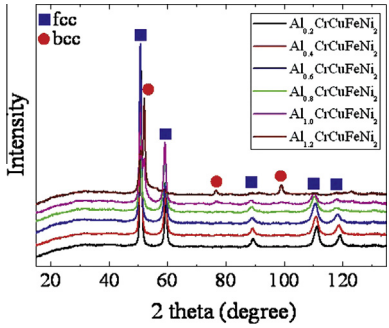

Fig. 2.9. X-ray diffraction patterns for $Al_xCrCuFeNi_2$ alloys (x = 0.2–1.2) [97].

atoms. Both types of solid solutions affect the properties of the material by distorting the crystal lattice and disrupting the physical and electronic homogeneity of the solvent material.

The binary Cu–Ni phase diagram, as shown in Fig. 2.6, is an example of Hume-Rothery rules of formation of an isomorphous solid solution [96]. All 4 rules are satisfied in this simple case. The case of HEAs seems to be an exception to the Hume-Rothery rules. All HEAs reported have a minimum of 4–5 components, and the elements have a mixture of simple FCC, BCC, and HCP structures. For example, the FCC CoCrCuFeNi HEA contains a BCC metal, Cr, while both Cu and Ni are FCC. Fe undergoes structural changes from BCC to FCC at 912 °C and FCC to BCC again at 1394 °C, and Co transforms to FCC from HCP at 422 °C. Furthermore, Cr also has much lower electronegativity than the rest of the elements in the alloy. Consequently, there are few elements in the periodic table that is soluble in Cr to an appreciable amount except V. However, formation of a FCC solid solution phase was observed and formation of intermetallic σ phases (Co_2Cr_3 and α-CoFe, Pearson symbol of tP30) was depressed in the CoCrCuFeNi and CoCrFeNi HEAs. Another example is the formation of a BCC solid solution phase in the $Al_3CoCrCuFeNi$ HEA. In this case, the element, Al, has an FCC structure. Therefore, it is tempting to state that the high entropy of mixing can overweigh the Hume-Rothery rules and perhaps is the most important parameter in the solid-solution formation that has been overlooked in the traditional physical metallurgy.

Till today, all reported HEAs have either the FCC or BCC structure, and no HCP structured HEAs, as shown in Fig. 2.7 [11]. This observation is not so surprising because most elements prefer a BCC or FCC structure. Among transition metals, there are a total of 9 elements that have a HCP structure at room

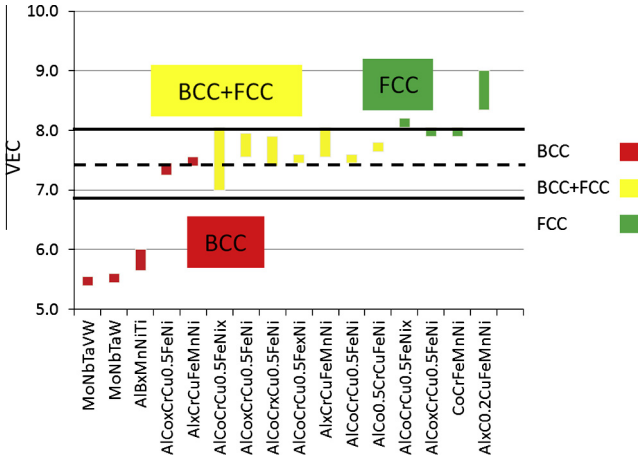

Fig. 2.10. Relationship between VEC and the FCC, BCC phase stability for HEA systems. Note on the legend: green color for sole FCC phases; red color for sole BCC phase; yellow color for mixes, FCC and BCC phases [97].

temperature, i.e. Sc, Ti, Zr, Hf, Co, Tc, Ru, Re, Os, Cd and Zn with the first five transforming to BCC at higher temperature. Tc is a radioactive element while Re, Ru and Os are extremely expensive elements. Cd and Zn both have a very low melting point and high vapor pressure. Among non-transition metals, Mg prefers a HCP structure while Be undergoes HCP → BCC transformation at $T = 1270\,^{\circ}C$. While the vast majority of rare earth elements prefer a HCP or double HCP structure at room temperature, most of them transform to BCC at very high temperatures. Therefore, it is likely that HEAs based on rare earth elements can be formed with a HCP structure given that: (1) they all have similar atomic sizes; (2) they all form isomorphous binary solid solution.

Ren et al. [93] suggested that elemental interactions can affect not only the distribution of elements in dendrite (DR) and inter-dendrite (ID) regions but also the microstructures in the CuCrFeNiMn alloy system. Alloys with a single FCC phase are always related to their high contents of Cu, Ni, and Mn, which is similar in stainless steels. According to the alloying effect of elements on microstructural characteristics in stainless steels, elements can be classified into two types: one is FCC stabilizer, such as Ni, Mn, Cu, C and N, and the other is BCC stabilizer, such as Cr, Mo, Si, and Nb. The Ni equivalent (Ni_{eq}, by a mass fraction) and Cr equivalent (Cr_{eq}, by a mass fraction) are often used to predict the changes of microstructures in stainless steels: the higher the Ni_{eq}, the easier it is to obtain an FCC structure. Conversely, the higher the Cr_{eq}, the easier it is to form a BCC structure. Therefore, the tendency in forming FCC and BCC phases can be estimated by means of the relationship between Ni_{eq} and Cr_{eq} in HEAs. Based on the experience and the distinct composition difference between stainless steels and HEAs, the expressions of Ni_{eq} and Cr_{eq} are modified properly as follows [93]:

$$Ni_{eq} = Ni\% + 0.5Mn\% + 0.25Cu\% \tag{2-10}$$

$$Cr_{eq} = Cr\% + Fe\% \tag{2-11}$$

where Ni%, Mn%, Cu%, Cr%, or Fe% stands for the atomic percent (at.%) of each element, as shown in Fig. 2.8.

However, Co is a well-known strong FCC former. Other FCC formers that are less known include Pd, Pt, Ir, and Rh. On the BCC former side, most refractory metals have a BCC structure and tend to stabilize the BCC structure, and, consequently, HEAs of various elemental combinations have been reported, based on refractory metals [14].

Guo et al. [97] suggested using the valence electron concentration (VEC) to predict the BCC and FCC structured solid solutions of HEAs.

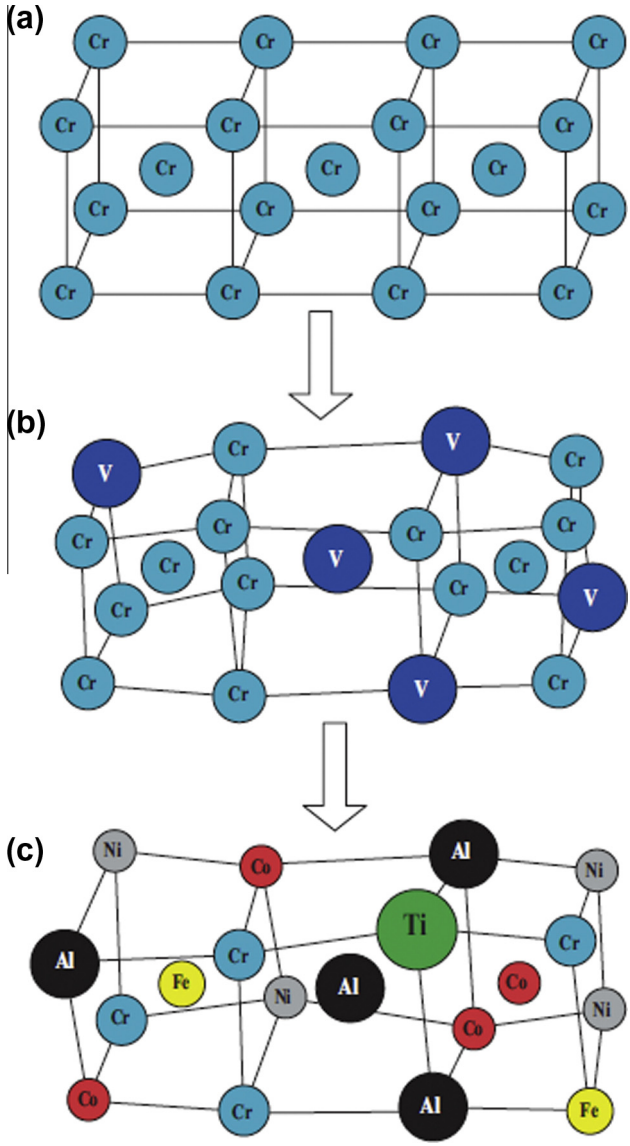

Fig. 2.11. Schematic illustration of BCC crystal structure: (a) perfect lattice (take Cr as example); (b) distorted lattice caused by additional one component with different atomic radius (take a Cr–V solid solution as example); (c) serious distorted lattice caused by many kinds of different-sized atoms randomly distributed in the crystal lattice with the same probability to occupy the lattice sites in multi-component solid solutions [20].

$$\mathrm{VEC} = \sum C_i(\mathrm{VEC}_i) \tag{2-12}$$

here C_i is the atomic percent of the ith element, and VEC_i is the VEC of the ith element.

Fig. 2.9 shows the X-ray diffraction (XRD) patterns of Guo's alloys ($Al_xCrCuFeNi_2$) [97]. It is seen that with the increase of the Al content, the phase structures change from FCC to BCC in $Al_xCrCuFeNi_2$ alloys. Fig. 2.10 summarized the relationship between the structure and VEC, and we can see that for the BCC-structured solid solution, VEC < 6.8; while for FCC, VEC > 8 [97].

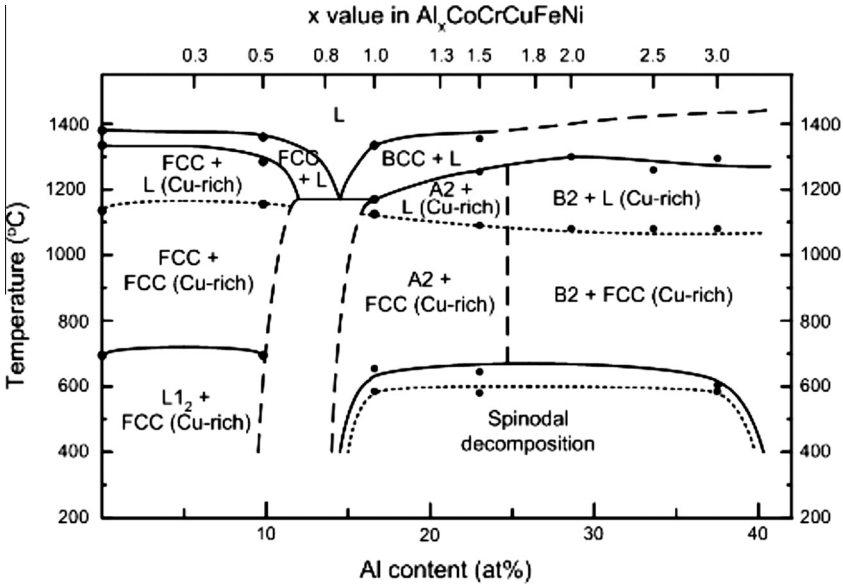

Fig. 2.12. Predicted phase diagram of Al$_x$CoCrCuFeNi alloy system with different aluminum contents (*x* values). L: liquid phase. The phase transition temperatures of the alloys were measured by DTA (temperature limit of measurement: 1400 °C) and indicated as black solid dots in the figure [45].

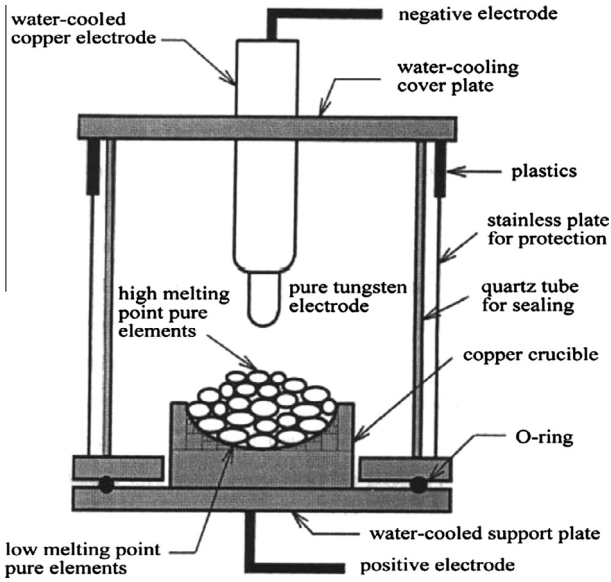

Fig. 3.1. A schematic diagram of the arc melting method [99].

Zhang et al. [20] suggested that the phase change from the FCC to BCC in the Ti$_x$CoCrFeNiCu$_{1-y}$Al$_y$ alloy system should be due to the atomic-level strain energy, as shown in Fig. 2.11. As the Al element has a relatively larger atomic size, the addition of the Al element will induce the higher atomic-level stress [73,74] in HEAs with the structure of higher atomic-packing efficiency (APE). The HEA with an

FCC structure generally has higher APE than that with a BCC structure. With more Al additions, the atomic-level stress will be increased too high to tolerate, and thus, resulting in a transition to the BCC structure with lower APE, which will decrease the strain energy and reduce the Gibbs free energy.

Tong et al. [45] plotted a simple phase diagram for the $Al_xCoCrCuFeNi$ alloy, as presented in Fig. 2.12, which shows the phase change with the variation of Al content at different temperatures. The phase diagram shows an eutectic reaction at 15 at.% Al. In the lower Al content region (<15 at.%), the primary phase is an FCC phase. While in the higher Al content region (>15 at.%), the primary phase becomes a BCC phase. When the Al content increases to more than 25 at.%, the ordered B2 phase dominates.

3. Kinetics and alloy preparation

Thermodynamics, as mentioned in the former section, mainly addresses the stability of the state, and does not concern the rate, time, and routes. The kinetics in materials science is defined as the process of the materials transition from one state to another, with time. There is also another term, dynamics, which is mainly used for mechanical behavior, and conventionally related to the loading speed and time. Thus, the kinetics for HEAs in this section will focus on the mobility of the elements during phase transformations. In another word, the mobility of the particles in the alloy is equal to the inverse of the viscosity, η, of the alloy, which is related to the diffusion coefficient, D, by the Stokes–Einstein equation [98]:

$$D = \frac{\kappa T}{6\pi\eta\gamma} \tag{3-1}$$

Eq. (3-1) is applicable in the case of low Reynolds numbers, for diffusion of spherical particles through a liquid, where D is the diffusion constant, γ is the radius of a diffusing particle, T is the absolute temperature, and $\kappa = \frac{R}{N}$, where R is the gas constant, and N is Avogadro's number.

The high entropy of the alloy in its liquid state will potentially facilitate forming the high-entropy phases. However, the kinetics play a very important role for phase formation. The microstructures of HEAs can be controlled by the cooling rate, the processing routes of the alloys, and plastic deformation in combination with various heat treatment. Thus, their properties can be optimized by controlling processing parameters.

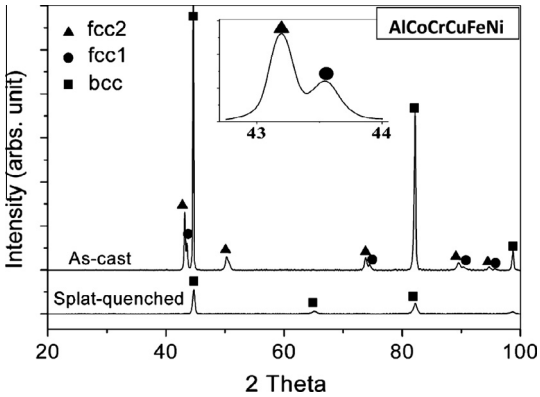

Fig. 3.2. XRD patterns of both splat-quenched and as-cast equi-atomic AlCoCrCuFeNi HEA. The splat-quenched HEA shows the presence of a BCC phase (a_{BCC} = 2.87 Å), whereas the as-cast HE alloy indicates the presence of one BCC (a_{BCC} = 2.87 Å) and two FCC phases. Two FCC phases are clearly visible from two overlapping peaks shown in the inset, corresponding to the two {1 1 1} planes with slightly different lattice parameters (a_{FCC1} = 3.59 Å and a_{FCC2} = 3.62 Å) [15].

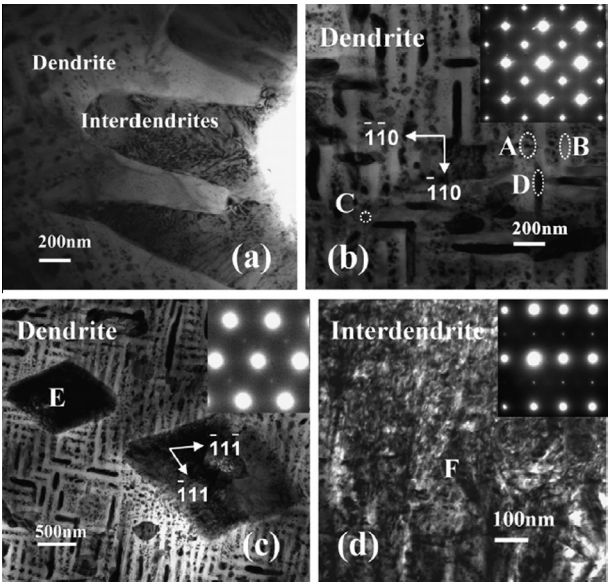

Fig. 3.3. Bright-field TEM images of as-cast equiatomic AlCoCrCuFeNi HE alloy: (a) dendrite and interdendritic regions; (b) microstructure of dendritic region with plate-like precipitates oriented along the ⟨1 1 0⟩ directions. The corresponding electron diffraction pattern of the [0 0 1] zone axis presented in the inset exhibits reflections of ordered BCC, B2 structure (a_{BCC} = 2.88 Å). The characters A–D are positions of the EDX measurements; (c) dendritic region with rhombohedron-shaped precipitates (a_{FCC2} = 3.64 Å). The corresponding electron diffraction pattern of the ⟨1 1 0⟩ zone axis in the inset displays weak superlattice reflections corresponding to L12 structure; (d) microstructure of the interdendritic region and corresponding electron diffraction pattern of the ⟨1 1 2⟩ zone axis, showing weak superlattice reflections corresponding to $L1_2$ structure (a_{FCC1} = 3.58 Å) [15].

At present, typical processing routes for HEAs can be summarized according to the starting states for the alloy preparation, mainly (1) from the liquid state, (2) from the solid state, (3) from the gas state, and (4) from electrochemical process.

3.1. Preparation from the liquid state

A popular liquid processing method is arc melting. The typical furnace is shown in Fig. 3.1. The torch temperature of the arc-melting furnace can be very high (>3000 °C), and can be controlled by

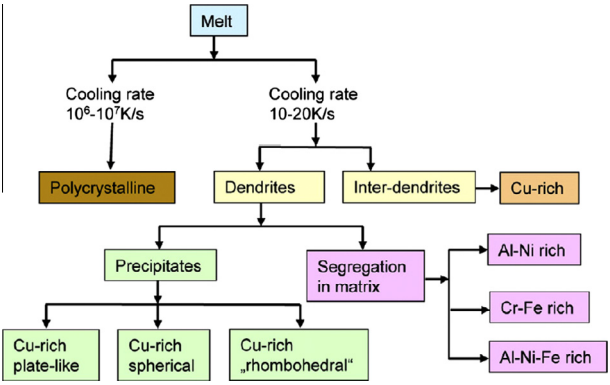

Fig. 3.4. Schematic representation of phase segregation observed during solidification of AlCoCrCuFeNi HEA by two different processing conditions: splat quenching (cooling rate 10^6–10^7 K s^{-1}) and casting (cooling rate 10–20 K s^{-1}) [15].

adjusting the electrical power. Hence, most of the high-melting elements can be mixed in their liquid state by this kind of furnaces [99]. However, for elements with a low melting point, which are easy to evaporate, e.g., Mg, Zn, and Mn, the arc-melting process may not be the best choice, because the composition cannot be precisely controlled. In this case, resistance heating or induction heating may be much more appropriate.

Singh et al. [15] carefully studied the decomposition process of the AlCoCrCuFeNi HEA, and they found that a high cooling rate tended to promote formation of a single phase, as presented in Fig. 3.2. Fig. 3.3 shows the bright-field TEM images of the as-cast AlCoCrCuFeNi HEA. Five phases were present in the as-cast sample; the interdendritic region consisting of the Cu-rich phase of an $L1_2$ structure (FCC1), dendrites containing Cu-rich plate-like precipitates of the B2 type, rhombohedron-shaped Cu-rich precipitates of the $L1_2$ type (FCC2), Al–Ni-rich plates (B2), and Cr–Fe-rich interplates (BCC). The structure of the spherical Cu-rich precipitates could not be determined because of their small size, but their composition is similar to that of the plate-like Cu-rich precipitates. Thus, it can be considered that these two phases are of the same type. Nevertheless, the Cu-rich FCC1 and FCC2 phases have different compositions and were identified as two separate phases. The kinetics of microstructure formation can be summarized in Fig. 3.4, which shows a strong dependence of microstructure on the cooling rate during preparation. It can be found that high cooling rates favored the formation of polycrystalline phases with a size of few nanometers. However, relatively low cooling rates led to the formation of typical dendritic and interdendritic microstructures due to elemental segregation. This work clearly demonstrated that for certain "HEAs", a single solid-solution phase can only form at relatively high cooling rates, and their high-entropy state is valid in a metastable condition. Annealing at elevated temperatures or using slow cooling rates induces the formation of multiple phases, resulting in a dramatic reduction in the configurational entropy of mixing due to elemental partitioning among these phases. Therefore, proper annealing experiments are crucial to testify if a true equilibrium state exists, i.e., a single high-entropy solid-solution phase can form.

Tong et al. [45] summarized the kinetics of the $Al_xCoCrCuFeNi$ (x from 0 to 3.0) HEAs during the cooling process, as shown in Fig. 3.5. For the alloy containing a high Al content, Spinodal decomposition occurs, leading to a submicron-modulated structure. Fig. 3.6 shows the XRD patterns for the alloy having a low Al content (i.e., $Al_{0.5}CoCrCuFeNi$) prepared under different conditions (as-annealed, as-rolled, and as-homogenized). It is clear that phase formation and microstructures of the alloy are typ-

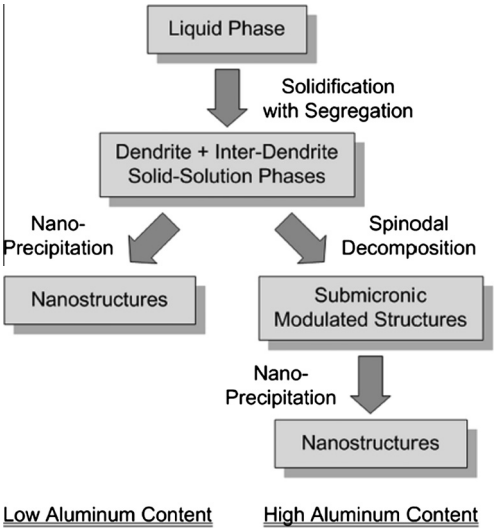

Fig. 3.5. Depiction of phase formation sequence during cooling of $Al_xCoCrCuFeNi$ alloy system with different aluminum contents [45].

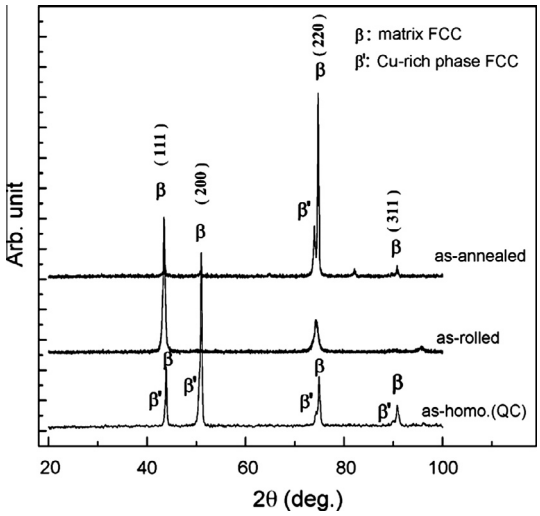

Fig. 3.6. XRD patterns of $Al_{0.5}CoCrCuFeNi$ alloy in the three states. QC: water quench [100].

ical kinetically dependent [100]. After annealing at 1173 K for 5 h, for example, the diffraction peak corresponding to the Cu-rich FCC phase becomes strong, suggesting that formation of this phase was greatly promoted.

Another liquid technique is Bridgman solidification, which is also called the Bridgman–Stockbarger method [101,102]. This method is named after the Harvard physicist, Percy Williams Bridgman, and the Massachusetts Institute Technology (MIT) physicist, Donald C. Stockbarger. This technique is primarily used for growing single-crystal ingots, and involves heating the polycrystalline material above its melting point and slowly cooling it from one end of its container, where a seed crystal is located.

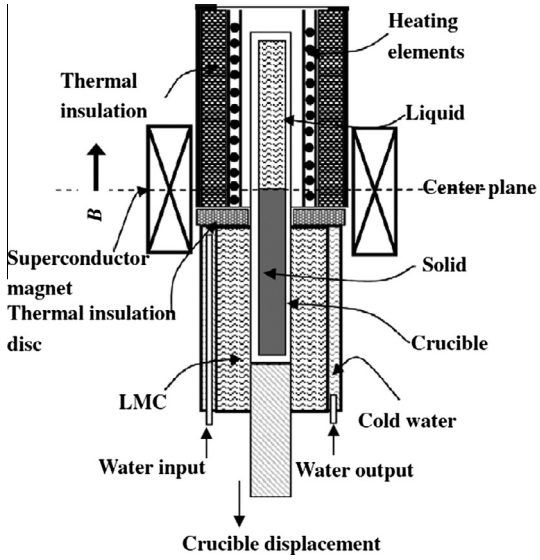

Fig. 3.7. A schematic diagram of the Bridgman solidification [104].

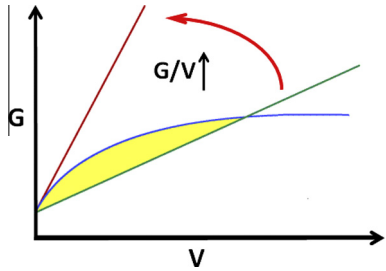

Fig. 3.8. A schematic diagram of the constitutional undercooling by G and V, here we assume that the solid and liquid interfaces are parallel to the liquid metal of Ga–In alloys surface, and the distance between the two faces keeps constant [106].

A single crystal of the same crystallographic orientation as the seed material is grown on the seed, and progressively formed along the length of the container. Such process can be carried out in a horizontal or vertical geometry. The Bridgman method is a popular way for producing certain semiconductor crystals for which the Czochralski process [103] is more difficult, such as gallium arsenide. The difference between the Bridgman technique and the Stockbarger method is subtle. While a temperature gradient is already in place for the Bridgman technique, the Stockbarger method requires pulling the boat through a temperature gradient to grow the desired single crystal. When seed crystals are not employed, polycrystalline ingots can also be produced from a feedstock consisting of rods, chunks, or any irregularly-shaped pieces once they are melted and allowed to re-solidify. The resulting microstructures of the ingots as obtained are characteristic of directionally solidified metals and alloys with the aligned grains [90,91]. Fig. 3.7 shows a typical Bridgman solidification facility cooled by a liquid metal (a Ga–In eutectic alloy, which is a liquid at room temperature) [104]. The samples are loaded in a crucible and melted by inductive heating or resistant heating, and then the melted alloys are gradually pulled down to the liquid metal. The outside of the liquid metal is further cooled by water.

Zhang et al. [105] reported that the morphology of AlCoCrFeNi alloy changed from the dendrite prepared by copper mould casting to the equi-axed grains by Bridgman solidification. This change was due to the high-temperature gradient, G, the low growth velocity, V, and the high ratio of G/V for the Bridgman solidification. For the copper-mould casting, G/V is usually low, as the G is a variable and V is usually very high. As shown in Fig. 3.8, the high G/V value tend to decrease the constitutional undercooling of the alloy, and thus it is possible to restrain the dendrite formation [106].

Wang et al. [107] applied a thermal-spray (TS) technology to fabricate coatings of the $Ni_xCo_{0.6}Fe_{0.2}Cr_ySi_zAlTi_{0.2}$ HEAs. A typical TS plasma facility is presented in Fig. 3.9 [108,109]. In this process, finely-divided HEA powders are initially melted on prepared substrates in order to form spray deposits. The required heat is generated by combustible gases or electric arcs in the thermal-spraying gun. As the target material is gradually heated up, it is converted to a molten state, and will be accelerated by the compressed gas. The confined stream of particles is carried to the substrate, and strikes the surface to flatten and forms thin platelets. These platelets are compatible with the irregularities of the prepared surface and to each other. Moreover, these sprayed particles are accumulated on the substrate by cooling and building up one by one into a cohesive structure. Thus, coatings are formed.

The results also indicate that the hardness of the HEAs prepared by the TS in combination with annealing at 1100 °C/10 h is significantly increased to that of the as-cast state (1045 HV). These samples exhibited excellent coarsening resistance, resulting from the Cr_3Si and several unidentified phases. The main features found in TEM are large amounts of nano-sized precipitates and dislocations. Note that, this $Ni_xCo_{0.6}Fe_{0.2}Cr_ySi_zAlTi_{0.2}$ alloy system does precipitate during casting, which is quite different from many other HEAs. The typical TEM characterization of the as-cast $Ni_xCo_{0.6}Fe_{0.2}Cr_ySi_zAlTi_{0.2}$ alloys with the addition/removal of Mn, Si, and Ni elements are also compared in this study. The results showed that a significant amount of nano-sized particles (ranging from 5 to 10 nm), atomic segregation, twinning structures, and sub-grain structures were distributed in the matrix. The above study further confirmed that phase formation and final microstructure of HEAs are strongly dependant on the processing conditions. Zhang et al. [110] reported the low-cost HEA coating with a nominal

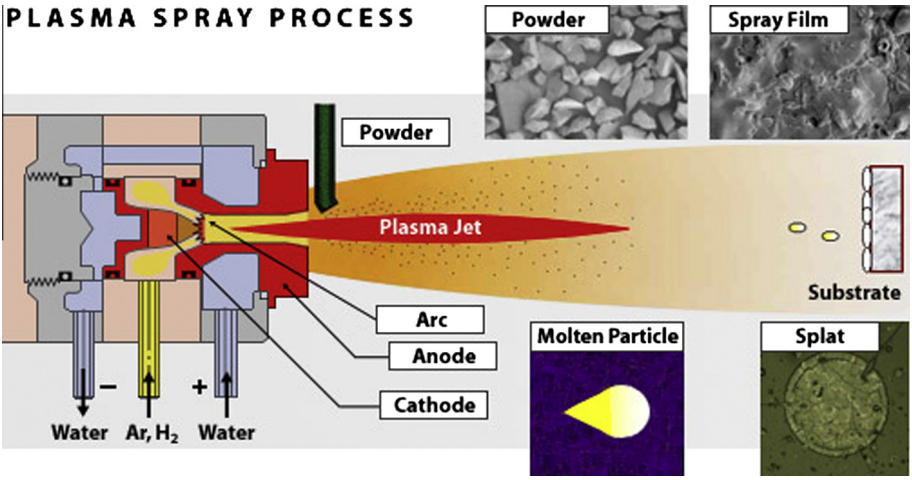

Fig. 3.9. Plasma Spray Process (Air Plasma Spray Coating). It is process sin which the metal substrate is coated with coating giving it a smooth protective layer. This includes air plasma spraying (ASP) particles of the coating at a pre-selected particle with velocity of about 500 meters per second [108].

composition of 6FeNiCoCrAlTiSi prepared by laser cladding. A typical schematic [111–113] is shown in Fig. 3.10. This technology is similar to the TS method in that it has an energy source to melt the feed stock that is being applied to a substrate. What it differs is that it uses a concentrated laser beam as the heat source, and it melts the substrate that the feed stock is being applied to. This technique normally results in a metallurgical bond that has the superior bond strength over TS. The resultant coating is dense with no voids or porosity. One of the advantages of the laser-cladding process is the laser beam which can be focused and concentrated to a very small area and keeps the heat-affected zone of the substrate very shallow. This feature minimizes the chance of cracking, distorting, or changing the metallurgy of the substrate. Additionally, the lower total heat minimizes the dilution of the coating with materials from the substrate.

The coating prepared by laser cladding has a simple BCC solid solution with high micro-hardness, high resistance to softening, and large electrical resistivity. After being annealed at $T < 750\,^{\circ}C$, the coating shows high thermal stability, and its resistivity slightly decreases, but the micro-hardness almost remains unchanged. After annealing at $T > 750\,^{\circ}C$, the micro-hardness of the coating slowly decreases with increasing the decomposition rate of the BCC solid solutions [110].

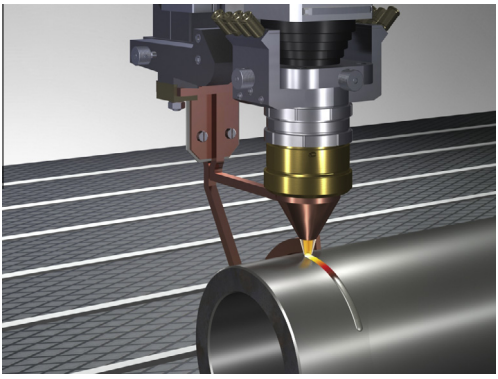

Fig. 3.10. A typical high-performance laser cladding using the laser-induction hybrid cladding head [111].

3.2. Preparation from the solid state

Mechanical alloying (MA) is a solid-state powder-processing technique involving repeated cold welding, fracturing, and re-welding of powder particles in a high-energy ball mill [114,115]. Originally developed to produce oxide-dispersion strengthened nickel- and iron-base superalloys for applications in aerospace industry, MA has now been shown to be capable of synthesizing a variety of equilibrium and non-equilibrium alloys starting from blended elemental or pre-alloyed powders. MA is akin to metal-powder processing, where metals may be mixed to produce superalloys. Mechanical alloying occurs in three steps. First, the alloy materials are combined in a ball mill and ground to fine powders. A hot-isostatic-pressing (HIP) process is then applied to simultaneously compress and sinter the powders. A final heat-treatment stage helps remove existing internal stresses produced during any cold compaction, which may have been used. This MA process has successfully produced alloys suitable for high-heat turbine blades and other aerospace components. The schematic for the mechanical alloying technique is shown in Fig. 3.11 [116].

Chen et al. [117] prepared the BeCoMgTi and BeCoMgTiZn equi-molar alloys entirely composed of HCP elements by MA. No crystalline solid solutions and compounds formed before full amorphization. Weeber and Bakker had classified the amorphization reactions of MA in binary alloys into three types in 1988 [118,119]. The first type (type-I) featured peak shifting of each element due to the formation of a crystalline solid-solution phase, and then peak broadening due to the formation of an amorphous structure. The second type (type-II) featured a decrease of elemental peaks accompanied with an increase of the amorphous broad peak. The final type (type-III) featured the formation of an intermetallic or intermediate compound prior to an amorphous structure [118]. The amorphization processes of these two alloys conform the type-II amorphization of the classification proposed by Weeber and Bakker et al. [118,119]. The inhibition of intermetallic compounds before amorphization is due to chemical compatibility among constituent elements in company with high-entropy and deformation effects, which enhance the mutual solubility. Direct formation of the amorphous phase instead of the crystalline one attributes to their large range of atomic size. This mechanism could be a guideline for the type-II amorphization of multi-component alloys.

Varalakshmi et al. [120] reported the nanocrystalline equiatomic HEAs synthesized by MA in the CuNiCoZnAlTi system from the binary CuNi alloy to the senary CuNiCoZnAlTi alloy. An attempt has been made to find the influence of non-equiatomic compositions on the HEA formation by varying the Cu content up to 50 at.% ($Cu_xNiCoZnAlTi$; x = 0%, 8.33%, 33.33%, and 49.98%). The phase formation and stability of mechanically-alloyed powders at an elevated temperature (1073 K for 1 h) were studied. The nano-crystalline equi-atomic alloys have FCC structure up to the quinary CuNiCoZn alloy and have a BCC structure in the hexanary CuNiCoZnAlTi alloy. In non-equiatomic alloys, BCC is the

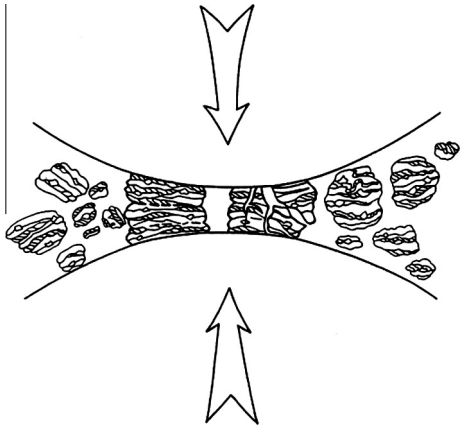

Fig. 3.11. The schematic for the mechanical alloying [116].

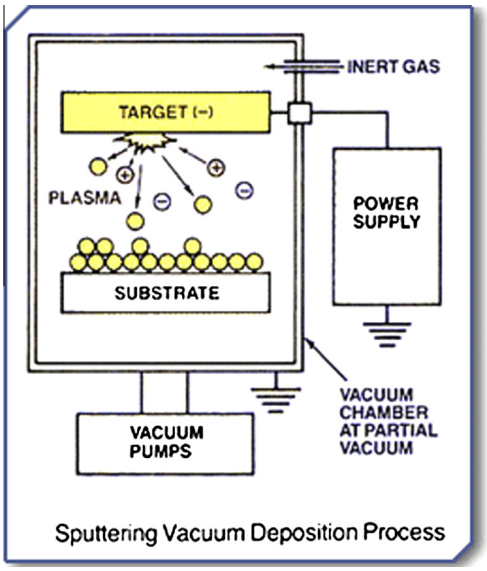

Fig. 3.12. A schematic diagram of the sputter method [123].

dominating phase in the alloys containing less than 8.33 at.% Cu, and the FCC phase was observed in alloys with a higher amount of Cu. The Vicker's bulk hardness and compressive strength of the equi-atomic nano-crystalline senary CuNiCoZnAlTi HEA after HIP are 8.79 and 2.76 GPa, respectively. The hardness of these HEAs is higher than that of most commercial hard facing alloys (e.g., stellite, whose compressive strength is 4.94 GPa).

3.3. Preparation from the gas state

To use HEA coatings as tribological applications, Chang et al. [121] prepared the (AlCrTaTiZr)N_x multi-component coatings by using the sputtering technique which is demonstrated in Fig. 3.12 [122]. Mechanical properties, creep behaviors, deformation mechanisms, and interface adhesion of the (AlCrTaTiZr)N_x coatings with different N contents were characterized. With increasing the N2-to-total (N_2 + Ar) flow ratio (RN) during the sputtering deposition, the (AlCrTaTiZr)N_x coatings transformed from an amorphous phase to a nano-composite and finally a crystalline nitride structure. The hardness of the coatings accordingly increased from 13 GPa to a high value of about 30 GPa, but the creep strain rate also increased from 1.3×10^{-4} to 7.3×10^{-4} s^{-1}. The plastic deformation of the amorphous coating deposited with RN = 0% proceeded through the formation and extension of shear bands, whereas dislocation activities dominated the deformation behavior of the crystalline nitride coatings deposited with RN = 10% and 30%. With increasing the RN, the interface adhesion energy between the coatings and the substrates was also enhanced from 6.1 to 22.9 J/m^2. On the Si substrates, a native oxide layer might exist. Consequently, the bonding between the oxide layer and the metallic coating with RN = 0% was weak. With increasing the RN, more N atoms were introduced and a larger number of strong covalent bonds between N, O and Si might probably form at the interfaces, thus enhancing the interface adhesion between the (AlCrTaTiZr)N_x coatings and the substrates. The morphology of the surface and cross-section of the deposited films are shown in Fig. 3.13. It is clear that the films are very uniform. In Fig. 3.13(a) and (b), no special growth feature was found in the amorphous coating deposited with RN = 0%. When increasing the RN to 10%, a columnar structure with a pyramid-like surface was observed in Fig. 3.13(c) and (d), suggesting formation of specific crystallography in this film by introducing an N_2 flow. As the RN increased to 30%, the surface morphology

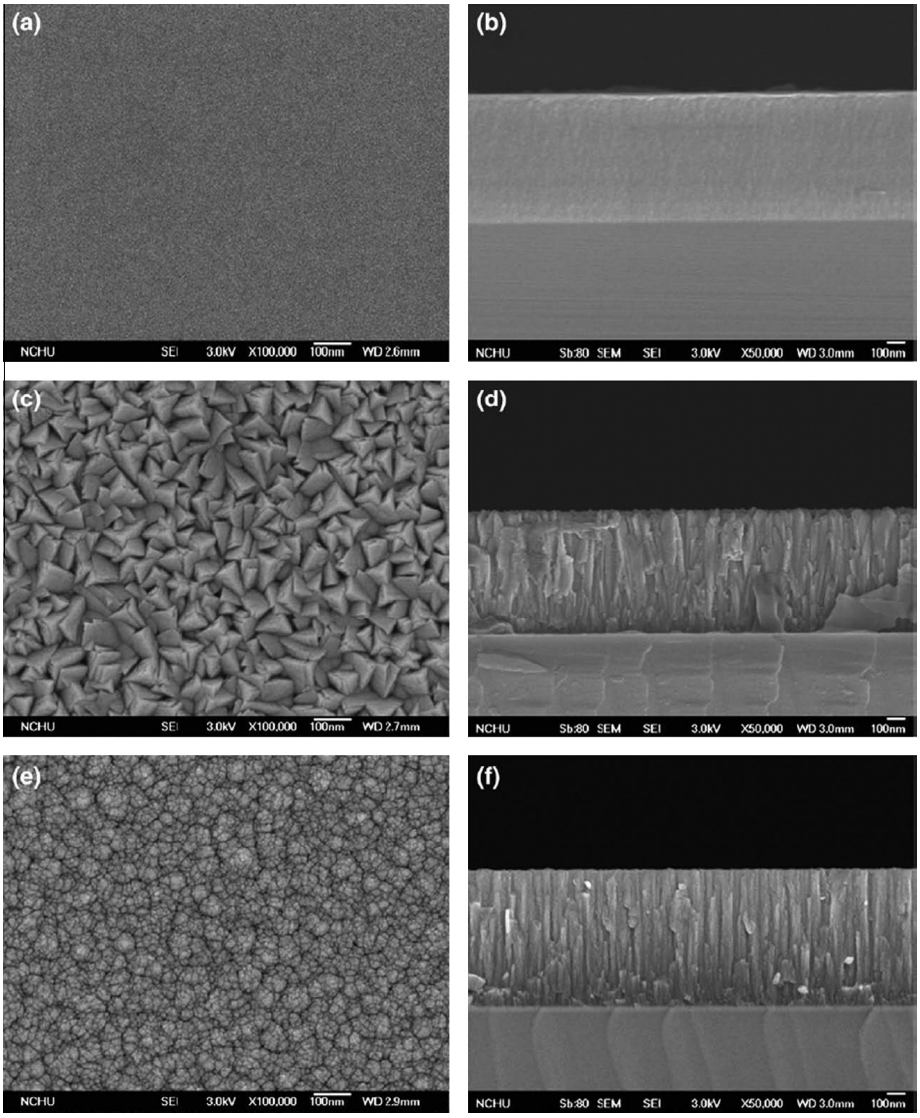

Fig. 3.13. SEM surface morphologies and cross-sectional microstructures of $(AlCrTaTiZr)N_x$ coatings deposited with different N2-to-total flow ratios (RN): (a) surface and (b) cross-section for RN = 0%; (c) surface and (d) cross-section for RN = 10%; (e) surface and (f) cross-section for RN = 30% [121].

transformed to a dome-like structure coexisted with the columnar structure as seen in Fig. 3.13(e) and (f), implying the further change in the crystallographic structure with a high N_2 flow.

Lin et al. [124] reported that the $(AlCrTaTiZr)O_x$ films deposited at 623 K by direct current (DC) magnetron sputtering from HEA target. Oxygen concentration increases with the oxygen flow ratio (RO), and saturates near 67 at.%. As-deposited films have an amorphous structure, but the morphology of these films are different as shown in Fig. 3.14. The metallic film is composed of grains about 20 nm, and smaller granules were seen in the grains without oxygen. The cross-section image shows column-like structure along the growth direction. The smaller granules are amorphous clusters, the "grains" are agglomerations of the clusters, and the columns are thus bundles of the agglomerations caused

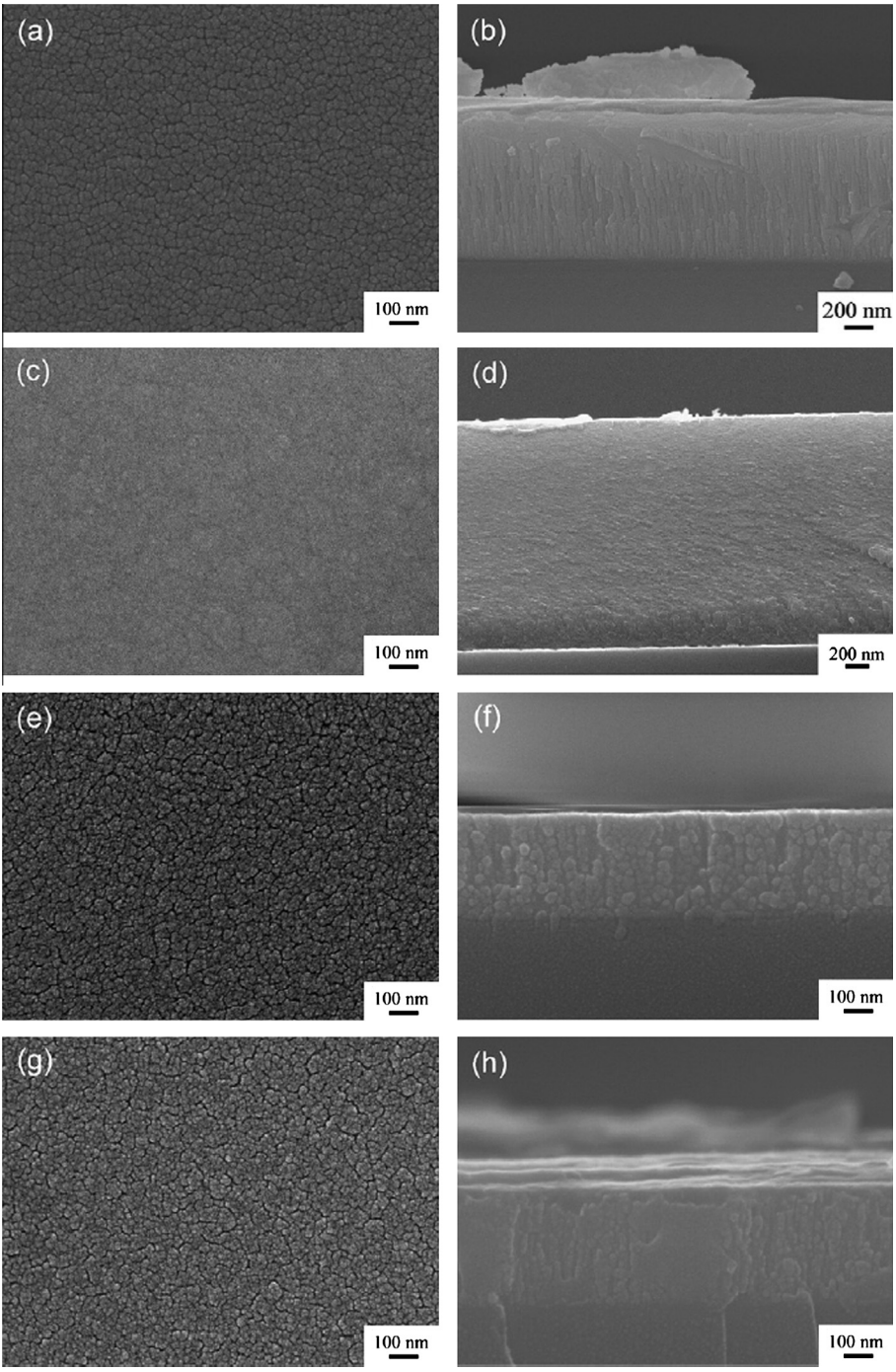

Fig. 3.14. Field Emission Scanning Electron Microscopy (FE-SEM) images of the as-deposited films: (a) plane view and (b) cross-section images of AlCrTaTiZr metallic films; (c) plane view and (d) cross-section images of films deposited at oxygen flow ratio (RO) = 2.5%; (e) plane view and (f) cross-section images of films deposited at RO = 15%; (g) plane view and (h) cross-section images of films deposited at RO = 50% [124].

from the film growth during sputtering. After addition of 2.5% oxygen to the atmosphere, the contrast of the films fades, the morphology becomes unclear, and the column structure disappears. The film is dense with no low density columnar grain boundaries. However, the surfaces of the films prepared at RO = 15% become rougher and show mosaic of crack network. The average mosaic unit size is around 30 nm. The cross section of the film shows lots of discrete pellets, which indicates that the film integrity is poor and easy to induce local cracking. At RO = 50%, the morphology is similar to the mosaic of cracks at RO = 15%, which is attributable to the tensile stress induced by the thermal expansion coefficient difference between the film and substrate during cooling. The hardness of these films varies in the range of 8–13 GPa. All amorphous oxide films maintain their amorphous structure up to 800 °C for at least 1 h. After annealing at 900 °C for 5 h, crystalline phases with the structures of ZrO_2, TiO_2, or Ti_2ZrO_6 form. Annealing enhances mechanical properties of the films, and the hardness and modulus can reach the values of about 20 and 260 GPa, respectively. The resistivity of the metallic films is around 10^2 μΩ cm but drastically rises to 10^{12} μΩ cm when the oxygen concentration increases.

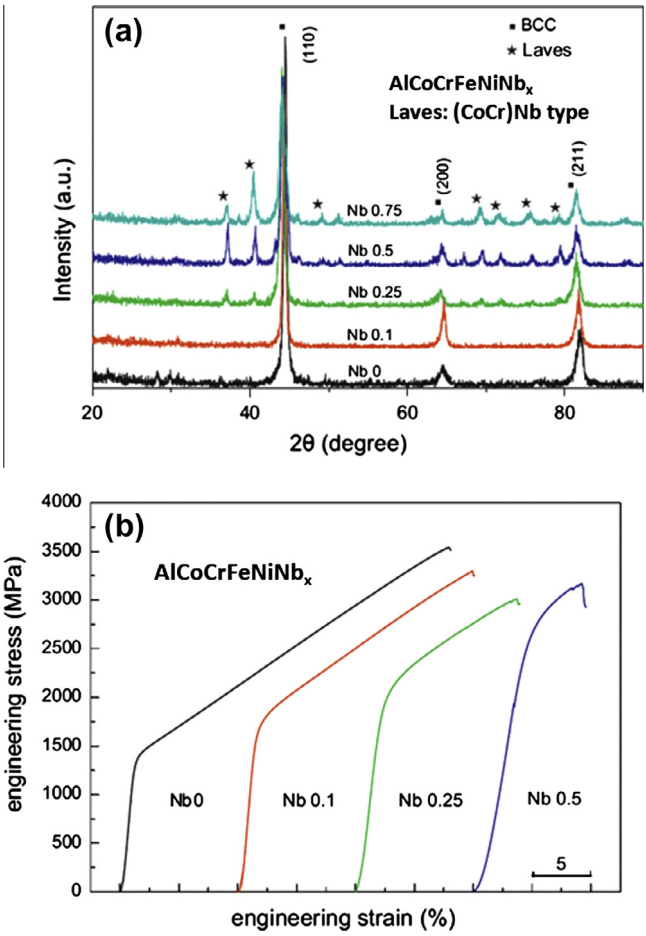

Fig. 4.1. (a) The addition of Nb elements into this HEA changes the original phase constitution, which yields the formation of ordered Laves phase besides solid solution phase. (b) The compressive stress–strain curves of the $AlCoCrFeNiNb_x$ rod samples with a diameter of 5 mm (x = 0, 0.1, 0.25, and 0.5) [135].

3.4. Electrochemical preparation

Yao et al. [125] prepared the BiFeCoNiMn HEA film using an electrochemical method. SEM shows that the surface of the film was grained, and the nano-rods with a high aspect ratio of 10 were obtained by potentiostatic electrodeposition in the N, N-dimethylformamide (DMF)–CH_3CN organic system. An amorphous film of $Bi_{19.3}Fe_{20.7}Co_{18.8}Ni_{22.0}Mn_{19.2}$ was obtained by potentiostatic electrodeposition at −2.0 V, but a main solid solution phase with a FCC structure was identified by XRD and selected area electron diffraction (SAED) patterns after the films were annealed under N_2 atmosphere. Also, the differential thermal analysis (DTA) curve verified that the film was crystallized by the heat treatment at 762 K. The as-deposited films show soft magnetic behavior, and hard magnetic anisotropy was observed in the annealed films. Limited work on preparing HEAs by electro-deposition was reported, but definitely, this fabrication route provide an innovative approach to develop new HEAs with unique properties.

4. Properties

The constitution of materials science usually contains four components, which forms the materials science tetrahedron. They include: (1) compositions and structures; (2) processing; (3) properties; and (4) performance. Sometimes, the characterization or the modeling and simulation can also be thought as the center of the tetrahedron. In this chapter, the mechanical, physical, and chemical properties of HEAs are described as follows.

4.1. Mechanical behavior

Superior structural alloys remain in a high demand for some extreme environmental engineering, particularly in the nuclear, turbine, and aerospace industries. Owing to microstructures, HEAs are reported with high hardness and high compressive strength both at room temperature and elevated temperatures [2,21,100,126–130,4]. HEAs have shown great integrated tensile properties, including both high ultimate tensile strength and reasonable ductility [100,131,132]. Overall, it has been reported that the FCC-structured HEAs exhibit low strength and high plasticity, and BCC-structured HEAs show high strength and low plasticity. Thus, the structure types are the dominant factor for controlling the strength or hardness of HEAs. In this chapter, we review some of the HEAs papers

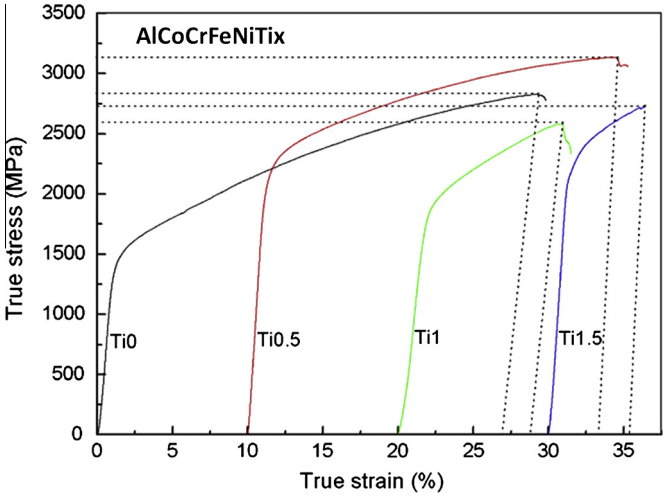

Fig. 4.2. Compressive true stress–strain curves of $AlCoCrFeNiTi_x$ alloy rods with a diameter of 5 mm [12].

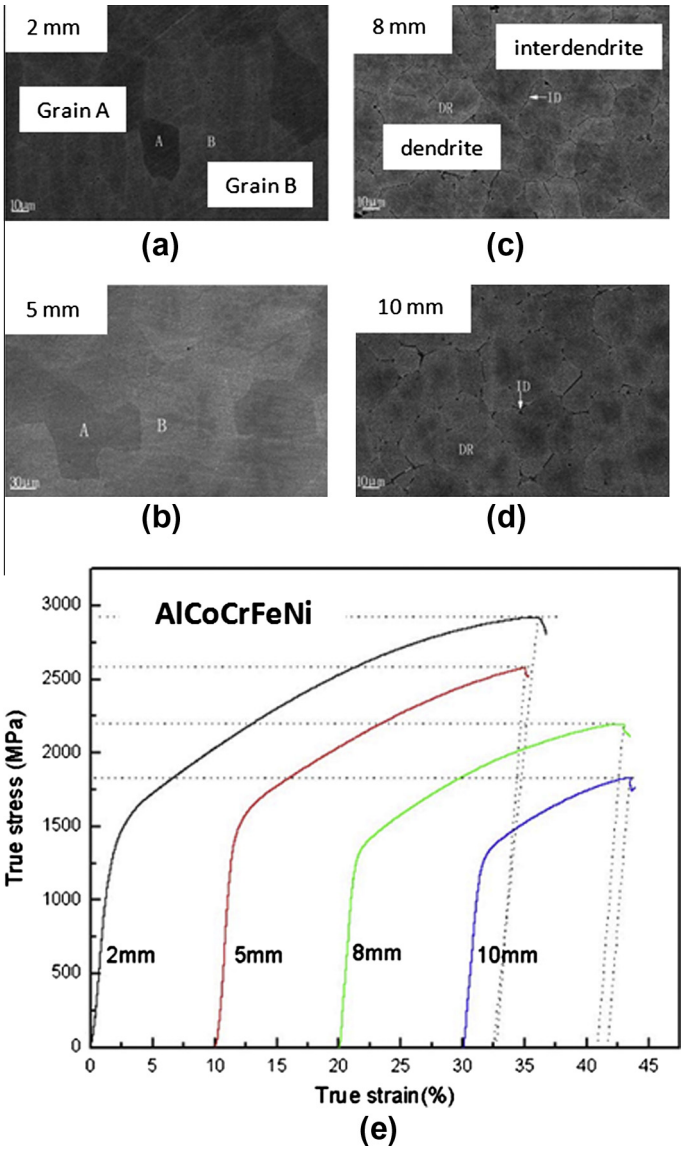

Fig. 4.3. As the cooling rate was increased, both the strength and the plasticity are enhanced significantly. Compressive true stress–true strain curves for the AlCoCrFeNi alloy samples with different diameters [129].

concerning mechanical properties: what has been reported, and what the deformation mechanisms are. Thus, the design and development of HEAs to the next level is suggested.

4.1.1. Mechanical behavior at room temperature

For room-temperature mechanical properties of HEAs, the yield strength can be varied from 300 MPa for the FCC-structured alloys, such as $CoCrCuFeNiTi_x$ system, to about 3000 MPa for the BCC-structured alloys, such as $AlCoCrFeNiTi_x$ system [12,13]. The values of Vickers hardness range from 100 to 900. The structure types are one of the dominant factors for controlling the mechanical

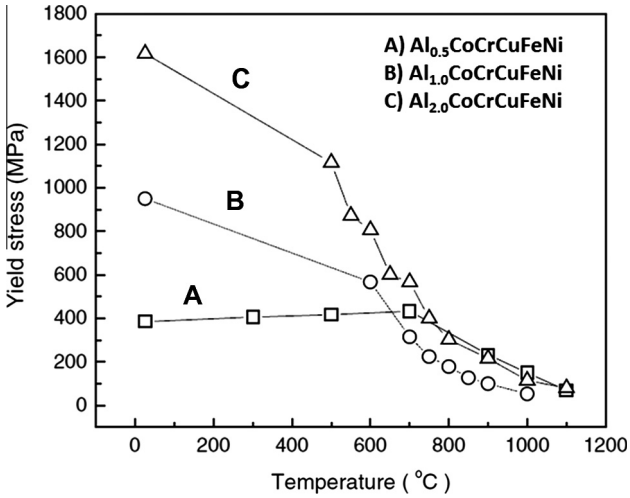

Fig. 4.4. Compressive yield strength of $Al_xCoCrCuFeNi$ alloy system tested at different temperatures: (A) $Al_{0.5}CoCrCuFeNi$, (B) $Al_{1.0}CoCrCuFeNi$, and (C) $Al_{2.0}CoCrCuFeNi$ alloys [2].

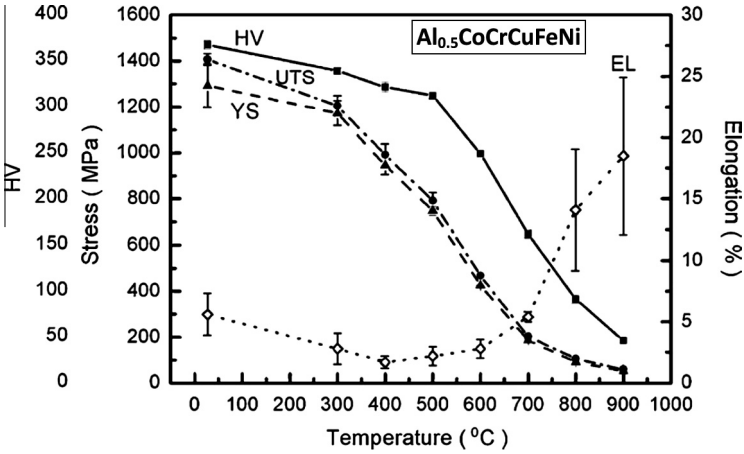

Fig. 4.5. Hardness, strengths, and elongation as a function of temperature for as-rolled samples [100].

behavior of HEAs at room temperature. Here, we would like to discuss two other effects on mechanical behavior.

4.1.1.1. Alloying effects. Like other conventional alloys, small amounts of alloying elements can also be added to HEAs to increase or decrease the strength, plasticity, hardness, etc. The addition of one alloying element to improve one property may have unintended effects on other properties. For example, in order to investigate the differences of effects of various alloying elements on mechanical properties of AlCoCrFeNi alloy, the effects of C, Mo, Nb, Si, Ti elements on AlCoCrFeNi alloy have been investigated systematically [12,133–135].

Ma and Zhang [135] studied the Nb alloying effect, finding that the microstructures and properties of the $AlCoCrFeNb_xNi$ HEAs became two phases in the prepared $AlCoCrFeNb_xNi$ HEAs: one is body-centered-cubic (BCC) solid solution phase (Fig. 4.1(a)); the other is the Laves phase of (CoCr)Nb type. The

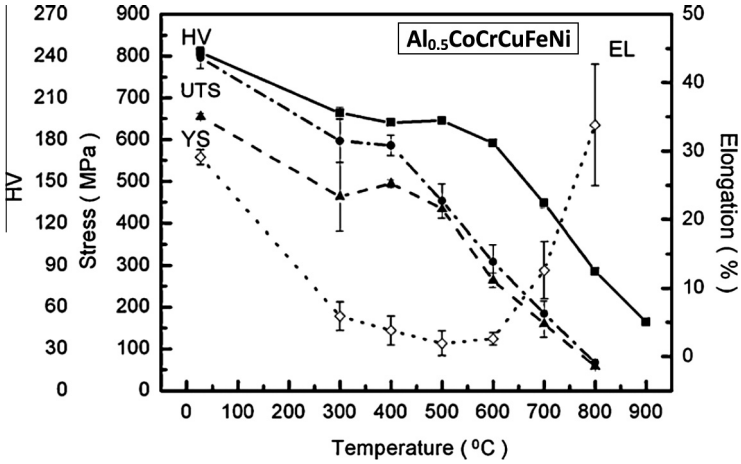

Fig. 4.6. Hardness, strengths, and elongation as a function of temperature for as annealed samples [100].

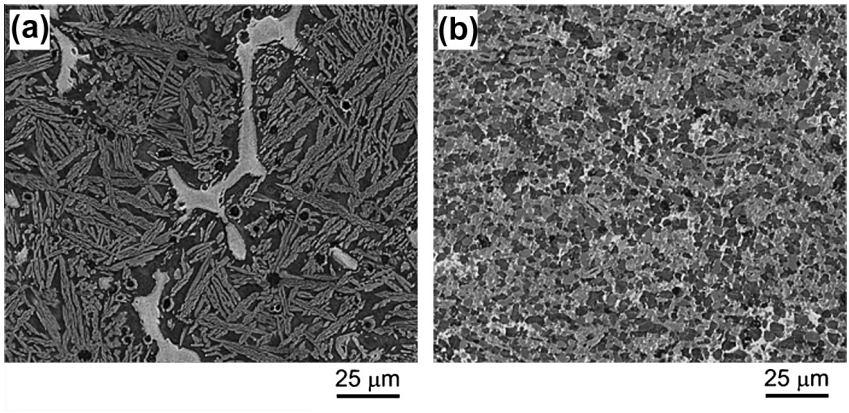

Fig. 4.7. Microstructure of the AlCrCuNiFeCo HEA in (a) as-cast and (b) hot-forged conditions [131].

microstructures of the alloy series vary from hypoeutectic to hypereutectic, and the compressive yield strength and Vickers hardness have an approximately linear increase with increasing Nb content as shown in Fig. 4.1(b) [135].

Zhou et al. [12] investigated the Ti alloying effect on $AlCoCrFeNiTi_x$, designed by using the strategy of the equiatomic ratio and high entropy of mixing. The alloy system is composed primarily of the BCC solid solution and possesses excellent room-temperature compressive mechanical properties, as shown in Fig. 4.2. Particularly for the $AlCoCrFeNiTi_{0.5}$ alloy, the yield stress, fracture strength, and plastic strain are as high as 2.26 GPa, 3.14 GPa, and 23.3%, respectively, which are superior to most of the high-strength alloys such as bulk metallic glasses [12,136].

4.1.1.2. Cooling-rate effects. The high cooling rates are effective for reducing the inter-dendrite composition segregation and making the microstructure more uniform, and the ductility can be improved while the yield strength has no significant change.

Wang et al. [129] studied the cooling rates effects on the microstructure and mechanical behaviors of a HEA of AlCoCrFeNi by preparing as-cast rod samples with different diameters. Smaller diameter

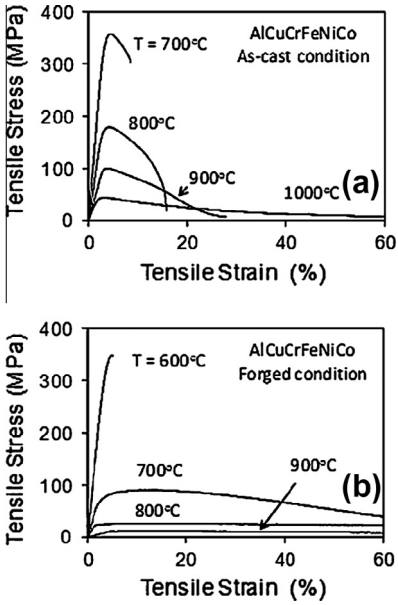

Fig. 4.8. Typical stress–strain curves of AlCoCrCuFeNi (a) the as-cast and (b) hot forged samples deformed at different temperatures and the initial strain rate of 10^{-3} s^{-1} [131].

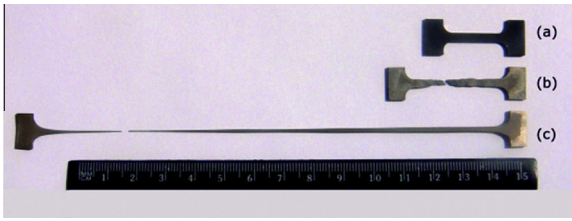

Fig. 4.9. Photographs of AlCoCrCuFeNi tensile samples after deformation at 1000 °C: (a) a non-deformed sample; (b) as-cast sample (δ = 77%); and (c) forged sample (δ = 864%). $\dot{\varepsilon} = 10^{-3}$ s^{-1} [131].

rod samples have higher cooling rate when using the same equipment. He found that the cast samples have the same phase of BCC solid solution while higher cooling rates lead to more uniform microstructures with reduced inter-dendrite composition segregation as shown in Fig. 4.3(a–d) [129]. With decreasing the casting diameter, which means the increasing cooling rate, both the strength and the plasticity are increased slightly, as shown in Fig. 4.3(e). From the fractographs, the samples exhibit features typical of cleavage fracture. The sample was fractured in the vertical direction to the side, which may be helpful to the large plasticity for higher cooling rate specimens. This work may contribute to exploring the application of HEAs, especially when seeking different mechanical properties with the same chemical composition.

4.1.2. Mechanical behavior at elevated temperatures

The high-temperature properties of the HEAs were also extensively studied [14,100,127,131]. Like, conventional alloys, the microstructures and mechanical properties can be tuned to achieve the optimum. Fig. 4.4 shows that the yield strength decreases with increasing the testing temperature [2]. It is seen that the low Al-content alloy exhibits low yield strength, but it decreases slowly with increasing temperature. Fig. 4.5 presents the change in mechanical properties of the $Al_{0.5}CoCrCuFeNi$ HEA of the

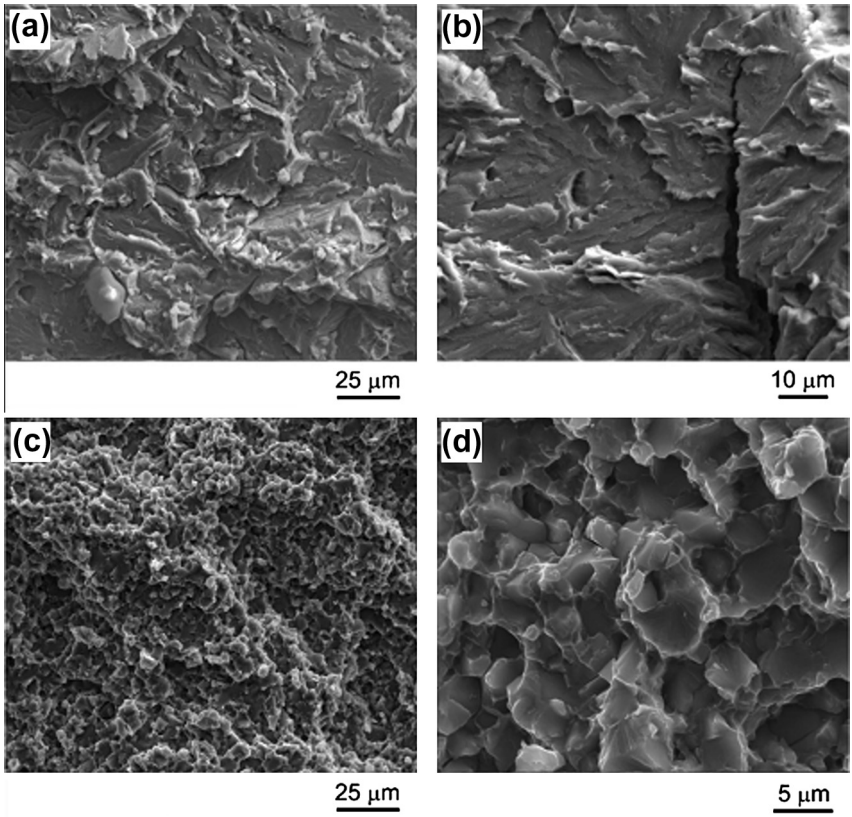

Fig. 4.10. SEM images of the AlCoCrCuFeNi fracture surfaces of tensile samples after tensile deformation at room temperature: (a and b) as-cast and (c and d) hot-forged conditions [131].

rolled sample as the temperature increased [100]. Fig. 4.6 shows mechanical properties of the $Al_{0.5}$-CoCrCuFeNi HEA of annealed samples as a function of the testing temperature [100]. It is shown that, after annealing, the strength and hardness decrease while the elongation increases, and the strength decreases slowly with increasing the temperature, which means that heat-treatment will have the most impact on the mechanical properties, especially at elevated temperatures. We would like to discuss the heat-treatment effect on high temperature properties of HEAs, including high-performance HEAs at elevated temperatures, called refractory HEAs.

4.1.2.1. Heat-treatment effects. Fig. 4.7 presents the microstructure of the AlCrCuNiFeCo HEA in (a) as-cast and (b) hot-forged conditions [131]. Considerable refinement of the cast microstructure was observed after extensive multi-step forging at 950 °C. Fig. 4.8 exhibits the typical stress–strain curves of the as-cast (a) and hot-forged (b) samples deformed at different temperatures with an initial strain rate of 10^{-3} s^{-1} [131]. We find that, after forging, the alloy is considerably softer and much more deformable than the as-cast alloy. Fig. 4.9 exhibits the photographs of tensile samples after deformation at 1000 °C: (a) a non-deformed sample; (b) an as-cast sample (tensile ductility, d = 77%); and (c) a forged sample (d = 864%) at a strain rate of 10^{-3} s^{-1}. The forged sample demonstrates highly homogeneous flow, great resistance to neck formation, and exceptionally high elongation of 864%. Fig. 4.10 presents the corresponding SEM images of the fracture surfaces of samples after tensile-testing deformation at room temperature: (a and b) as-cast and (c and d) hot-forged conditions [131]. At low magnification, the as-cast alloy sample has a coarse-faceted appearance [Fig. 4.10(a)], whereas the forged

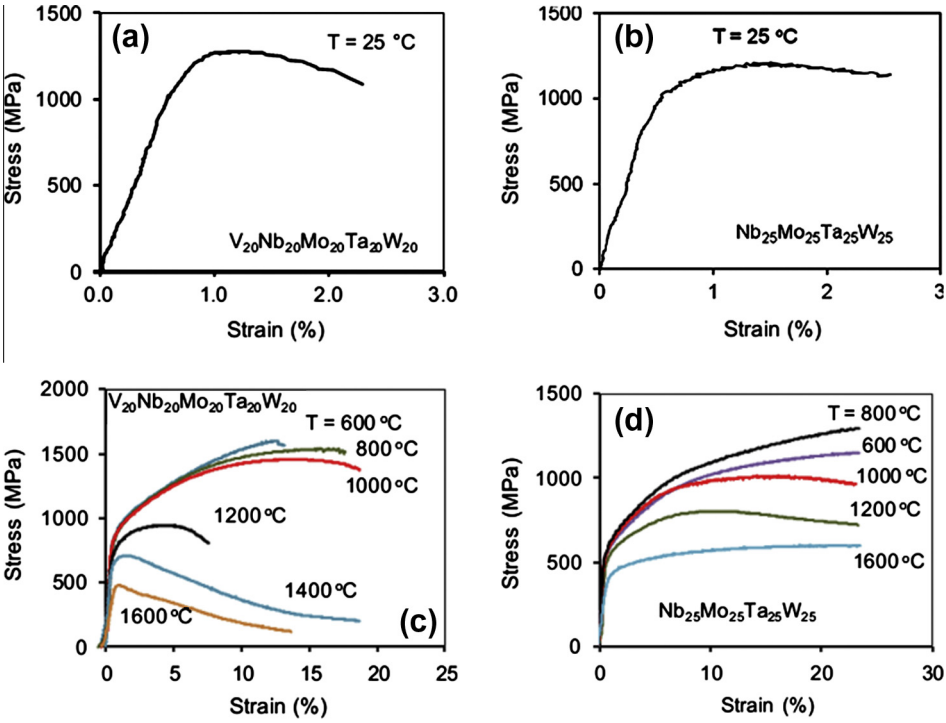

Fig. 4.11. Compressive engineering stress–strain curves of NbMoTaW and VNbMoTaW HEAs at room temperature and high temperatures [14].

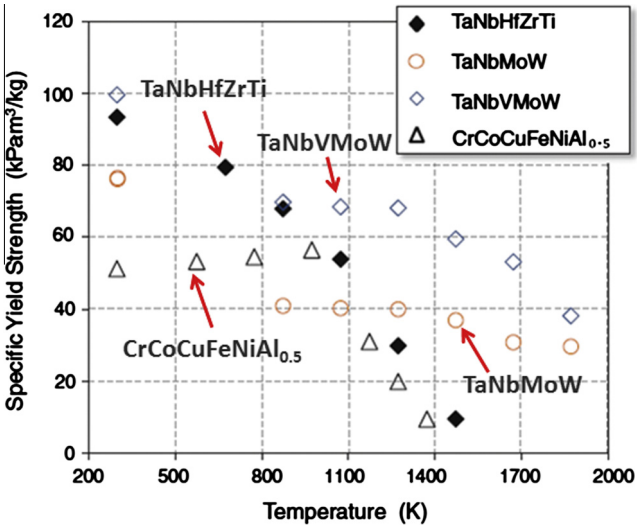

Fig. 4.12. The temperature dependence of the specific yield-strength of the TaNbHfZrTi alloy in comparison with that for TaNbMoW, TaNbVMoW, and $CrCoCuFeNiAl_{0.5}$ cast alloys [128].

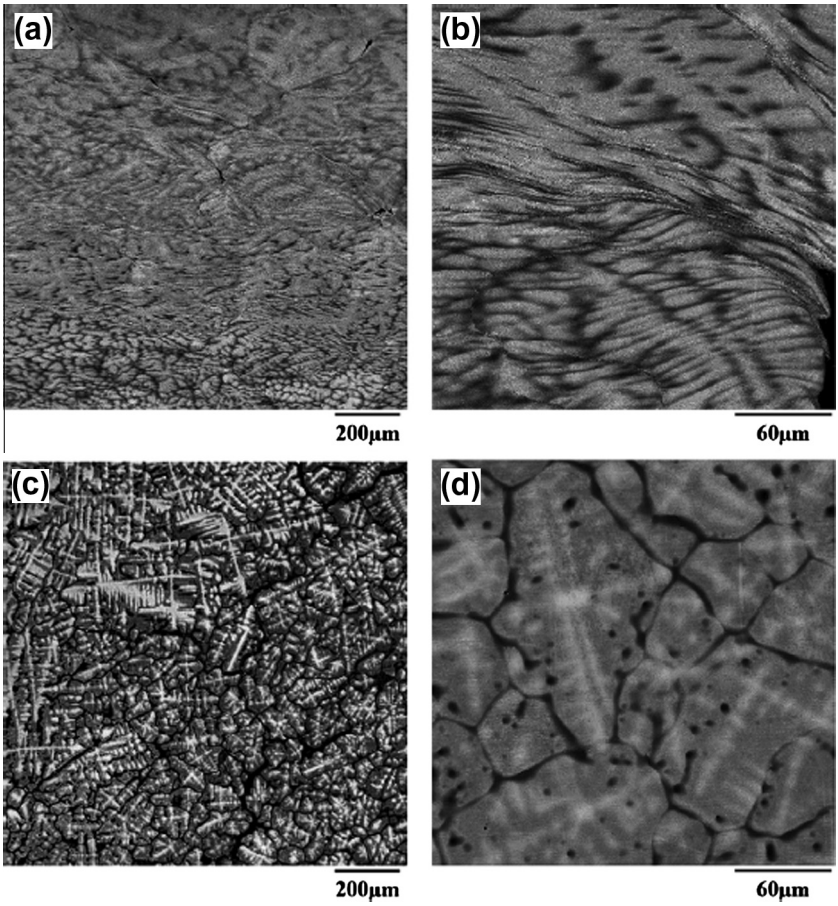

Fig. 4.13. The SEM backscatter images of the NbMoTaW (a and b) and VNbMoTaW (c and d) HEAs after the deformation at 1,673 K. [14].

sample has fine granular appearance [Fig. 4.10(c)]. This observation is consistent with the much smaller grain/particle size of the forged condition than the as-cast condition. High magnification images confirm brittle, quasi-cleavage, fracture of the as-cast alloy, with such characteristic features as flat facets, angular faceted steps, river-pattern markings, cleavage feathers, and tongues [Fig. 4.10(b)]. At the same time, higher-magnification images of the forged sample confirm a mixed type of brittle and ductile fracture [Fig. 4.10(d)]. The brittle type fracture is reflected by the presence of flat facets with characteristic river-pattern markings inside large dimples while the ductile type fracture is reflected in numerous dimples of different diameters surrounding the flat facets. It is likely that, during tensile deformation of the forged sample, cracks are formed at the interfaces of the BCC and FCC particles by brittle fracture, and then the crack opening into voids occurs by plastic deformation of nearest, more ductile regions [131].

4.1.2.2. Refractory HEAs. Currently, Ni-based superalloys already have the great combination of elevated temperature properties, including creep resistance, corrosion resistance, and damage tolerance, but operating temperatures are reaching the theoretical limits of these materials. The high entropy alloying (HEA) approach was used to develop new refractory alloys, which contain several principal

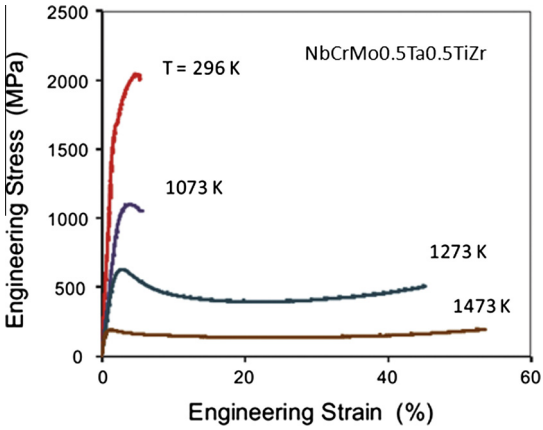

Fig. 4.14. The engineering stress–strain compression curves of the $NbCrMo_{0.5}Ta_{0.5}TiZr$ alloy samples after HIP at 296 K, 1073 K, 1273 K, and 1473 K [127].

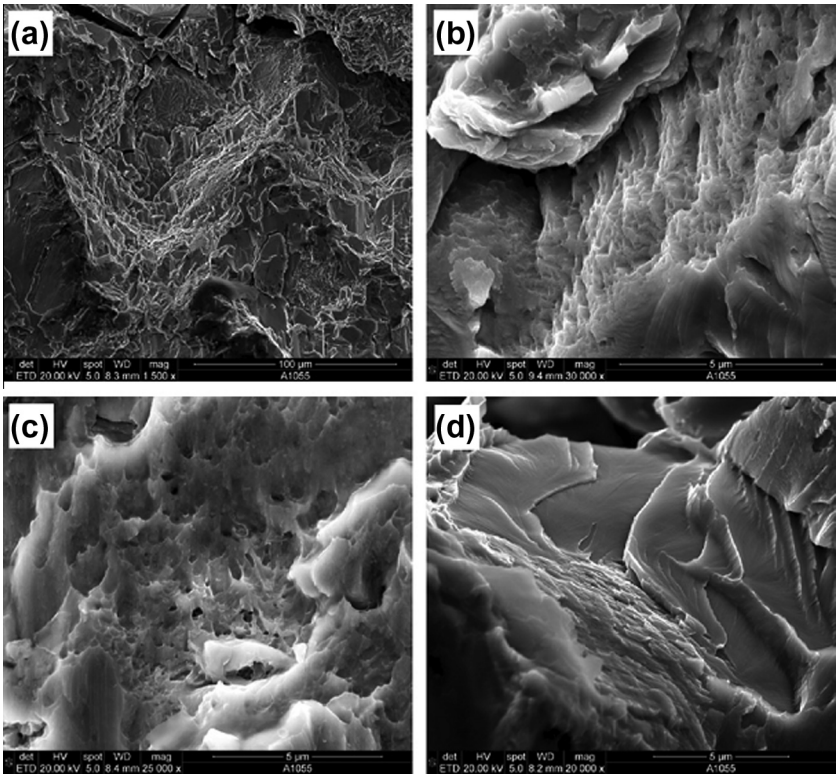

Fig. 4.15. SEM secondary electron images of the fracture surface of a $NbCrMo_{0.5}Ta_{0.5}TiZr$ alloy samples after compression deformation at room temperature [127].

alloying elements at near equiatomic concentrations, using new metallic materials with higher melting points, such as refractory molybdenum (Mo) and niobium (Nb) alloys [14,16,126–128].

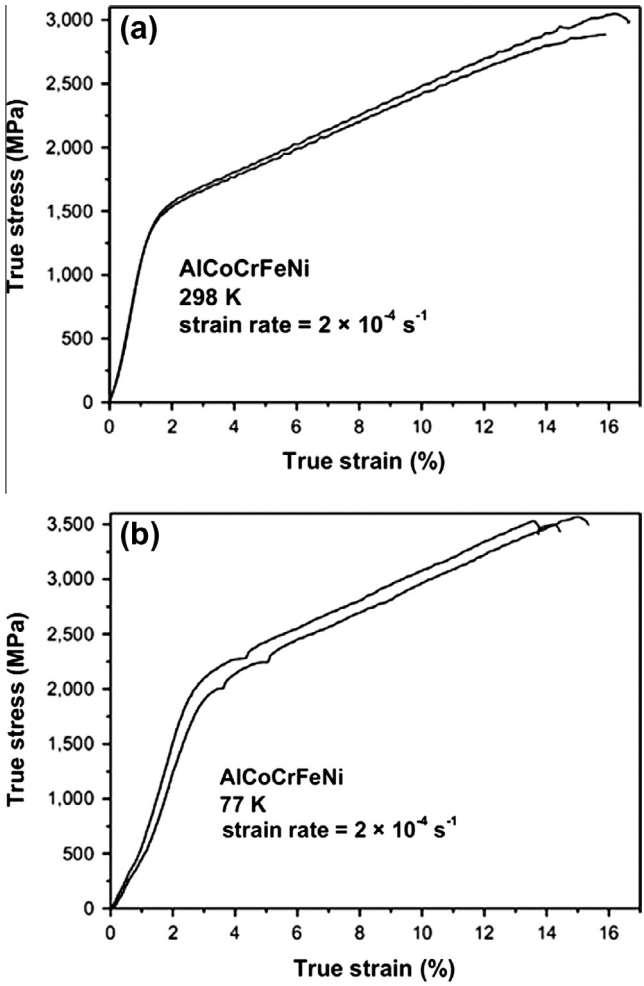

Fig. 4.16. The compressive true stress–strain curves of the AlCoCrFeNi HEA at (a) 298 and (b) 77 K. The yield strengths and fracture strengths at cryogenic temperatures increase distinguishingly, compared to the corresponding mechanical properties at ambient temperature [137].

Senkov et al. [14] reported the yield strength of NbMoTaW and VNbMoTaW alloys at elevated temperatures as shown in Fig. 4.11. From Fig. 4.11, we can see that the V addition is beneficial to increasing the strength, but not suitable for the heat-softening resistance. Fig. 4.12 exhibits the specific yield-strength change with increasing the temperature for the TaNbHfZrTi, TaNbMoW, TaNbVMoW, and $CrCoCuFeNiAl_{0.5}$ cast alloys [128]. It can be seen that the high specific yield strength of the $CrCoCuFeNiAl_{0.5}$ HEAs can be sustained over to 1100 K, and the TaNbMoW HEA can sustain its high specific strength to 1800 K. Fig. 4.13 shows the backscatter images of the NbMoTaW and VNbMoTaW HEAs after the deformation at 1673 K [14].

Lower density and better room temperature ductility are required if we seek for applications in the aerospace engineering. By replacing V, Ta, and W in the NbMoTaW and VNbMoTaW alloys with lighter Cr, Mo, and Zr, respectively, the density of the new refractory $NbCrMo_{0.5}Ta_{0.5}TiZr$ HEAs alloy was reduced to 8.2 g/cm^3. In addition, the new alloy showed improved room temperature ductility, relative to the NbMoTaW and VNbMoTaW alloys. Fig. 4.14 exhibits the engineering stress–strain compression

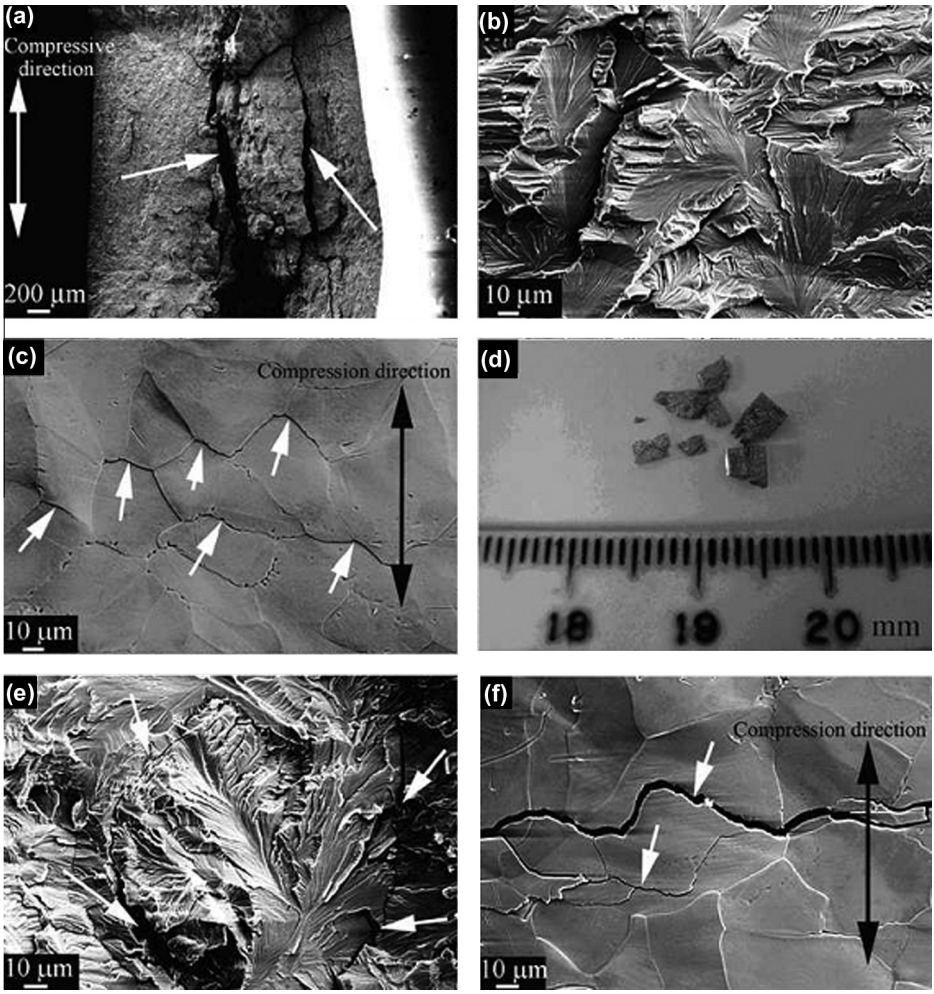

Fig. 4.17. The low and high magnifications for the fracture surfaces of the AlCoCrFeNi HEA at 298 K shown in (a) and (b), respectively; The lateral surface of the deformed sample of the AlCoCrFeNi HEA at 298 K shown in (c); The low and high magnifications for the fracture surfaces of the AlCoCrFeNi HEA at 77 K shown in (d) and (e), respectively; The lateral surface of the deformed sample of the AlCoCrFeNi HEA at 77 K shown in (f) [137].

curves of the $NbCrMo_{0.5}Ta_{0.5}TiZr$ alloy samples after HIP at 296 K, 1073 K, 1273 K, and 1473 K [127]. During deformation at 296 K, the yield strength was 1595 MPa and continuous strengthening occurred until the alloy fractured by localized shearing at maximum strength of 2046 MPa accumulating about a 5% strain. During testing at $T = 1073$ K, yield strength decreased to 983 MPa, the peak strength of 1100 MPa was achieved at a strain of 4.2%, and the sample fractured by shearing at a strain of about 6%, after a decrease in strength to 1050 MPa. An increase in the testing temperature to 1273 K resulted in a considerable softening of the alloy after a short stage of strain hardening. At this temperature, yield strength ($\sigma_{0.2}$) = 546 MPa, compressive strength (σ_p) = 630 MPa, and the minimum strength achieved during strain softening was 393 MPa after a plastic strain of about 22%. At this temperature, the sample did not fracture. An increase in the temperature to 1473 K, led to a further decrease in the flow stress of the alloy, and $\sigma_{0.2}$ was 170 MPa. The peak stress of 190 MPa was reached shortly after yielding, followed by weak softening and a steady state flow at the minimum strength

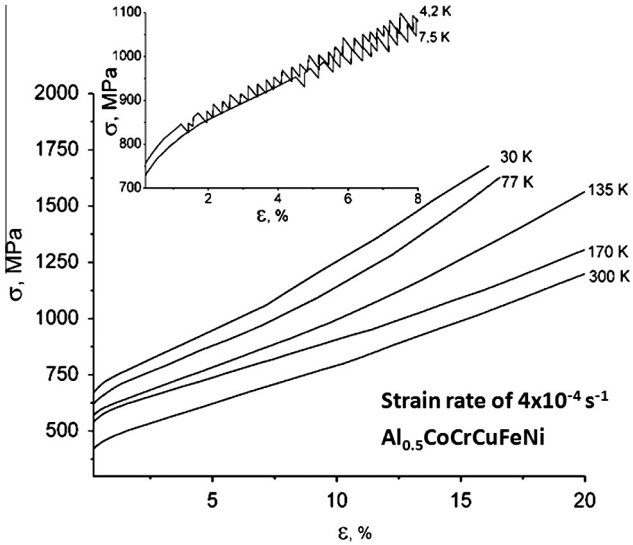

Fig. 4.18. At all temperatures to 4.2 K, the $Al_{0.5}CoCuCrFeNi$ HEA possesses high plasticity under compression. At temperatures below 15 K, the curves show a serrated shape. The inserted figure illustrates a typical serrated stress–strain curve [138].

(σ_{min}) = 135 MPa. No sample fracture occurred at this temperature. Fig. 4.15 presents the SEM secondary-electron images of the fracture surface of a $NbCrMo_{0.5}Ta_{0.5}TiZr$ alloy samples after compression deformation at room temperature [127]. It shows a combination of plastic and brittle deformation mechanism. The formation of dimples is convincing evidence of plastic deformation [Fig. 4.15(b and c)] while the microstructure of teared pieces is the symbol of quasi-cleavage fracture of the FCC (Laves) phase, as well as along the interfaces [Fig. 4.15(a and d)].

In summary, refractory HEA is a unique idea and relatively new field. Compared to compositions with 3d elements, refractory HEAs (4d elements) show exceptionally bright mechanical properties, especially at elevated temperatures. More research fields including new compositions and fracture mechanism need to be explored.

4.1.3. Mechanical behavior at cryogenic temperatures

It is fully acknowledged that the low-temperature mechanical properties are particularly critical for real applications of metallic alloys. The mechanical behaviors of HEAs at cryogenic temperatures are yet to be investigated in detail. It is also known that FCC metal does not show a ductile–brittle transition temperature (DBTT), so should we expect the same for FCC HEAs? Meanwhile, because DBTT is known for BCC metals, has anybody done work on deformation of BCC HEAs at low *T*? The aim of this chapter is to review the compressive characteristics of both BCC and FCC HEAs at cryogenic temperatures.

Qiao et al. studied the compressive characteristics of a single-phase BCC HEA with the composition of AlCoCrFeNi at 77 K [137]. For the AlCoCrFeNi HEA, there is no obvious ductile to brittle transition even the temperature is lowered to 77 K. Comparing with the compression properties at different temperatures, the yielding strengths and fracture strengths of the AlCoCrFeNi HEA increase by 29.7% and 19.9%, respectively, when the temperatures decrease from 298 to 77 K, as shown in Fig. 4.16. However, the fracture strains change gently while the fracture modes at 298 and 77 K are intergranular and transgranular, respectively as shown in Fig. 4.17 [137]. This means that the DBTT of the AlCoCrFeNi BCC HEA is lower than 77 K.

Laktionova et al. [138] studied the deformation peculiarities of $Al_{0.5}CoCrCuFeNi$ alloy by in a temperature range from 300 K to 4.2 K. The alloy has been found to provide a high strength and plasticity greater than 30% in this temperature range: the yield stress amounts to 450 MPa for 300 K and

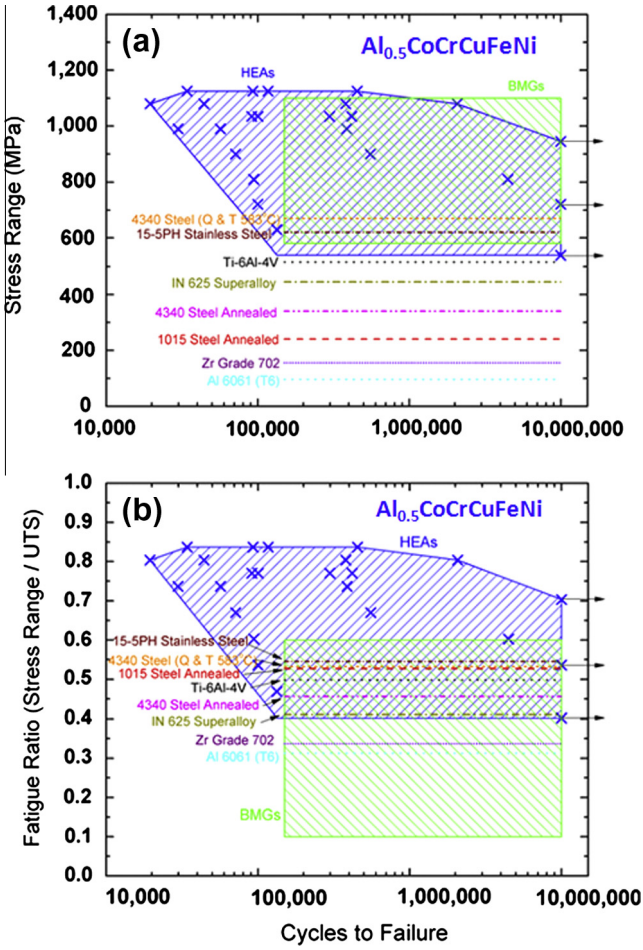

Fig. 4.19. S–N curves comparing the fatigue ratios of the $Al_{0.5}CoCrCuFeNi$ HEA, other conventional alloys and bulk metallic glasses [139].

750 MPa for 4.2 K as shown in Fig. 4.18. At temperatures below 15 K, the smooth behavior of the stress–strain curves changes to the jump-like one, called serration behavior. This trend is proposed to be related to the change of deformation mechanisms, which is discussed in details in Section 5. Thus, FCC HEAs do not exhibit DBTT, like FCC metals.

4.1.4. Fatigue behavior

Many potential applications for HEAs, such as aircraft engine components, frequently encounter cyclic loading. If we seek for the application in the aerospace industry or other area, besides monotonic loading, the fatigue behavior and lifetime prediction are one of the most significant factors, which are required to be studied and explored, yet rarely reported. The limited publication published so far is concerning the fatigue behavior of $Al_{0.5}CoCrCuFeNi$ HEAs, discussed as below.

Hemphill et al. [139] studied fatigue behavior of the $Al_{0.5}CoCrCuFeNi$ HEA and compared the results to many conventional alloys, such as steels, titanium alloys, and advanced BMGs. Fig. 4.19(a) shows that a typical stress range vs. the number of cycles to failure (S–N) curves comparing fatigue ratios [fatigue ratio = fatigue endurance limit/ultimate tensile strength (UTS)) of the $Al_{0.5}CoCrCuFeNi$ HEA

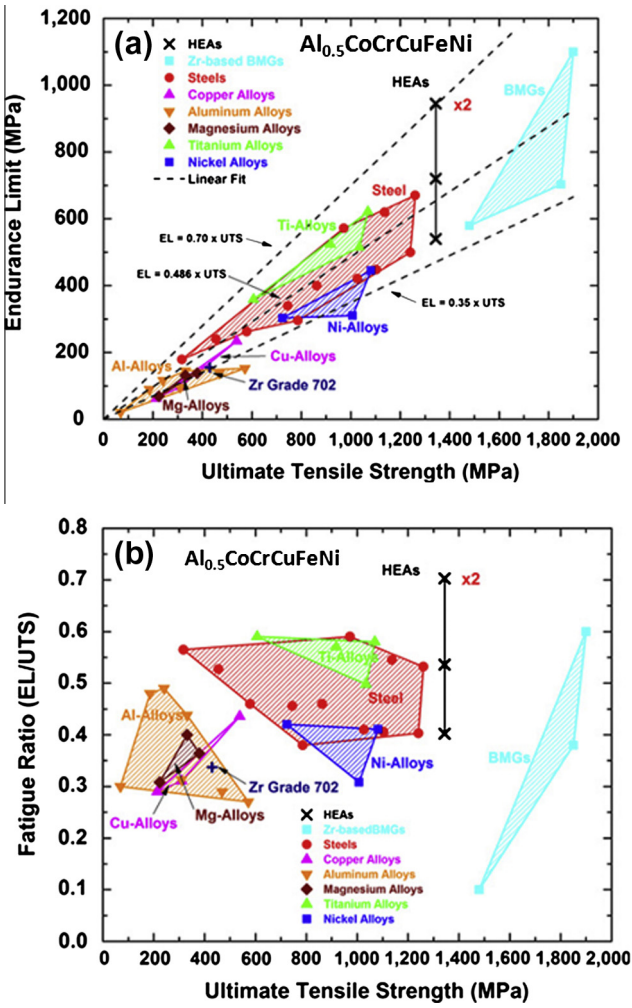

Fig. 4.20. Plots comparing (a) the fatigue endurance limits and (b) the fatigue ratios of the $Al_{0.5}CoCrCuFeNi$ HEA as a function of the UTS of other structural materials and BMGs [139].

to other conventional alloys, and BMGs [140]. The lower bound of the fatigue ratios of HEAs compares favorably to those of steels, titanium, and nickel alloys, and outperforms zirconium alloys as well as some of the Zr-based BMGs. Moreover, for some materials, such as ultra-high strength steels and wrought aluminum alloys, their high tensile strengths result in lower fatigue ratios due to their brittle nature. The strong group (which is defined as samples in the group contain fewer fabrication defects and can reveal the intrinsic fatigue behavior of the HEA) of HEAs tends to outperform these materials by displaying a greater fatigue ratio than materials with comparable tensile strengths due to the reduced number of defects. The upper bound of the fatigue limit of HEAs is significantly higher than that of other conventional alloys and BMGs, showing that HEAs have the potential to outperform these materials in structural applications with improved fabrication and processing.

Fig. 4.19(a) illustrates the fatigue-endurance limits for the $Al_{0.5}CoCrCuFeNi$ HEA as a function of UTS. One reason for the high fatigue strength of HEAs is the high tensile strength of these materials. It can be clearly seen that as the UTS increases the fatigue-endurance limit also increases in a linear fashion, approximately equal to 0.5 for most materials [139]. HEAs follow a similar pattern and even

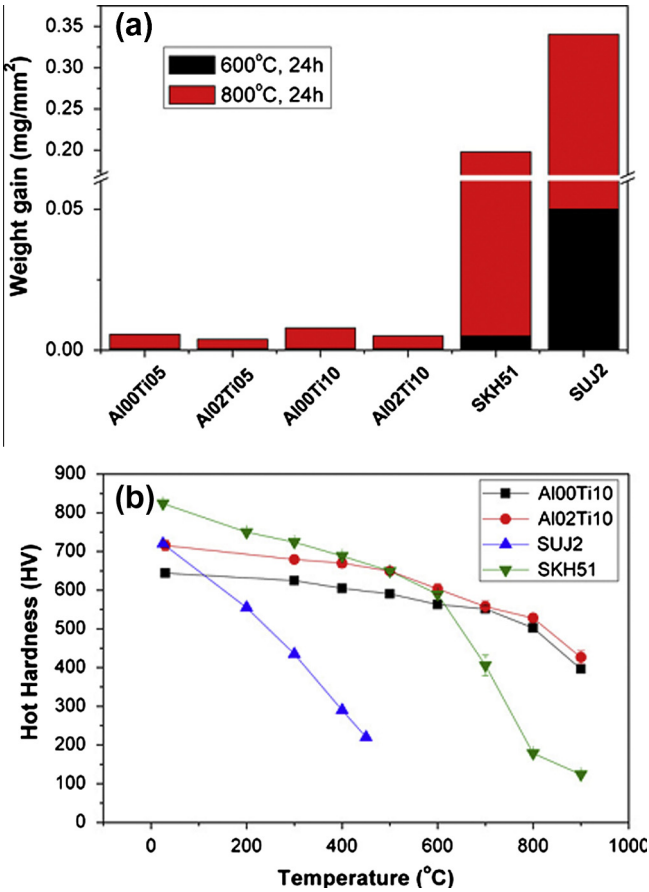

Fig. 4.21. (a) Weight gain test of Al00Ti05 ($Co_{1.5}CrFeNi_{1.5}Ti_{0.5}$), Al02Ti05 ($Al_{0.2}Co_{1.5}CrFeNi_{1.5}Ti_{0.5}$), Al00Ti10 ($Co_{1.5}CrFeNi_{1.5}Ti$), Al02Ti10 ($Al_{0.2}Co_{1.5}CrFeNi_{1.5}Ti$), SUJ2 (AISI 52100) and SKH51 (AISI M2) specimens at 600°C (873 K) and 800 °C (1073 K) for 24 h. The data is presented as weight increase per unit area after test. (b) Hot hardness vs. temperature plots for Al00Ti10, Al02Ti10, SUJ2 and SKH51 specimens from room temperature to 900 °C (1173 K) [140].

exceed this ratio, with an upper bound of 0.703. To better compare the fatigue performance of HEAs with other materials with respect to their UTS, the fatigue ratios are used as shown in Fig. 4.19(b). Fig. 4.20(a) illustrates this relationship comparing the fatigue-endurance limit vs. UTS. Its high tensile strength may contribute to the high fatigue strengths of HEAs. It can be clearly seen that as the UTS increases the endurance limit will also increase in a linear fashion, approximately equal to 0.5 for most materials [139]. HEAs follow a similar pattern and even exceed this ratio, with an upper bound of 0.703 as shown in Fig. 4.20(b).

These results are highly encouraging for excellent fatigue resistance in HEAs and with potential long fatigue life, even at stresses approaching the ultimate stress. Because of the lack of the literature on the fatigue behavior of HEAs, the focus of the continuing studies should be placed on the data points that show an unexpectedly long fatigue life. If the necessary information on the fatigue resistance can be found and a prediction model for fatigue specimens can be developed, HEAs have a bright future in various applications for components in fatigue environments.

4.1.5. Wear behavior

Although it is cheaper than most superalloys and Ti alloys, the cost of HEAs are still higher than that of steel, owing to the use of some expensive elements, such as Co and Cu. Thus, HEAs show more

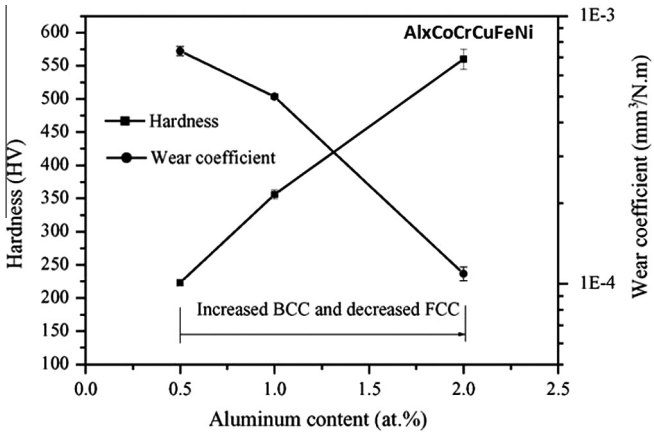

Fig. 4.22. Vickers hardness and wear coefficient of $Al_xCoCrCuFeNi$ alloys with different aluminum contents [141].

competitive and potential for use in tools, molds, and structural components, so wear is a fundamental phenomenon in these applications. Tests on the wear behavior of HEAs have been conducted under abrasive conditions and adhesive conditions.

Chuang et al. [140] reported that the wear resistance of the $Co_{1.5}CrFeNi_{1.5}Ti$ and $Al_{0.2}Co_{1.5}CrFeNi_{1.5}Ti$ alloys are better than that of conventional wear-resistant steels with similar hardness as shown in Fig. 4.21. Increasing the molar ratio of Ti significantly increases the volume fraction of η precipitates. The addition of Al decreases the amount of the coarse η phase in the interdendritic (ID) regions and triggers the formation of the needle-like η phase with Widmanstätten structures in the Al-rich regions of the ID [140]. The difficulty in effectively relocating Al results in this phenomenon. The hardness values of $Co_{1.5}CrFeNi_{1.5}Ti$ and $Al_{0.2}Co_{1.5}CrFeNi_{1.5}Ti$ alloys are HV 654 and HV 717, respectively, because of the strengthening effect from the hard η phase [140]. The excellent anti-oxidation property and resistance to thermal softening in these HEAs are proposed to be the main reasons for the excellent wear resistance.

Alloying can affect the wear behavior of HEAs. Wu et al. [141] studied adhesive wear behavior of $Al_xCoCrCuFeNi$ HEAs as a function of aluminum content. He found that, for higher Al content, the worn surface is smooth and yields fine debris with a high oxygen content, which gives a large improvement in wear resistance as shown in Fig. 4.22. The reason of this improvement is attributed to its high hardness, which not only resists plastic deformation and delamination, but also brings about the oxidative wear in which oxide film could assist the wear resistance [141].

4.1.6. Summary

Up to now, some HEAs with unique properties have been reported: e.g., high-strength body-centered-cubic (BCC) AlCoCrFeNi HEAs at room temperature, and refractory VNbMoTaW at elevated temperatures. For room-temperature mechanical properties of HEAs, the yield strength can be varied from 300 MPa for the FCC-structured alloys to about 3000 MPa for the BCC-structured alloys. The alloy and cooling-rate effects can change the microstructures and influence mechanical properties. At elevated temperatures, the high specific yield strength of the $Al_{0.5}CrCoCuFeNi$ HEAs can be sustained over to 1100 K, and the TaNbMoW refractory HEA can sustain its high specific strength to 1800 K. Like conventional alloys, heat-treatment process is also one of the most crucial factors on affecting mechanical properties. At cryogenic temperatures, for the $Al_{0.5}CoCrCuFeNi$ HEA, there is no obvious ductile to brittle transition even the temperature is lowered to 4.2 K.

On the other hand, HEAs also possess both high fatigue resistance and high wear resistance. For fatigue behavior, $Al_{0.5}CoCrCuFeNi$ HEAs was studied and compared to many conventional alloys, such as steels, titanium alloys, and advanced bulk metallic glasses. The $Al_{0.5}CoCrCuFeNi$ HEAs could have supreme fatigue resistance outperforming conventional alloys and BMGs, if the inclusion contents

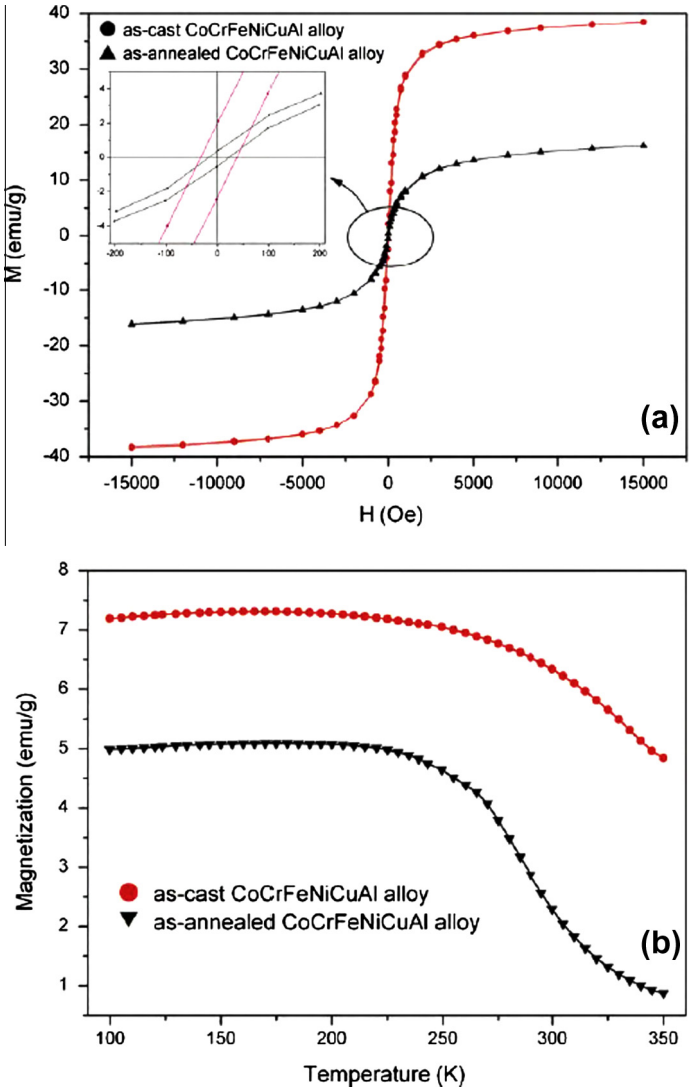

Fig. 4.23. Magnetization curves of the as-cast and as-annealed CoCrFeNiCuAl high entropy alloys: (a) the hysteresis loops and (b) the temperature dependence of magnetization ($M(T)$) curves while cooling the alloys at 200 Oe [142].

can be reduced in the HEA. For wear behavior, the wear resistances of the $Co_{1.5}CrFeNi_{1.5}Ti$ and $Al_{0.2}$-$Co_{1.5}CrFeNi_{1.5}Ti$ alloys are better than that of conventional wear-resistant steels with similar hardness.

4.2. Physical behavior

Ma and Zhang [135] reported that the $AlCoCrFeNb_xNi$ ($x = 0$, 0.1, 0.25, 0.5, and 0.75) HEAs exhibit ferromagnetic properties, because their permeability (χ) is in the range of 2.0×10^{-2}–3.0×10^{-3}. While for the $Ti_{0.8}CoCrCuFeNi$ and TiCoCrCuFeNi alloys, they exhibit superparamagnetic properties [13], which is due to the nano-particles forming in the alloy.

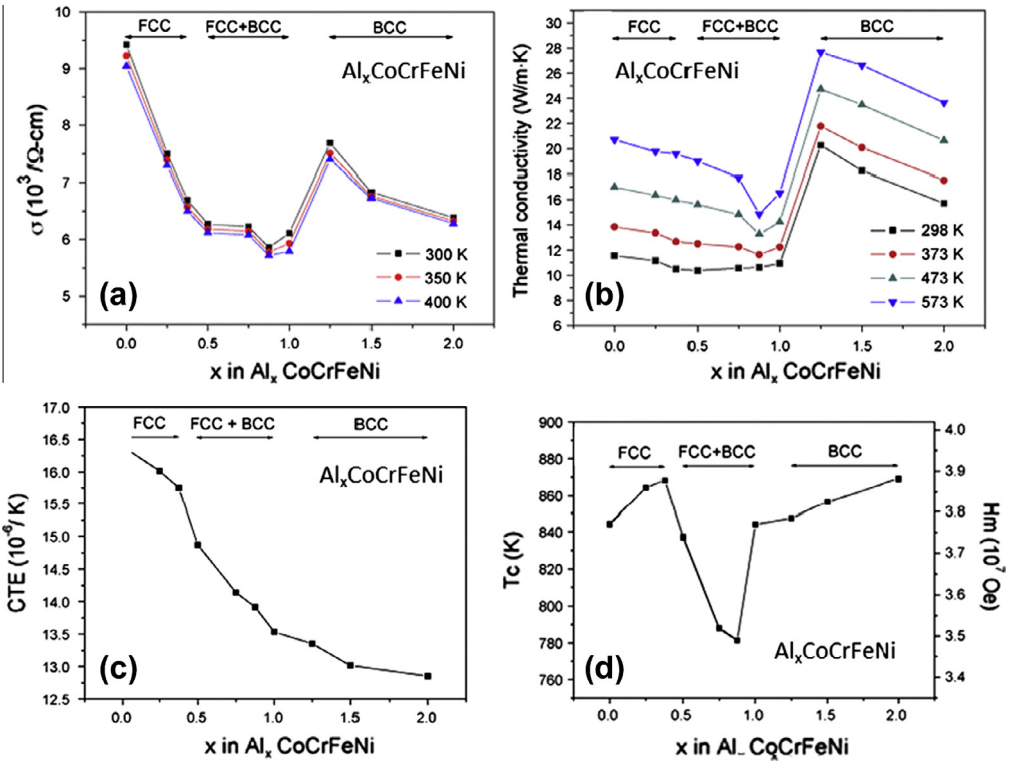

Fig. 4.24. Electrical conductivity σ (a), thermal conductivity (b), thermal-expansion (CTE) (c), and Curie temperature and molecular field as a function of x in $Al_xCoCrFeNi$ alloys (d) [144].

Fig. 4.23 presents the magnetic hysteresis loops of the as-cast and as-annealed CoCrFeNiCuAl HEAs measured at room temperature. Both alloys show excellent soft magnetic properties. Saturated magnetizations (M_s), remanence ratio (M_r/M_s), and coercivity (H_c) of the as-cast and as-annealed alloys are estimated to be 38.18 emu/g, 5.98%, 45 Oe, and 16.08 emu/g, 3.01%, 15 Oe, respectively. Zhang and coworkers [13] had investigated the magnetic properties of $CoCrCuFeNiTi_x$ alloys, which exhibited saturated magnetization lower than 2 emu/g. Compared with the magnetic properties of bulk metals, both the as-cast and as-annealed CoCrFeNiCuAl alloys show high M_s and low H_c. The alloys present comparable magnetic properties with the soft ferrite and can be utilized as soft magnetic materials. On the other hand, the as-cast alloy exhibits a similar super-paramagnetic curve, which can be attributed to the nanoscaled microstructure. The decrement of M_s in the as-annealed alloy resulted from the structure coarsening and phase transformation. Fig. 4.23(b) depicts the temperature dependence of magnetization [$M(T)$] curves of the as-cast and as-annealed alloys, while cooling them to liquid nitrogen at 200 Oe. The results clearly reveal a ferromagnetic transition of both alloys at all temperatures. The $M(T)$ curves also indicate the high Curie temperature (T_c) of both alloys [142].

Chen and Kao [143] reported that the electrical resistivity of the $Al_{2.08}CoCrFeNi$ HEA is very close to a constant over a temperature range from 4.2 to 360 K. The average temperature coefficient of resistivity (TCR) from 4.2 to 360 K is 72 ppm/K, with a half-parabolic shape in its resistivity-temperature curve that is similar to Manganin (Manganin is a trademarked name for an alloy of $Cu_{86}Mn_{12}Ni_2$). It was first developed by Edward Weston in 1892. Manganin foils and wires are used in the manufacture of resistors, particularly ammeter shunts, because of their virtually zero temperature coefficient of resistance value and long-term stability. Several Manganin resistors served as the legal standard for the ohm in the United States from 1901 to 1990. Manganin wires are also used as an electrical

conductor in cryogenic systems, minimizing the heat transfer between points, which need electrical connections. Manganin is also used in gauges for studying high-pressure shock waves (such as those generated from the detonation of explosives because it has low strain sensitivity but high hydrostatic pressure sensitivity. It indicates that the phonon effect on this alloy keeps nearly the same through this temperature range.

Chou et al. [144] reported the electrical conductivity, σ, as shown in Fig. 4.24(a), thermal conductivity, in Fig. 4.24(b), the coefficient of thermal expansion (CTE) in Fig. 4.24(c), and the Curie temperature, T_c, together with molecular field, in Fig. 4.24(d), as a function of composition, x, in the $Al_xCoCrFeNi$ alloys. The electrical conductivity, σ, for $Al_xCoCrFeNi$ can be divided into three parts according to the microstructure of the alloys. The electrical conductivity decreases with increasing x in the single-phase (FCC or BCC) regions, while it has a minimum at $x = 0.875$ in the duplex-phase (FCC + BCC) region. The electrical conductivity in the duplex-phase region is smaller than that in the single phase.

The electrical resistivity, which is the inverse of σ, is influenced by the electron–electron interaction ($T^{1/2}$), magnetic effect (T^2), and phonon (T^3) [144]. At temperatures very near absolute zero temperature, a Kondo-type term, $\ln T$, may appear in the expression of electrical resistivity for dilute magnetic atoms in nonmagnetic alloys. At intermediate temperatures, e.g., 100–200 K, T and T^2 may contribute to electrical resistivity. At temperatures higher than the Debye temperature where the thermal effect is significant, electrical resistivity is proportional to the temperature, T, and electrical resistivity may be written as

$$\rho = \rho_o + cT \tag{4-1}$$

here ρ_o is the residual electrical resistivity at 0 K.

Thermal conductivity, $\kappa(T)$, is generally obtained from measurements of thermal diffusion coefficient, $\alpha(T)$, specific heat, $C(T)$, and density, $\rho(T)$, of a material at a temperature, T, and then calculated according to the following equation [144],

$$\kappa(T) = \alpha(T) \times C(T) \times \rho(T) \tag{4-2}$$

Fig. 4.24(b) shows $\kappa(T)$ as a function of x for the $Al_xCoCrFeNi$ HEAs. At a specific T, $\kappa(x)$ decreases with x in each single-phase region for both FCC and BCC structures, and thermal conductivity for BCC

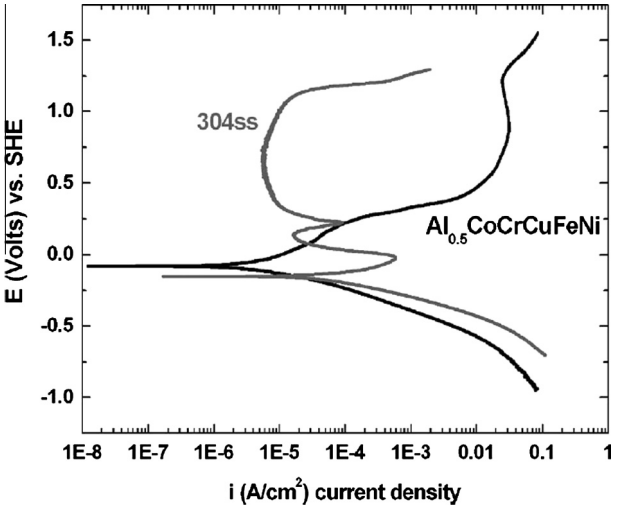

Fig. 4.25. Comparisons of the anodic polarization curves for the $Al_{0.5}CoCrCuFeNi$ alloy and the 304 stainless steel in deaerated 1 N H_2SO_4 [150].

structure is greater than that for FCC structure. Thermal conductivity in the FCC + BCC duplex region is the lowest for each specific *T*.

As shown in Fig. 4.24(c), CTE for the Al_xCoCrFeNi alloys decreases with *x*. The Curie temperature presented in Fig. 4.24(d) increases with *x* in the FCC- and BCC-single-phase regions, and reaches a minimum in the duplex FCC + BCC region. Using the invar effect to measure this second-order phase transition, one can have accurate data for the Curie temperature. The corresponding molecular field of the order of 107 Oe, shown in Fig. 4.24(d), is also estimated by assuming the magnetization of each alloy being with one Bohr magneton.

Yang et al. [145] also reported the electrical resistivity of NbTiAlVTaLa_x, CoCrFeNiCu, and CoCrFeNiAl HEAs. With the increase of La addition, the resistivities of NbTiAlVTaLa_x alloys increase. With increasing the temperature, the resistivity of the CoCrFeNiCu alloy decreases, while the CoCrFeNiAl alloy increases.

Kao et al. [146] studied the electrical, magnetic, and Hall properties of the Al_xCoCrFeNi HEAs, and found a Kondo-like behavior. Generally, the Kondo effect describes the scattering of conduction electrons in a metal due to magnetic impurities. It is a measure of how electrical resistivity changes with temperature, which is usually observed in the dilute alloy systems. The Kondo-effect likely appears in alloys containing rare-earth elements like cerium, praseodymium, and ytterbium, and actinide elements like uranium.

Lucas et al. [147] studied the magnetic properties of the FeCoCrNi HEAs, and evaluated their potential applications at high temperatures, and suggested that the inclusion of Cr, which is an anti-ferromagnetic element, will not be good for the magnetic properties, and Pd would be much better to substitute for Cr. Singh et al. [148] further studied magnetic hardening of the AlCoCrCuFeNi HEAs by a 3-dimension atom probe (3D-AP) and TEM, and indicated the decomposition of CrFeCo-rich regions into FeCo-rich and Cr-rich domains, respectively.

4.3. Biomedical, chemical and other behaviors

Braic et al. [149] investigated the biomedical properties of (TiZrNbHfTa)N and (TiZrNbHfTa)C HEA coatings. It reported that the HEA carbide coating exhibited high hardness of about 31 GPa, and good friction behavior and wear resistance when tested in simulated body fluids. Cell-viability tests proved that the osteoblast cells were adherent to the coatings, and very high percentages (>80%) of live cells were observed on the sample surface after 72 h incubation time.

Lee et al. [150] reported the corrosion resistance of the HEA of $Al_{0.5}$CoCrCuFeNi. Fig. 4.25 shows that the corrosion potential (E_{corr}) of the $Al_{0.5}$CoCrCuFeNi HEA ($-0.080\ V_{SHE}$) is apparently more noble than that of the 304 stainless steel ($-0.151\ V_{SHE}$), and the corrosion current density (i_{corr}) of the $Al_{0.5}$CoCrCuFeNi HEA (3.19 μA/cm^2) is also lower than that of the 304 stainless steel (33.18 μA/cm^2)

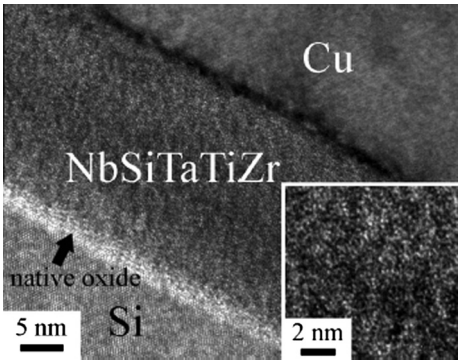

Fig. 4.26. TEM image of the Cu/NbSiTaTiZr/Si test structure after 800 °C annealing. Inset shows the high resolution image of the NbSiTaTiZr barrier [153].

by an order of magnitude in a 1 N H_2SO_4 solution. Additionally, the 304 stainless steel has a wider region of the passive potential than the $Al_{0.5}CoCrCuFeNi$ HEA. Clearly, the $Al_{0.5}CoCrCuFeNi$ alloy is more resistant to general corrosion than the 304 stainless steel (higher E_{corr}, lower i_{corr}) in the 1 N H_2SO_4 solution.

Chen et al. [99] studied the microstructure and electrochemical properties of $Cu_{0.5}NiAlCoCrFeSi$ HEAs, and made a comparison of corrosion properties between the HEAs and the type-304 stainless steel. The anodic-polarization curves of the HEAs, obtained in aqueous solutions of NaCl and H_2SO_4, clearly indicated that the general corrosion resistance of the HEAs at ambient temperature is superior to that of 304 stainless steels, irrespective of the concentration of an electrolyte in the range of 0.1–1 M. On the other hand, the HEAs' resistance to pitting corrosion in a Cl^- environment is inferior to that of 304 stainless steel, as indicated by a lower pitting potential and a narrower passive region for the HEA. Tests in 1 N sulfuric acid containing different concentrations of chloride ions showed that HEAs have the least resistance to general corrosion at a chloride-ion concentration of 0.5 M (close to the concentration in seawater). The lack of hysteresis in cyclic-polarization tests confirmed that HEAs, like the 304 stainless steel, are not susceptible to pitting corrosion in the chloride-free 1 N H_2SO_4.

Chen et al. [151,152] reported that two promising HEAs, $Al_xCrFe_{1.5}MnNi_{0.5}$ (x = 0.3 and 0.5), were designed from the AlCoCrCuFeNi alloys by substituting Mn for expensive Co and excluding Cu to avoid the Cu segregation. Microstructures and properties were investigated and compared in different states: as-cast, as-homogenized, as-rolled, and as-aged states. The $Al_{0.3}CrFe_{1.5}MnNi_{0.5}$ alloy in the as-cast, as-homogenized, and as-rolled states has a dual-phase structure of BCC and FCC phases, in which Al, Ni-rich precipitates of the B2-type BCC structure dispersed in the BCC phase. The $Al_{0.5}CrFe_{1.5}MnNi_{0.5}$ alloy in the corresponding states has a matrix of a BCC phase in which Cr-rich particles of the BCC structure and Al, Ni-rich precipitates of the B2-type BCC structure disperse. These three BCC phases have the same lattice constant. Both alloys are processable and show a hardness range of HV 300–500 in the as-cast, as-forged, as-homogenized, and as-rolled states. The $Al_{0.5}CrFe_{1.5}MnNi_{0.5}$ alloy has a higher hardness level than $Al_{0.3}CrFe_{1.5}MnNi_{0.5}$ because of its full BCC phase. Both alloys display a significant high-temperature age-hardening phenomenon; the as-cast $Al_{0.3}CrFe_{1.5}MnNi_{0.5}$ alloy can attain the highest hardness, HV 850, at 600 °C for 100 h, and $Al_{0.5}CrFe_{1.5}MnNi_{0.5}$ can possess even higher hardness, HV 890. The aging hardening resulted from the formation of a $Cr_5Fe_6Mn_8$-like phase. Prior rolling on the alloys before aging could significantly enhance the age-hardening rate and hardness level due to introduced defects. The $Al_{0.5}CrFe_{1.5}MnNi_{0.5}$ alloy exhibits the excellent oxidation resistance up to 800 °C, which is better than the $Al_{0.3}CrFe_{1.5}MnNi_{0.5}$ alloy. Combining this merit with its high softening resistance and wear resistance, as compared to commercial alloys, the $Al_{0.5}CrFe_{1.5}MnNi_{0.5}$ alloy has the potential for high-temperature structural applications.

Kao et al. [46] studied the CoFeMnTiVZr HEA system for the absorption and desorption of hydrogen. Pressure-composition-isotherms (PCIs) demonstrate that $CoFeMnTi_xVZr$, $CoFeMnTiV_yZr$, and $CoFeMnTiVZr_z$ can absorb and desorb hydrogen for x, y, and z that satisfy $0.5 < x < 2.5$, $0.4 < y < 3.0$, and $0.4 < z < 3.0$, respectively. XRD pattern reveals that $CoFeMnTi_xV_yZr_z$ alloys have a simple C14 Laves phase with a single set of lattice parameters before and after PCI tests. The distributions of each element in the $CoFeMnTi_xV_yZr_z$ alloys are roughly equal, as revealed by scanning electron microscopy (SEM)/energy-dispersive-analysis (EDS) mapping. The effects of values, x, y, and z, on the hydrogen-storage properties are elucidated in terms of the lattice constant, elemental segregation, hydride-formation enthalpies between the alloy components and hydrogen, and the averaged formation enthalpy. The high-entropy effect promotes the formation of a single C14 Laves phase, and the maximum hydrogen-storage capacity is strongly related to the hydride-formation enthalpy of the alloy and hydrogen.

Tsai et al. [153] and Chang et al. [154] studied the potential of HEAs and HEA nitrides to be used as diffusion barriers in the microelectronics industry to reduce the inter-diffusion between Cu and Si. Fig. 4.26 shows the cross-sectional TEM images of the test specimen after annealing at 800 °C. Three distinct layers with sharp interfaces can be observed. This trend means that the barrier is effective, and there is no inter-diffusion. Note that the single-crystal lattice image of the Si substrate remains intact, and no silicidation reaction is observed. Therefore, the NbSiTaTiZr HEA indeed remains its chemical stability against Si up to 800 °C. Additionally, from the inset of Fig. 4.26, which shows the high-resolution TEM image of the barrier, we can see that the NbSiTaTiZr HEA retains its amorphous nature after annealing at 800 °C. We note that virtually all known conventional amorphous metals, even

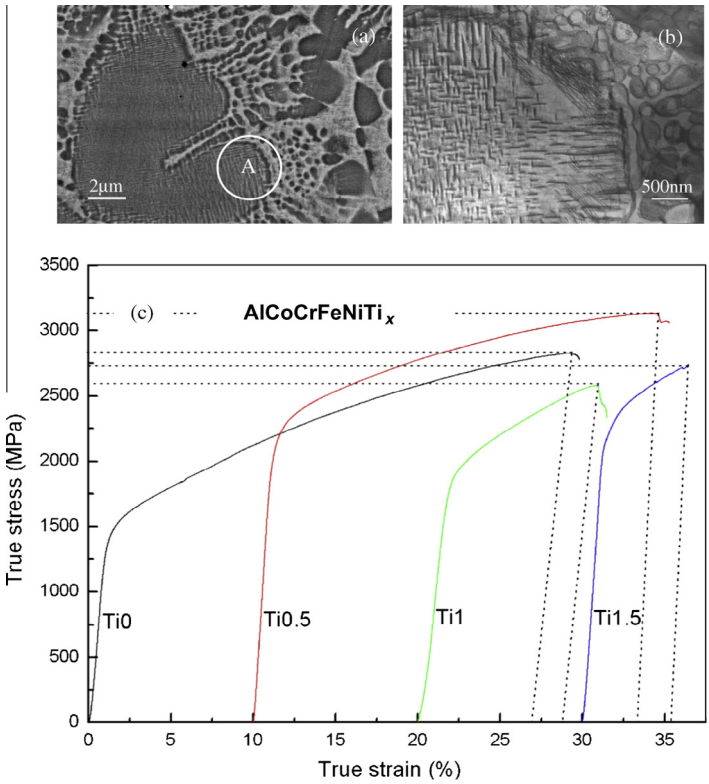

Fig. 5.1. SEM back-scattered micrograph (a), and TEM bright-field image (b) which is corresponding to the A region marked by circle in (a). Compressive true stress–strain curves of Ti0, Ti0.5, Ti1, and Ti1.5 alloy rods with diameter of 5 mm at a strain rate of 10^{-4} s^{-1} (c) [136].

those with high GFA, crystallize below 550 °C. Therefore, the extremely high structural stability of the NbSiTaTiZr barrier is unique and striking [153].

5. Serrations and deformation mechanisms

According to Sethna, Dahmen et al. [155–160], crackling noise arises when a system responds to slowly changing external conditions through discrete, impulsive events spanning a broad range of sizes. For example, when a magnetic tape is slowly magnetized by an external magnetic field, the process happens in avalanches, "Barkhausen noise" of reorienting magnetic domains that range from the microscopic to macroscopic scale in size. The avalanche size and duration distributions are often described by universal power laws over a broad range of sizes and durations. Here "universal" means that the scaling behavior on long length scales is independent of microscopic details and only dependent on generic properties, such as symmetries, dimensions, interaction range, and dynamics. In many systems, this universality has been explained theoretically as being due to the proximity to an underlying critical point.

While Barkhausen noise is related to the creation of magnetic domains and domain wall motion during the process of magnetization, similar crackling noise can also be observed in slowly sheared micro- and nano-crystals [161–178], slowly-sheared granular materials [179–184], as well as in metallic alloys, including BMGs [185,186] and HEAs [187].

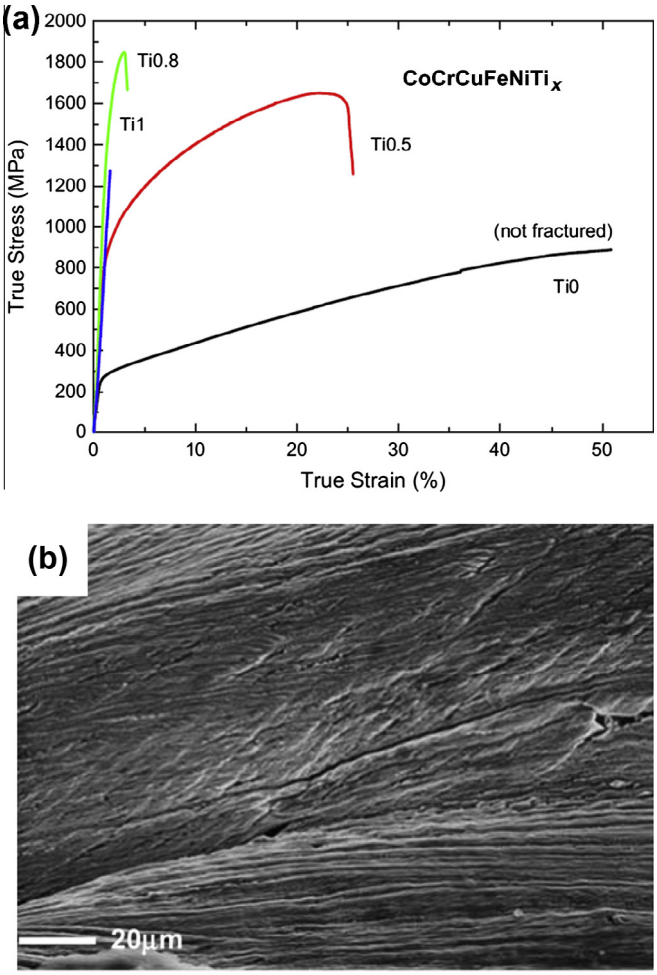

Fig. 5.2. (a) True stress–true strain curves of the CoCrCuFeNiTi$_x$ rod samples with diameter of 5 mm (x = 0, 0.5, 0.8, and 1) at a strain rate of 10^{-4} s^{-1}. (b) SEM secondary electron images of fracture surfaces of the CoCrCuFeNi alloys [13].

In each of the above cases, crackling noise corresponds to serrations or "steps" in the magnetization hysteresis loops or the stress–strain curves, respectively. Similar crackling noise has also been observed in martensitic materials [188]. With modeling and analysis of these serrations, we may provide in-depth mechanisms for plastic deformation, fracture, and magnetization of the materials.

5.1. Serrations for HEAs

Serrations can be defined as a saw-like appearance, a row of sharp or tooth-like projections. Monolithic BMGs present serrations during plastic deformation, especially at a normal strain rate around 10^{-4} s^{-1}. The serrations are closely related to the shear-band formation and propagations [189–192], while for HEAs, serrations were exhibited at a medium strain rate of 10^{-3} s^{-1} or at low temperatures.

The microstructure and the stress–strain curves of the AlCoCrFeNiTi$_x$ HEAs at a strain rate of 10^{-4} s^{-1} are presented in Fig. 5.1. The HEAs are mainly of BCC-structured alloys. The dendrite is

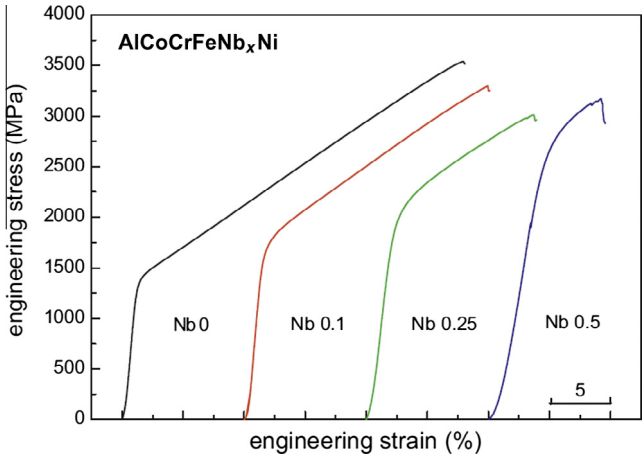

Fig. 5.3. The compressive stress–strain curves of the AlCoCrFeNb$_x$Ni rod samples with a diameter of 5 mm at a strain rate of 10^{-4} s^{-1} (x = 0, 0.1, 0.25, and 0.5) [135].

marked by A, and the interdendrite phase is in gray color, as shown in Fig. 5.1(a). In region A, it shows needle-like precipitations and dislocation loops. However, the clear serrations on the stress–strain curves were not found [136]. Fig. 5.2 exhibits the stress–strain curves for the CoCrCufeNiTi$_x$ HEAs at the same strain rate, and these HEAs mainly have a FCC structure. In Fig. 5.2, the strength increases with the increase of Ti content. However, the serrations during the plastic deformation of the Ti free alloy were not observed, even the plasticity is very large. Fig. 5.2(b) presents the deformation band for the Ti-free alloy after the compression test, which clearly show the flow and river-like patterns [13].

Fig. 5.3 presents the stress–strain curves of the AlCoCrFeNb$_x$Ni alloys with a diameter of 5 mm at a strain rate of 10^{-4} s^{-1} (x = 0, 0.1, 0.25, and 0.5) [135]. In this Figure, the serrations are absent. The microstructures of the alloys have a BCC to BCC + Laves phase with the increase of Nb contents. Fig. 5.4(a) shows XRD patterns for the AlCoCrFeNi alloys with different diameters, while Fig. 5.4(b) presents compressive true stress–strain curves for these HEA samples at a strain rate of 10^{-4} s^{-1}. From the XRD patterns, the sample size did not alter the BCC phase, while the plasticity decreases with the increase of sample size. However, no clear serrations were observed for all the samples with different sizes [129].

The low-temperature (77 K) compressive stress–strain curves for the BCC-structured AlCoCrFeNi HEA at a strain rate of 10^{-4} s^{-1} are presented in Fig. 5.5. One or two large serrations and some smaller serrations during the plastic deformation were found [137]. Fig. 5.6 presents the stress–strain curves of the $Al_{0.5}CrCuFeNi_2$, Al1CrCuFeNi$_2$, and $Al_2CrCuFeNi_2$ alloys at a strain rate of 10^{-4} s^{-1}. Serrations on the stress–strain curves were not found [5].

The compressive stress–strain curves of the $Al_{0.5}CoCrCuFeNi$, $Al_{1.0}CoCrCuFeNi$, and $Al_{2.0}CoCrCuFeNi$ alloys under different testing temperatures at different strain rates of (a) 10 s^{-1} and (b) 10^{-3} s^{-1} are presented in Fig. 5.7 [130]. It is clear that the serrations on the stress–strain curves at the strain rate of 10^{-3} s^{-1} are greater than that at the strain rate of 10 s^{-1}. It seems that the serration is greater at the lower testing temperatures. Moreover, serrations seem to depend on composition of the alloys.

The compressive stress–strain curves of the $Ta_{20}Nb_{20}Hf_{20}Zr_{20}Ti_{20}$, $Ta_{20}Nb_{20}W_{20}Mo_{20}V_{20}$ and $Ta_{25}Nb_{25}W_{25}Mo_{25}$ alloys at a strain rate of 10^{-3} s^{-1} are shown in Fig. 5.8 [126]. Some serrations on the plastics deformation region for the $Ta_{20}Nb_{20}Hf_{20}Zr_{20}Ti_{20}$ alloy were observed. In summary for the serration behavior of HEAs, the serrations during the compression tests at the strain rate of 10^{-3} s^{-1} seem to be greater than those at the strain rate of 10^{-4} s^{-1} or 10 s^{-1}. At lower temperatures, the serrations are more visible than that at higher temperatures. More work needs to be done on this field.

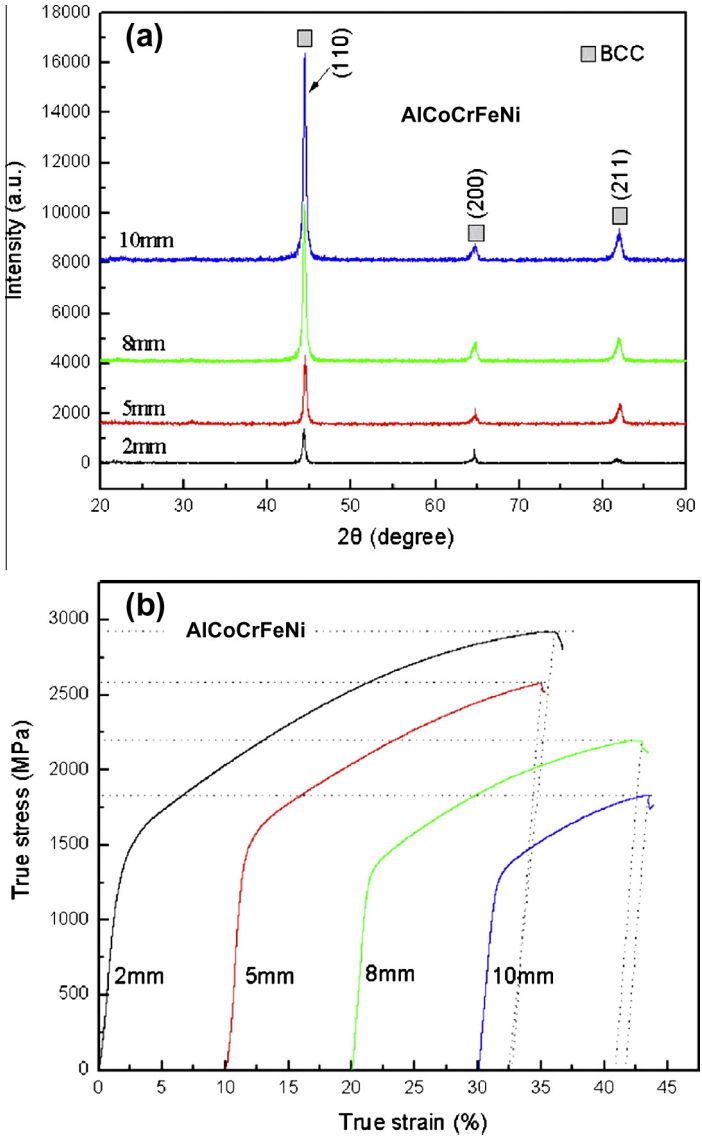

Fig. 5.4. (a) The XRD patterns for AlCoCrFeNi alloy samples with different diameters; (b) compressive true stress–true strain curves for the AlCoCrFeNi alloy samples with different diameters at a strain rate of $10^{-4}\,s^{-1}$ [129].

5.2. Barkhausen noise for HEAs

Fig. 5.9 presents the serrations on the magnetization loops, which correspond to the Barkhausen noise [193]. Fig. 5.10 shows the magnetization curves of the $AlCoCrFeNb_xNi$ alloys ($x = 0$, 0.1, 0.25, 0.5, and 0.75) [135]. According to the following equation of the classification of magnetic properties:

$$\chi = \frac{M\ (\mathrm{A/m})}{H(\mathrm{A/m})} = \frac{\sigma\ (\mathrm{emu/g}) \cdot \rho\ (\mathrm{g/cm^3})}{4\pi \cdot H(\mathrm{Oe})} \tag{5-1}$$

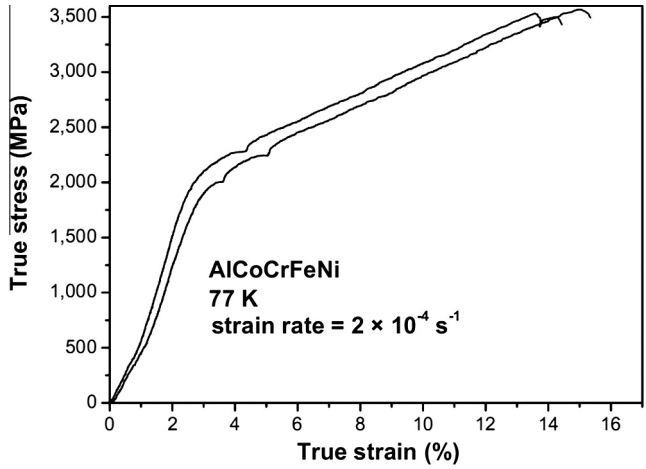

Fig. 5.5. The compressive true stress–strain curves of the AlCoCrFeNi HEA at 77 K at a strain rate of 10^{-4} s^{-1} [137].

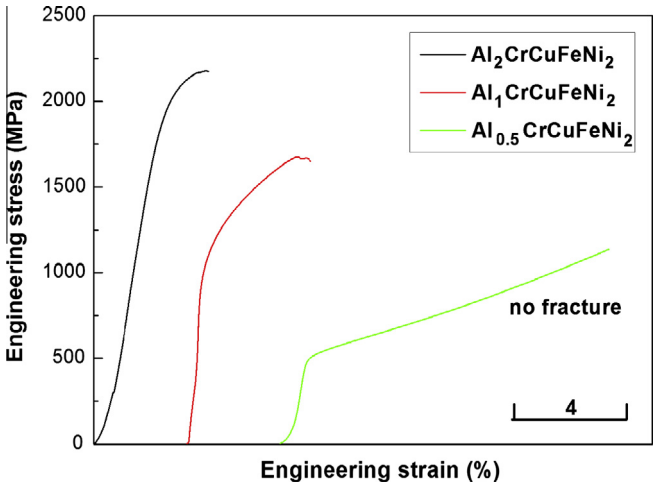

Fig. 5.6. Stress–strain curves of $Al_{0.5}CrCuFeNi_2$, $Al_1CrCuFeNi_2$, and $Al_2CrCuFeNi_2$ alloys at a strain rate of 10^{-4} s^{-1} [5].

where χ is the permeability, M is the magnetization, H is the magnetic field intensity, σ is the specific saturation magnetization, and ρ is the density of alloys equal to roughly 6.5–7.5 g/cm^3 for the alloy series. According to Eq. (5-1), χ can be estimated to be 2.0×10^{-2}–3.0×10^{-3}. According to the definition of ferromagnetism, it can be seen that this alloy exhibits a ferromagnetic property, which may be ascribed to the additions of the paramagnetic elements (Al and Nb) and the anti-ferromagnetic element (Cr) into these alloys, in addition to the ferromagnetic elements (Fe, Co, and Ni) that do not preserve the ferromagnetic property. The coercivity, H_c, ranges from 52 to 94 Oe, which reveals its soft magnetic behavior; the saturation magnetization, M_s, and remanence, M_r, approximately decrease, while H_c increases with increasing the Nb content, which may be attributed to two reasons: Firstly, the CoCrNb alloy belongs to hard magnetic materials, and H_c can reach 105 A/m. Secondly, the Laves phase may pin the magnetic domain of the BCC phase matrix, as they are rotating under an external magnetic field.

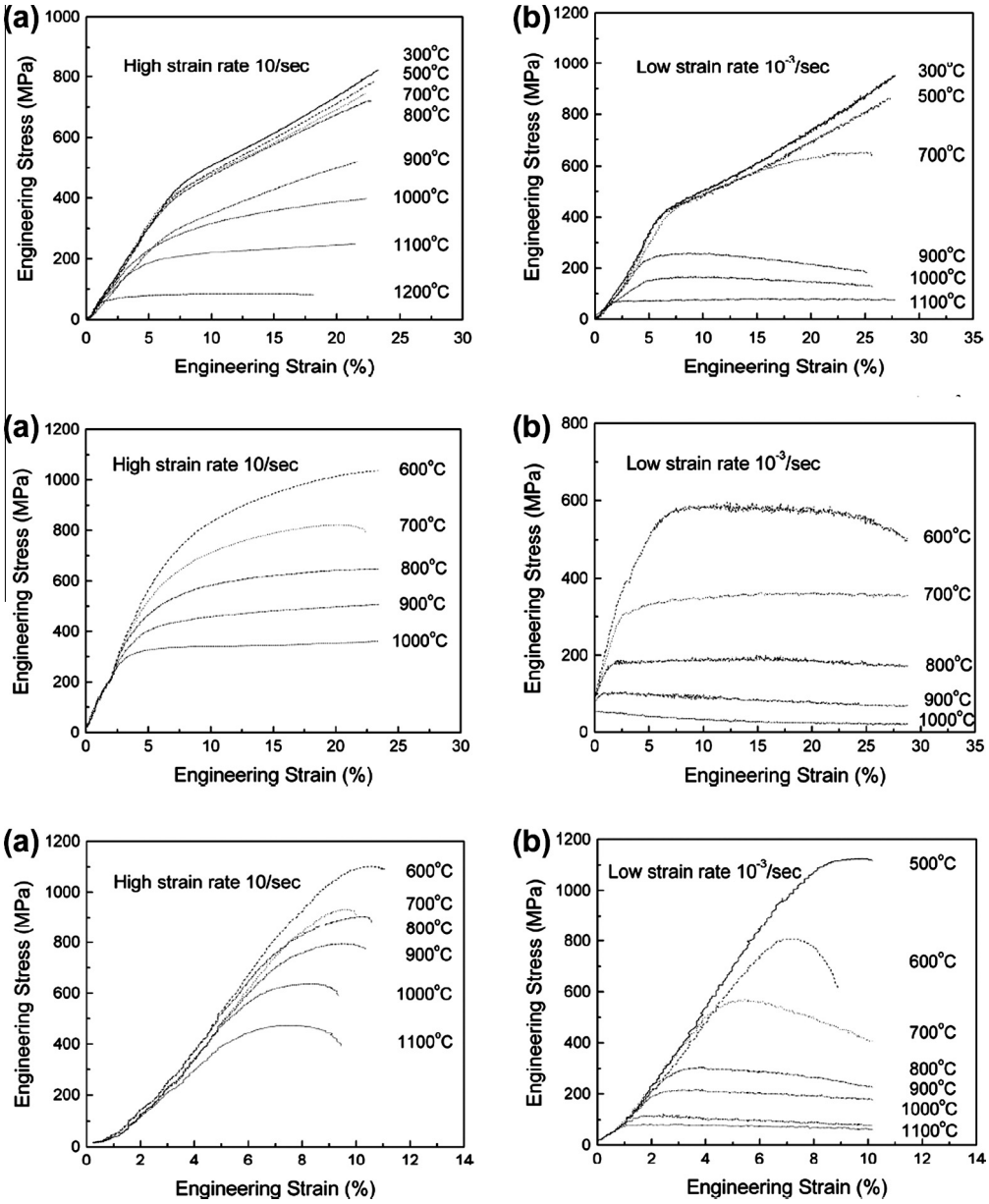

Fig. 5.7. Compressive stress–strain curves of $Al_{0.5}CoCrCuFeNi$ alloys under different testing temperatures at different strain rates of (a) $10\,s^{-1}$ and (b) $10^{-3}\,s^{-1}$. Compressive stress–strain curves of $Al_{1.0}CoCrCuFeNi$ alloys under different testing temperatures at the different strain rates of (a) $10\,s^{-1}$ and (b) $10^{-3}\,s^{-1}$. Compressive stress–strain curves of $Al_{2.0}CoCrCuFeNi$ alloys under different testing temperatures at the different strain rates of (a) $10\,s^{-1}$ and (b) $10^{-3}\,s^{-1}$ [130].

The magnetization curves of the $Ti_xCoCrCuFeNi$ alloys ($x = 0$, 0.5, 0.8, and 1), showing a transition from the paramagnetism ($x = 0$ and 0.5) to super-paramagnetism ($x = 0.8$ and 1), are presented in Fig. 5.11 [13]. There are some serrations on the magnetization hysteresis loops.

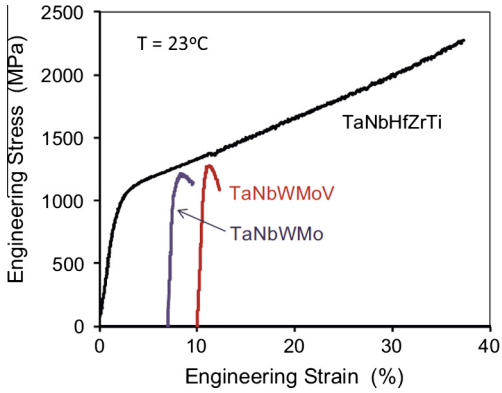

Fig. 5.8. Engineering stress vs. engineering strain compression curves of the $Ta_{20}Nb_{20}Hf_{20}Zr_{20}Ti_{20}$ alloy and $Ta_{20}Nb_{20}W_{20}Mo_{20}V_{20}$ and $Ta_{25}Nb_{25}W_{25}Mo_{25}$ alloys at a strain rate of $10^{-3}\ s^{-1}$ [126].

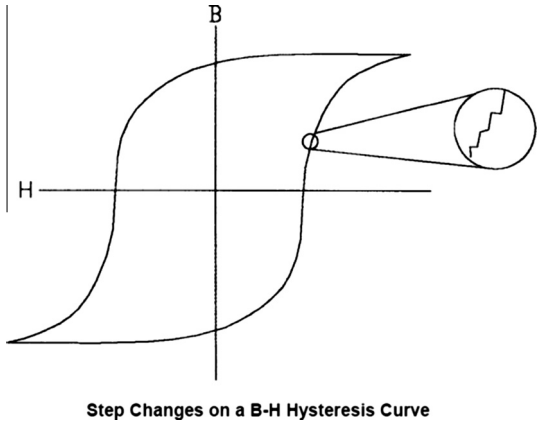

Fig. 5.9. Barkhausen noise corresponding to the serrations on the magnetization loops [193].

5.3. Modeling the Serrations of HEAs

A number of different models have been developed to study the statistics of crackling noise, many of which are reviewed in [155]. Originally Barkhausen noise in magnetic materials was used as a paradigm for crackling noise. Random field Ising models far from equilibrium were shown to reproduce the magnetization avalanche statistics observed in Barkhausen-noise experiments [155].

More recently the crackling noise during plastic deformation is being modeled. Simulations of slowly-sheared crystals using discrete dislocation-dynamics models [162,194–200], continuum models [194], phase-field models [201], and phase field crystal models [202] all reveal a broad (power-law) distributions of the serration sizes in the associated stress–strain curves.

Interestingly, the slip avalanche statistics observed in many of these simulations are predicted by a simple analytic mean field theory (MFT) model [156,179]. It is described in detail in Refs. [156,179]. It predicts the serration-size statistics, such as size distributions, duration distributions, power spectra of acoustic emissions, and other properties, for plastic material deformation. It is important to note that different materials with roughly the same stress strain curves may reveal different serration statistics or different statistics of the acoustic emission under deformation, resulting from different underlying deformation mechanisms. This means that the analysis of serration statistics is a powerful

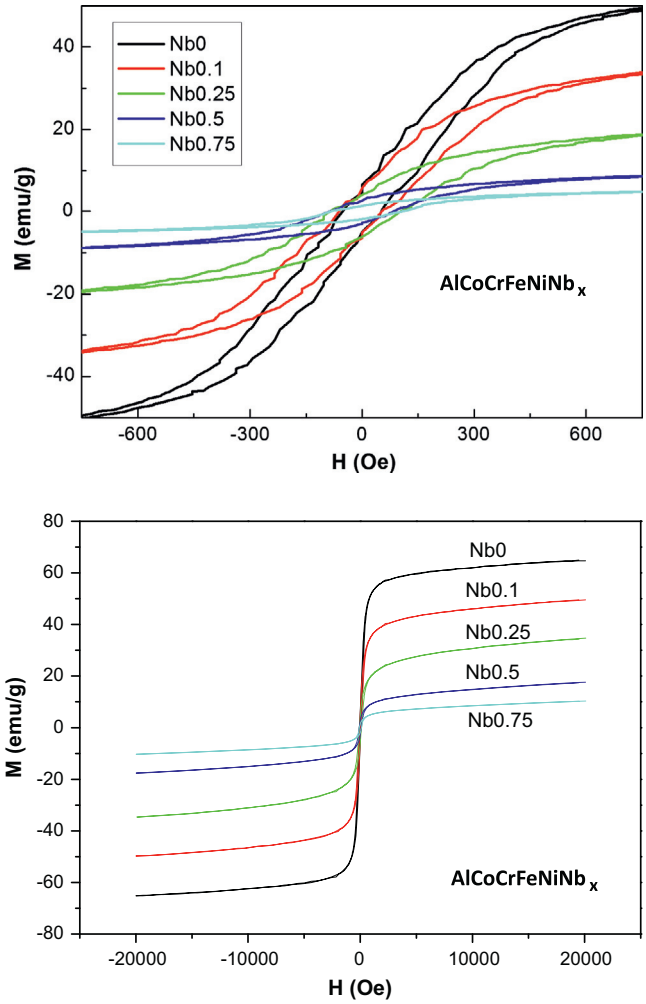

Fig. 5.10. Magnetization curves of the $AlCoCrFeNb_xNi$ alloys (x = 0, 0.1, 0.25, 0.5, and 0.75) [135].

tool for testing models of the underlying deformation mechanism. The serration statistics far from the failure stress also provide information about the distance to failure, so that the analysis of serrations is useful for nondestructive materials testing.

The simple analytic model makes the following assumptions [156]:

1. A slowly-sheared material has weak spots where slip initiates when the local stress exceeds a random local threshold stress. (In crystals, for example, weak spots could be the locations of movable dislocations.)
2. Slip avalanches (i.e. collective slips of many coupled weak spots) can become macroscopically large, spanning length scales that are large, compared to the microscopic structure of the material.
3. The material is sheared sufficiently slowly so that slip-avalanches do not overlap in time, i.e. each slip avalanche has enough time to finish before the stress is slowly increased to trigger the next slip avalanche.

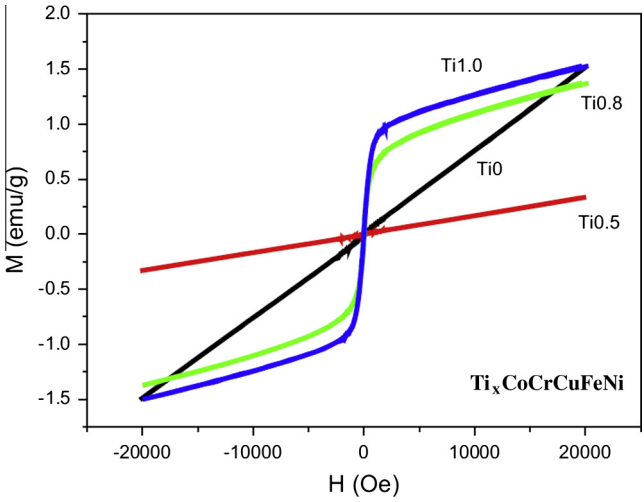

Fig. 5.11. Magnetization curves of the $Ti_xCoCrCuFeNi$ alloys ($x = 0$, 0.5, 0.8, and 1), showing a transition from the paramagnetism ($x = 0$ and 0.5) to superparamagnetism ($x = 0.8$ and 1) [13].

4. The mean field approximation replaces the long-range elastic interactions with infinite range interactions. This means that in mean field theory the long range elastic interactions (for example between dislocations) are replaced by interactions that do not decay with distance. In this approximation each weak spot or dislocation interacts with every weak spot in the material equally strongly, irrespective of their relative distance. This sounds like a drastic approximation, however by use of tools from statistical physics and the theory of phase transitions, it can be shown not to affect the scaling behavior of the serration statistics on long length scales [156]. In other words if the serration size distribution decays with a certain power law in the presence of long range elastic interaction, it decays with the same power law in the simple models that are based on the mean field approximation.

A failed spot slips until the local stress is reduced to a random arrest stress, and then re-sticks. The stress released by a failed spot triggers other elastically-coupled weak spots to slip, creating a slip-avalanche. According to assumption 3, avalanches have sufficient time to complete, before the slow, externally imposed material deformation increases the stress to trigger the next slip avalanche. This is called the "adiabatic limit" characterized by a separation of time scales between the fast avalanche propagation dynamics and the slowly-increasing external shear stress or the small applied strain rate. In Refs. [156,179], detail-independent ("universal") analytical predictions are extracted for this adiabatic limit, which agree with numerical studies of dislocation dynamics [161,197,199,200].

The simple model predicts the serration statistics for two different boundary conditions: slowly increasing stress boundary conditions and small imposed strain-rate boundary conditions.

Exact results for a slowly-increasing applied shear stress (F) boundary conditions: In Ref. [156], both a continuum and a discrete version of the model are discussed. Both versions of the model give the same results for the serration statistics. We briefly review the discrete version here, since it is easier to analyze analytically and numerically.

In the discrete version of the MFT model with N lattice points, at applied stress F, the local stress τ_l at a lattice point l can be given [203]:

$$\tau_l = J/N\sum_m (u_m - u_l) + F \tag{5-2}$$

Each point fails when the local stress, τ_l, is larger than the local failure threshold (slip stress) $\tau_{f,l} \equiv \tau_{s,l}$ (or $\tau_{d,l}$). When site l fails, it slips by a certain amount, Δu_l, resulting in a stress reduction, $\tau_{f,l} - \tau_{a,l} \sim 2G\Delta u_l$, where $G \sim J$ is the elastic shear modulus. The released stress is equally redistributed to the other points in the system, possibly triggering some of the other points to slip, leading to a slip avalanche, visible as a serration in the stress–strain curve. In Ref. [156], the distribution of slip avalanche sizes is calculated analytically. For a slowly increasing F ($F < F_c$, where F_c is a flow stress or failure stress for a ductile material), the solid responds with slip avalanches (strain steps, or serrations in the stress–strain curve) of sizes. These slip avalanches typically also cause acoustic emissions that can be measured. For a small stress-bin around the flow stress, F_c, the distribution, $D(s,F_c)$, of serration sizes follows a universal power law:

$$D(s,F_c) \sim 1/s^{\tau} \tag{5-3}$$

with a universal critical exponent $\tau = 1.5$. For small stress-bins around stresses F below but close to F_c, the distribution follows the same power law up to a maximum size:

$$S_{\max} \sim (F_c - F)^{1/\sigma} \tag{5-4}$$

with a universal exponent $\sigma = 0.5$. In other words, the maximum size of the serrations seen in a small stress-bin centered around a stress F below the flow stress F_c, is related to the square root of the inverse distance of F from the flow stress. This is reflected by the scaling form that the model predicts for large serration sizes:

$$D(s,F) \sim 1/s^{\tau} D(s \cdot (F_c - F)^{1/\sigma}) \tag{5-5}$$

with universal cutoff scaling function $D(x) \sim A\exp(-Bx)$. The constants A and B depend on the details of the material. These scaling predictions can most easily be tested using Widom scaling collapses, as done, for example, for slip avalanches in nanocrystals in Ref. [178], and for Barkhausen noise in magnetic systems in Ref. [155]. In a Widom scaling collapse one plots $y = D(s,F)s^{\tau}$ vs. $x = s \cdot (F_c - F)^{1/\sigma}$ and tunes the values for τ, σ, and F_c until the distributions $D(s,F)$ collapse unto the same curve. The model predicts that the values for τ and σ for which a collapse is achieved are the mean field values $\tau = 1.5$ and $\sigma = 0.5$, and the collapse of the curves is predicted to fit the above exponential scaling function $D(x)$.The local slope of the stress–strain curve (the effective shear modulus G_e), is inversely proportional to the mean avalanche size, $\langle s \rangle$, i.e., it scales as [156]:

$$G_e \sim 1/\langle s \rangle \sim (F_c - F)^{(2-\tau)/\sigma} \sim (F_c - F) \tag{5-6}$$

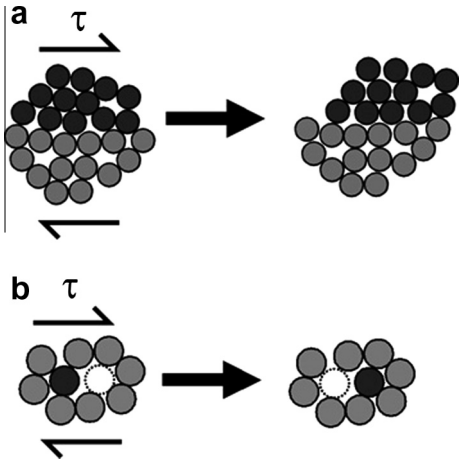

Fig. 5.12. Two-dimensional schematics of the atomistic deformation mechanisms proposed for amorphous metals, including (a) a shear transformation zone (STZ), after Argon, and (b) a local atomic jump, after Spaepen [68].

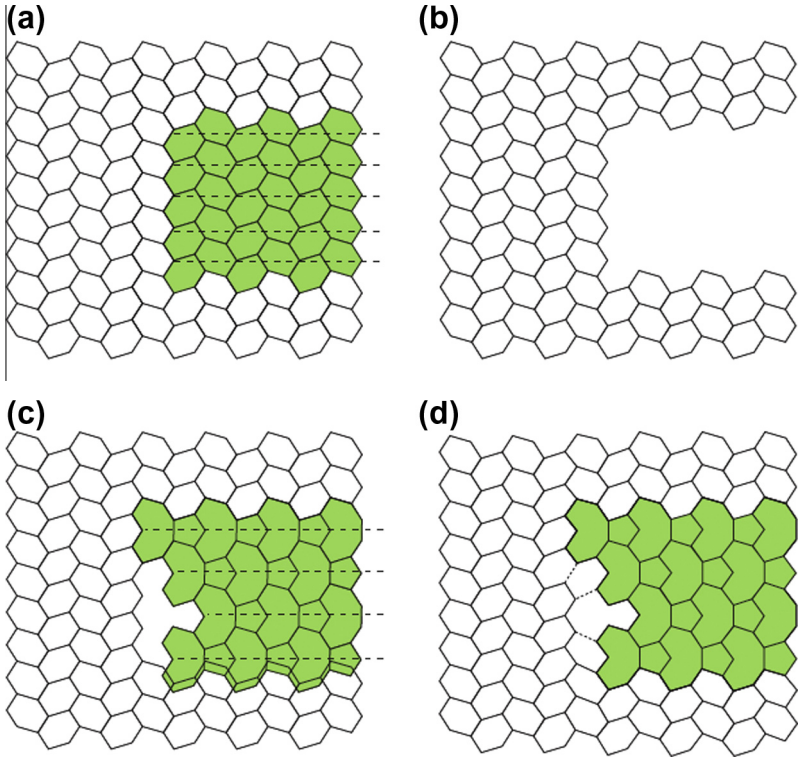

Fig. 5.13. Metadislocations. (a and b) Similar to regular dislocations, a slab of matter (shown in green) is withdrawn from the crystal to form a metadislocation. (c) This slab is replaced by another piece of crystal that is structurally related to the previous one. (d) After relaxation of the lattice, a loop surrounding the core of the defect allows us to define a Burger's vector. The length of a unit edge, typically 1 nm, is much larger than the distance between two neighbour atoms. Deformation is carried by local, short-distance atomic jumps, which propagate the foreign structure into the other and carry the crystal strain. The dashed lines in c emphasize the four slabs of material inserted in place of the five slabs removed in a [204].

These are some of the main predictions for the serration statistics of ductile materials. This theory has been found to agree extremely well with dislocation slip avalanche statistics for slowly compressed nanopillars [178]. In the supplementary material of [178] a detailed description of the data analysis procedure is given. In experiments that do not yield enough slips to produce statistically meaningful slip size distributions for the serrations that are observed within small stress bins, it may be easier to analyze histograms of slip sizes that are integrated over the entire stress range. Integrating the distribution $D(s,F)$ of Eq. (5-5) over stress F yields a prediction for a stress-integrated distribution of slip sizes $D_{\text{int}}(s)$ that is expected to scale as

$$D_{\text{int}}(s) \sim \int_0^{Fc} D(s,F)dF \sim \frac{1}{s^{\tau+\sigma}} \sim 1/s^2 \tag{5-7}$$

In the last step of Eq. (5-7) that we have used, that mean field theory predicts that $\tau + \sigma = 2$. The scaling behavior predicted by Eq. (5-7) has also been observed for slip avalanches of slowly compressed nanopillars [178]. Another useful method to improve the statistics for experiments with small numbers of slips is to use complementary cumulative distributions, rather than probability density distributions, as discussed in detail in [178] and its supplementary material. (The complementary cumulative distribution $C(s)$ is given by the fraction of slips that are *larger* than size s, while the probability density distributions, such as $D_{\text{int}}(s)$, is given the fraction of slips within a small bin of sizes around the mean value s.)

In Ref. [156], a weakening parameter ε is introduced that can be used to also model serration statistics for brittle materials, before the main failure event.

Related results can be derived for the boundary condition of a small imposed strain rate Γ: For this case, for ductile materials, the MFT predicts power law statistics as Eq. (5-7), with again $\tau = 1.5$ and $\lambda = 1$ in MFT.

$$D(s, \Gamma) \sim 1/s^{\tau} K(s \cdot \Gamma^{\lambda}) \tag{5-8}$$

Here K is a quickly decaying cutoff scaling function, so that the maximum serration in the power law regime of the distribution is expected to grow as as $s_{\max} \sim \Gamma^{(-\lambda)}$ as the strain rate is reduced to zero,

Additional predictions for serration duration distributions, power spectra of acoustic emissions caused by stress serrations, and other properties are derived in Ref. [156]. Comparisons of these predictions with experiments on HEAs are an open question for future studies, which can significantly advance our understanding of these new materials, including HEAs and BMGs.

5.4. Deformation mechanisms for HEAs

It is well known that the deformation mechanism for the conventional alloys is mainly dictated by the slip of dislocations. Another typical mechanism of plastic deformation is by twinning in conventional alloys. While for the amorphous alloys, it is hard to define dislocations and twinning. A model of shear-transition-zone (STZ) was proposed by Argon and a model of free volumes by Spaepen, as shown in Fig. 5.12 [68]. For quasi-crystals, a metal dislocation model can be used, as shown in Fig. 5.13 [204].

The plastic deformations for alloys can be roughly categorized into two types. Type-I is associated with the dislocation slips and/or climbs. This kind of deformation is usually smooth and has small serrations in the stress–strain curves. While for type-II, it is related to deformation twinning, STZ, and meta-dislocations. The type-II plastic deformation usually needs to activate more atoms, which may induce a larger scale of serrations than type-I.

In some cases, the type-I plastic deformation can also lead to serrations, which is generally induced by the interactions between the solute atoms with the dislocations. This phenomenon is also called the jerky flow, or Portevin-Le-Chatelier (PLC) effect [205]. Its mechanism is usually ascribed to dynamic-strain aging: when dislocations are arrested at obstacles during the waiting time necessary for the thermal activation of their motion, diffusing solute atoms lead to their additional pinning, followed by abrupt break-away. The serrations for the crystalline alloys have been reported in the alloys of AlMg alloy [205], α-brass [206], NiCoCr-base supper-alloys [207], and Inconel 718SPE alloy [208]. The interactions between the solute atoms and the dislocations tend to make the deformation units in the crystalline alloys complex, and tend to be like a type-II deformation.

Twinning can be categorized to one of the type-II plastic deformation mechanisms in the metallic alloys. It is reported that the plastics deformation by twinning rather than by dislocation movements showing much clearer serrations on the stress–strain curves. The twinning-induced plasticity (TWIP) steels show the serrations [209], while if alloyed with Al, their stacking fault energy reduced, then the plastic deformation is carried by the movement of dislocations rather twinning, leading no serrations on the stress–strain curves.

The STZs in the amorphous alloys are not structural defects, while the lattice dislocations are crystal defects. The shapes of serrations in the amorphous metals usually have sharp bottoms and tops [210]. In contrast, the serrations in crystalline alloys show a sharp top with a plateau bottom (type-A serration) or a plateau top with a sharp bottom (type-C serrations) [208]. According to Lebyodkin et al. [205], type-A serrations are induced by the interstitial solute atoms, and type-B serrations are induced by the substitutional atoms interacting with dislocations.

It is well known that when alloys are deformed in their plastic range, an essentially smooth and continuously varying deformation pattern gives way to highly localized deformation in the form of shear bands [211]. Sometimes such bands, once formed, persist and the subsequent deformation proceeds in a markedly non-uniform manner. However, such intense local deformation leads directly to ductile fracture, so that the onset of localization is synonymous with the inception of rupture.

Even though, the dislocation gliding is the most common mechanism of plastic deformation, there are still many factors which will make dislocations not able to glide. The HEAs are composed of many kinds of elements with equi-molar and high chemical disordering. The plastic-deformation mechanism is believed to be just located in between the conventional alloys and the amorphous metals.

6. Glass formation in high-entropy alloys

High-entropy bulk metallic glasses (BMGs) can be referred to BMGs with an equal-atomic or near equal atomic composition. These BMGs have not only large high glass-forming ability (GFA), but also very high entropy of mixing. Consequently, the high-entropy BMGs are a special class of BMGs which have both strong topological disorder and chemical disorder.

Recently, Lucas et al. have verified that HEAs indeed lack the long-range chemical order [40]. In this regard, the high-entropy BMGs may have special properties which do not exhibit in either normal BMGs or HEAs.

6.1. High-entropy effects on glass formation

Since the discovery of metallic glasses by direct quenching the melts in 1960 [212], what kind of compositions would have large GFA is always an open question. There are at least three viewpoints:

6.1.1. The best glass former is located at the eutectic compositions

It has been reported that for the binary and ternary alloys, the best GFA is usually found at or near the eutectic compositions [213–222]. This trend can be explained by the fact that the smallest temperature gap at the eutectic composition is required for undercooling below the glass-transition temperature, T_g, from the liquid temperature, T_l. Moreover, the reduced glass transition temperature, T_{rg} (defined as: $T_{rg} = T_g/T_l$) [214], would reach the maximum at the eutectic composition. This is because the T_l is the lowest at the eutectic composition, while the T_g is usually less dependent on the compositions. However, recent results revealed that this viewpoint might be not true in a irregular eutectic system in which the best glass formers are usually off-eutectic with an reduced T_{rg} value [223].

Another interesting argument along this line is proposed by Boettinger [224] who proposed that based on glass formation, there also exist at least two types of eutectic alloys. One type is with shallow liquidus lines and T_o curves are with low slopes (here T_o curves were defined as the polymorphic transition from the liquid to the solid with the same Gibbs free energy and without composition partitions). The T_o lines intersect at a temperature above the lowest glass transition temperature of the alloy system. This type of alloys tends to form solid solutions even when the growth velocity is very high, as shown in Fig. 6.1(a). The other type is well known as the deep eutectic, and T_o curves are very steep. The T_o lines normally intersect at a temperature below the lowest glass transition temperature of the entire alloy system, and glasses would be formed when the growth velocity is high enough, as shown in Fig. 6.1(b).

6.1.2. The best glass former is the composition with dense atomic packing

It has also been proposed that easy glass formation can occur due to the jamming effect of the complete filling of holes in the densely random-packed structure with small and large metallic atoms [225,226]. The dense packing would make the alloy melt with high viscosity and low atomic mobility, which greatly reduce the nucleation rate and growth velocity, and thus facilitate glass formation.

6.1.3. The best glass former has high entropy of mixing

A single pure element metal, hardly form glass by rapid quenching from the melts, and the binary metallic alloys which form glasses usually with a limited thickness by rapid cooling, usually at above 10^6 K s^{-1}. Ternary, quaternary, or alloys with more constituent elements can form glasses in bulk forms at a slow cooling rate. Particularly, the GFA of certain multi-component alloys is close to that of the oxide glass; the critical cooling rate for the VIT-1 alloy is only 0.1 K s^{-1}, and the critical size for glass formation reaches over 70 mm in diameter [227].

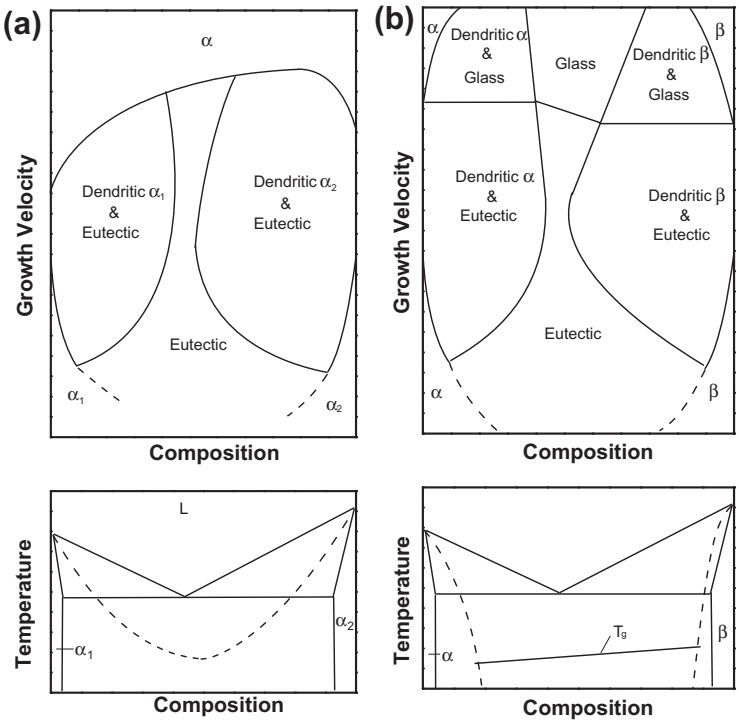

Fig. 6.1. Two types of eutectic alloys. (a) Forming the solid solutions and (b) forming glasses [224].

It is apparent that the three viewpoints proposed above for the composition requirements of easy glass-forming materials are not the same. Fig. 6.2 shows the compositions of the eutectic, dense atomic packing, and equi-atomic ratio alloys in a ternary system. Glass formation virtually is the outcome of phase competition during solidification. The alloys in which crystallization is suppressed to a maximum extent, i.e., formation of crystalline phases is the most difficult, should have the largest GFA in the alloy system. Therefore, high-entropy effects on glass formation, which varies from system to system, should be carefully analyzed.

6.2. GFA for HEAs

Greer [29] proposed the "confusion" principle by summarizing the reported easy glass formers which usually contains multiple elements, and concluded that the more elements involved, the lower the chance that the alloy can select the viable crystal structures, thus leading to larger GFA. Based on this principle, the high entropy of mixing is beneficial for glass formation.

On the other hand, viscosity, η, is extensively used to describe glass formation in the metallic-glass community via the Adams–Gibbs equation [228]

$$\eta = \eta_0 \cdot \exp\frac{C}{TS_c(T)} \tag{6-1}$$

where η_0 is the ideal viscosity, C is activation energy barrier to cooperative arrangements, T is temperature, and S_c is the configurational entropy. The main contribution to S_c is the entropy of mixing. From Eq. (6-1), it is known that high entropy usually corresponds to low viscosity, which normally results in low GFA from a kinetic point of view.

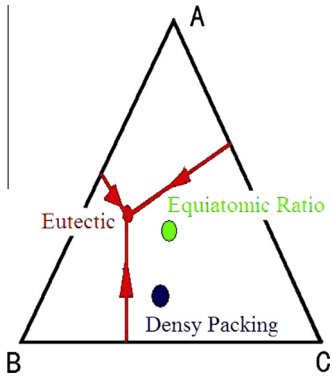

Fig. 6.2. The proposed easy glass-forming compositions, I: eutectic; II: equiatomic ratio and high-entropy composition; III: dense atomic packing composition.

Therefore, simple mixing of many elements in the periodic table might not favor glass formation. In contrast, other factors must be taken into account as far as high-entropy effects are considered.

Based on literature data, glass-forming ability can indeed be greatly improved by proper addition of more elements. Zhang et al. [229,230] have proposed that the elements in alloys can be categorized into two types. The type-I elements are the unlike constituent elements, and it is generally recognized that these elements in the alloys with high GFA usually have a large difference in their atomic size and heat of mixing. The type-II elements are the similar ones which are close to each other in the periodic table. The type-I elements can improve the GFA by increasing atomic packing efficiency and the viscosity of the alloys, as extensively studied by many research groups. For example, the smallest metallic element, Be, can greatly improve the GFA of Zr and Ti-based alloys. The rare earth metals, such as Y, with a large atomic size can also dramatically increase the GFA of Zr, Ti, and Fe-based alloys. The similar elements can also significantly improve the GFA of the metallic alloys, which is mainly associated with the high-entropy effects. An example is that the binary LaCu alloy only has limited GFA

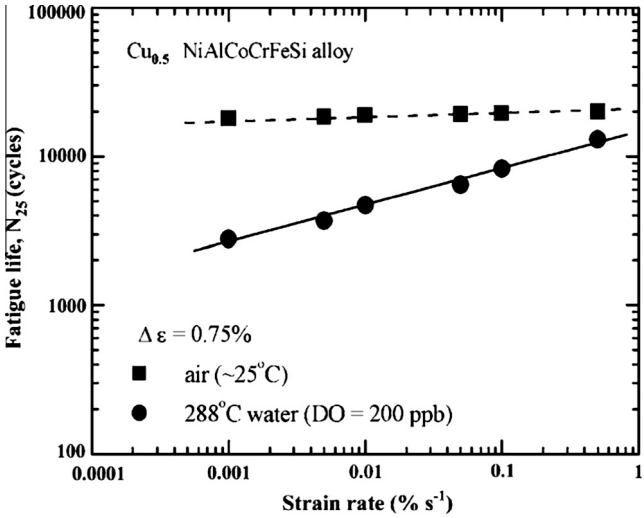

Fig. 6.3. Effect of strain rate on the fatigue lives of the $Cu_{0.5}NiAlCoCrFeSi$ alloy in air at 25 °C and 288 °C water containing 200 ppb dissolved oxygen [245].

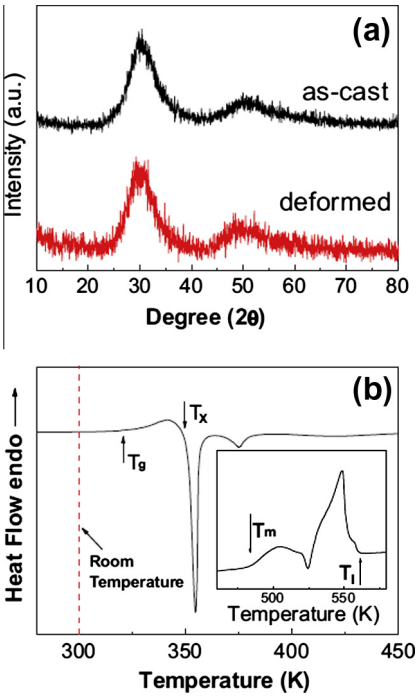

Fig. 6.4. (a) XRD patterns of $Zn_{20}Ca_{20}Sr_{20}Yb_{20}(Li_{0.55}Mg_{0.45})_{20}$ in as cast state and after 70% plastic deformation. (b) DSC traces of as cast $Zn_{20}Ca_{20}Sr_{20}Yb_{20}(Li_{0.55}Mg_{0.45})_{20}$ high-entropy BMG [35].

and can only form glass at a very high cooling rate by melt spinning (10^6 K s^{-1}), with a critical thickness of less than 50 μm. Addition of the type-I element Al in this alloy leads glass formation in bulk form with a critical size of 1–2 mm [218–220]. Subsequently, the similar element, Ni, was added to partially substitute Cu, the critical size was increased to 8 mm in the La[Cu, Ni]Al alloys [218]. Li [230] also replaced La with similar rare earth metals, Ce, Pr, and Nd, glassy rods with a 15 mm diameter were obtained. The similar method for enhancing the high-entropy effects were also found in the (Ti, Zr, Hf)–(Ni, Cu)–Al [231–242], and (Fe, Co, Ni)–(Zr, Hf, Nb, Ta, Mo, W)–B alloy systems [243,244].

6.3. Properties of high-entropy BMGs

As discussed earlier, BMGs usually have compositions close to/near the eutectic, and the content of solute elements is usually much higher than that in conventional alloys. The composition of HEAs is not too far from the BMG-forming compositions in the alloy system, as pointed out by Ma et al. [3]. In some cases, HEAs can form glass in a bulk form, even though their GFA is not the best in the system. For instance, Chen et al. [245] reported that for the $Cu_{0.5}$NiAlCoCrFeSi high-entropy BMG, the critical size for glass formation reaches 3 mm in diameter. The high-entropy BMG showed high tensile strength of about 2000 MPa at 288 °C in high-purity water. Fig. 6.3 shows the fatigue life of the $Cu_{0.5}$-NiAlCoCrFeSi BMG tested in air at 25 °C and in a simulated boiling water reactor containing 200 ppb dissolved oxygen (DO) as a function of strain rate. Note that the fatigue life of a test specimen is defined as the number of cycles for the tensile stress to drop 25% from its peak value. The results indicate that environmental effects on the fatigue life of the $Cu_{0.5}$NiAlCoCrFeSi high-entropy BMG are more pronounced in the high-temperature water than in air. In addition, the fatigue life decreases with decreasing strain rate in both environments. For instance, in a simulated boiling water reactor (BWR) environment (200 ppb DO), a reduction in the strain rate from 0.5 to 0.001% s^{-1} decreases

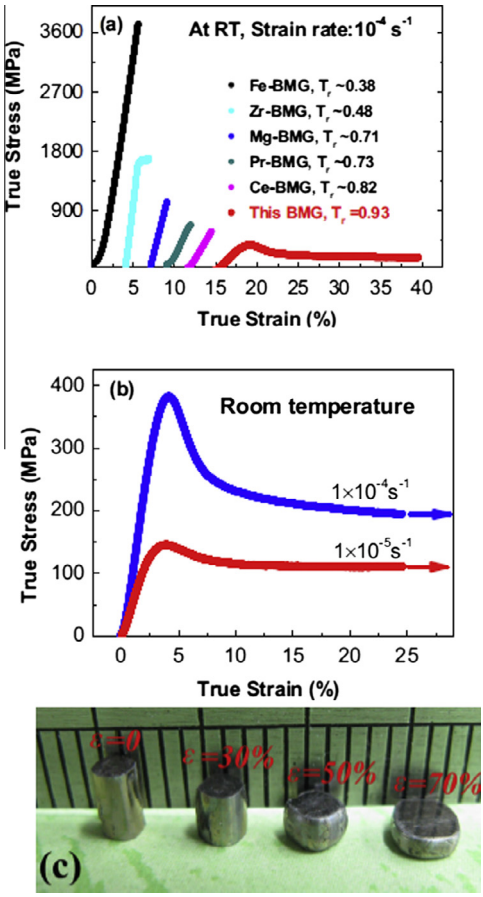

Fig. 6.5. (a) Stress–strain curves of the $Zn_{20}Ca_{20}Sr_{20}Yb_{20}(Li_{0.55}Mg_{0.45})_{20}$, $Fe_{64}Mo_{14}C_{15}B_6Er_1$, $Zr_{41}Ti_{14}Cu_{12.5}Ni_{10}Be_{22.5}$, $Mg_{65}Cu_{25}Y_9Gd_1$, $Pr_{60}Al_{10}Ni_{10}Cu_{20}$, $Ce_{62}Al_{10}Cu_{20}Co_3Ni_5$ samples. (b) Highlight the stress–strain curves for the $Zn_{20}Ca_{20}Sr_{20}Yb_{20}(Li_{0.55}Mg_{0.45})_{20}$ at strain rates of 10^{-4} and 10^{-5} s^{-1}. (c) The image of the compressed samples, they could be compressed to 70% of its original height without shear bands and cracking [35].

the fatigue life by a factor of 5, whereas the factor obtained in air is only 1.1. The good fatigue resistance of the present high-entropy BMG may be attributed to the formation of protective oxide films on the surface of the specimen in high-temperature water, leading to good overall corrosion resistance.

Gao et al. [36] reported that the SrCaYbMgZn equiatomic ratio alloys can form glassy rods with a 5 mm diameter, and this high-entropy BMG can be highly deformed at room temperature. Fig. 6.4(a) shows XRD patterns of the $Zn_{20}Ca_{20}Sr_{20}Yb_{20}(Li_{0.55}Mg_{0.45})_{20}$ alloy in its as-cast state and after 70% plastic deformation, while Fig. 6.4(b) displays the corresponding differential scanning calorimetry (DSC) traces of the as-cast specimen. Amorphous nature was confirmed by the XRD patterns in Fig. 6.4(a) for both the as-cast state and the deformed state. The DSC curve also demonstrates a distinct glass transition followed by exothermic crystallization. Fig. 6.5(a) presents the stress–strain curves of this high-entropy BMG, in comparison with that of $Fe_{64}Mo_{14}C_{15}B_6Er_1$, $Zr_{41}Ti_{14}Cu_{12.5}Ni_{10}Be_{22.5}$, $Mg_{65}Cu_{25}Y_9Gd_1$, $Pr_{60}Al_{10}Ni_{10}Cu_{20}$, and $Ce_{62}Al_{10}Cu_{20}Co_3Ni_5$ BMG samples. It can be seen that this high-entropy BMG exhibits low strength but a large plasticity. Fig. 6.5(b) compares the stress–strain curves for the $Zn_{20}Ca_{20}Sr_{20}Yb_{20}(Li_{0.55}Mg_{0.45})_{20}$ high-entropy BMG at the strain rate of 10^{-4} and 10^{-5} s^{-1}. It seems that the strength of the high-entropy BMG decreases largely with the decrease of the strain rate. Fig. 6.5(c) exhibits the SEM images of the compressed samples, demonstrating that the high-entropy

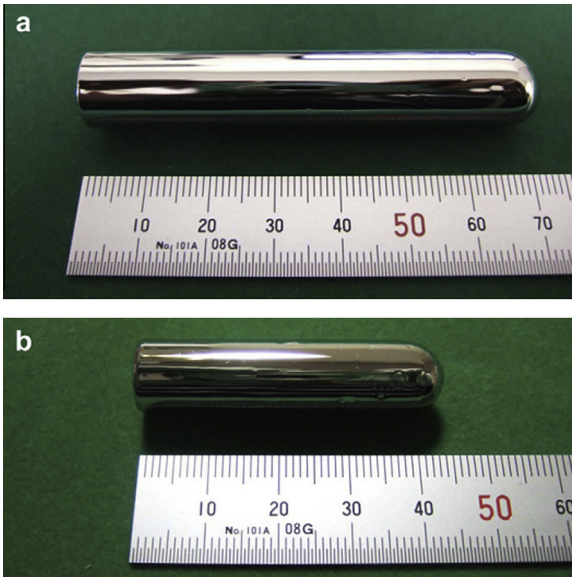

Fig. 6.6. High-entropy BMG with size of 12 and 10 mm in diameter [34].

BMG could be compressed to 70% of their original height without shear bands and cracking [36], which is unusual for BMG materials in general.

Figure. 6.6 shows the high-entropy BMGs with a composition of PdPtCuNiP with a critical size of 12 and 10 mm in diameter [34]. The cylindrical samples exhibit good metallic luster, indicating that the sample surfaces are neither oxidized nor contaminated due to the effect of B_2O_3 on excluding impurities. Furthermore, observations of the sample surfaces with unaided eyes can explain the absence of a concave shape on the millimeters to sub-millimeter scales.

Moreover, crystallization, structural relaxation and glass transition behavior of the high-entropy $(Ti_{33}Zr_{33}Hf_{33})_{50}(Ni_{50}Cu_{50})_{40}Al_{10}$, $(Ti_{25}Zr_{25}Hf_{25}Nb_{25})_{70}(Ni_{50}Cu_{50})_{20}Al_{10}$, and $(Ti_{33}Zr_{33}Hf_{33})_{70}(Ni_{33}Cu_{33}Ag_{33})_{20}Al_{10}$ BMGs were investigated in detail [239]. Structural relaxation was observed as a broad exothermic reaction prior to the onset of crystallization. All three amorphous alloys transform into a nanoscale icosahedral phase during the first exothermic DSC event. This observation indicates that the atomic complexity derived from the equiatomic substitution is effective in forming the nanoscale icosahedral phase [223,239,246,231]. However, the decomposition sequences of the icosahedral phase in these glassy alloys are entirely depending on the alloy composition. It was found that occurrence of the Zr_2Cu-type phase can increase the stability of the icosahedral phase, but formation of the Ti_2Ni-type or $MgZn_2$-type phases significantly decreases the thermal stability of the icosahedral phase [246].

7. Modeling and simulations

Largely due to the complexity of the multi-component system and disordered solid-solution structure in HEAs, predictive computational modeling of HEAs is very challenging. As a result, there are few theoretical reports on HEAs available in the open literature. However, there are increasing interests in computational modeling of HEAs to study the structure (including defects), thermodynamics, kinetics, and mechanical properties. For example, Kao et al. [247] simulated the structures of HEAs composed of up to eight elements (Ni–Al–Cu–Co–Ti–V–Zn–Zr) using tight-binding molecular dynamics. They found that the structure tends to become more random as the number of components increases in the system. Another study by Zhang et al. [248] using the CALPHAD (acronym of CALculation of PHAse Diagram) method developed the thermodynamic database for the Al–Co–Cr–Fe–Ni system. Irving

and Koch [81] have studied the elastic constants and stacking fault energies using first-principles density functional theory (DFT) [249] calculations supported by combined experiments. Calculations of elastic constants can be used to predict the mechanical stability of HEAs, and they may be correlated to the stacking-fault energy. Gao et al. [250] have used *ab initio* molecular dynamics (AIMD) simulations to predict the structure and diffusion of various HEAs, including $Al_xCoCrCuFeNi$, TiZrHfTaNb, and PdPtNiCuP. Simulations of the liquid structure can reveal rich information on the HEA formation during solidification and even in the solid state. The AIMD simulations also can predict diffusion constants. This chapter mainly focuses on DFT calculations, AIMD simulations, and CALPHAD modeling.

7.1. DFT calculations

Among available predictive computational modeling techniques, the DFT method [249] is probably the most desirable technique to tackle multicomponent alloy systems, such as HEAs. The DFT calculations only require the atomic number and crystal structure as the input and yield electronic and cohesive properties of solids. The core concept of the electronic DFT provides an exact transformation of the electronic many-body problem into a set of many coupled single-electron problems, where each electron interacts with an effective potential related to the total charge density. An unlimited number of alloys can be "virtually" processed by computers, and only promising compositions that pass the screening criteria are chosen and passed onto experiments for verification.

However, the challenge in dealing with disordered solid solution in DFT becomes intimidating when the system contains five or more components. Using the brute force approach to assemble tremendous amounts of atomic configurations due to random solid-solutions is not possible. To model disordered solid solutions using DFT methods, two popular techniques have been used. One is the special quasi-random structure (SQS) method [251,252]. Previously, SQS structures have been only applied to binary [253–255] and ternary alloys [256–258]. The SQS approach is to identify specially-designed small-unit-cell periodic structures that closely mimic the most relevant near-neighbor pair and multisite-correlation functions of random substitutional alloys. Therefore, developing SQS for 4-, 5-, and 6-component systems is necessary for HEAs. To the authors' knowledge, Niu et al. have developed SQS FCC and HCP structures for quaternary alloys [247]. The other is the Korringa-Kohn-Rostocker-coherent potential approximation (KKR-CPA) [259,260] method, and it has been widely used to study the electronic structure, thermodynamic and elastic properties of disordered solids [261–268] but mainly limited to binary alloys, although a recent study [269] extends it to ternary alloys. Recently, Wang and Gao have applied the KKR-CPA method to study the cohesive, electronic and elastic properties of $Al_xCoCrCuFeNi$ alloys [270].

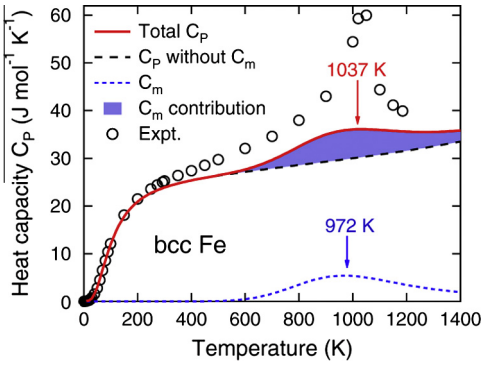

Fig. 7.1. Experimental (open circles) and calculated (curves) heat capacities of bcc Fe under pressure $P = 0$ [271]. The magnetic configurational entropy contributions (C_m) are obtained from the partition function due to the competition among magnetic states. A protrusion is clearly predicted with the maxima of 1037 K (from C_P) and 972 K (from C_m), pertaining to the Curie temperatures and close to the measured 1044 K.

One critical issue from the computational standpoint is how to calculate the total entropy of HEAs and identify the physical nature of "entropy" since the entropy of a phase of an alloy may contain multiple contributions from configuration (ΔS^{conf}), electron excitation (ΔS^{set}), lattice phonon vibration (ΔS^{ph}), magnetic spin fluctuation (ΔS^{mag}) and perhaps more:

$$\Delta S = \Delta S^{conf} + \Delta S^{el} + \Delta S^{ph} + \Delta S^{mag} \tag{7-1}$$

Note that the ideal configurational entropy is $-R\sum_{i=1}^{N} x_i \ln x_i$. It reaches its maximum, $R \ln N$, when the component mixes in an equal atomic amount.

However, strong ordering or clustering and subsequent elemental partitioning between phases are commonly observed in solid solutions (for example in AlCoCrCuFeNi [15]), and consequently, the configurational entropy can be reduced significantly. In such case, some important questions arise: will the reduced configurational entropy still be sufficient to stabilize the HEA phase? How to identify other entropy sources in addition to the configuration entropy, which may favor the HEA phase formation? One likely contribution is due to the magnetic spin fluctuation, as demonstrated in Ref. [271] (shown in Fig. 7.1). The commonly-observed anomaly in the heat capacity of magnetic materials in the vicinity of Curie temperature is believed to be due to the magnetic spin fluctuation [271], which becomes significant at high temperatures. Their work may have analogy to HEAs that contain multiple magnetic elements. It was reported in Ref. [147] that the magnetic entropy is comparable to the configurational entropy in magnitude. Less obvious contribution is from the vibrational entropy. Whether the ordered phase or disordered phase has higher vibrational entropy depends on the molar

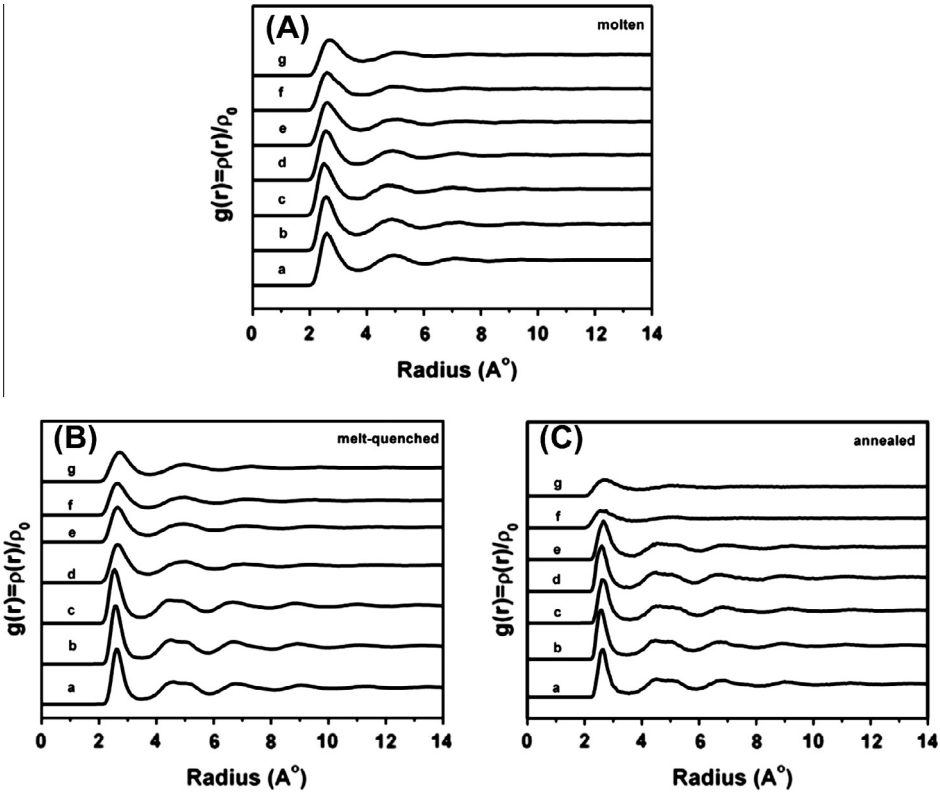

Fig. 7.2. Calculated radial distribution function (RDF) patterns of the alloys: (A) in the molten state; (B) in the melt-quenched state; (C) in the annealed state. a, Ni–Al; b, Ni–Al–Cu; c, Ni–Al–Cu–Co; d, Ni–Al–Cu–Co–Ti; e, Ni–Al–Cu–Co–Ti–V; f, Ni–Al–Cu–Co–Ti–V–Zn; g, Ni–Al–Cu–Co–Ti–V–Zn–Zr [82].

volumes, structures, and constituent elements [272,273]. For example, Muñoz et al. [274] found that the chemical ordering in the B2 structure increases the vibrational entropy by $+0.22 \pm 0.03k_B$/at, compared to the disordered B2 FeV alloy. On the other hand, Fultz et al. [275] found that disordering in L_{12} Ni_3Al has a higher vibrational entropy of $+0.2 \pm 0.1k_B$/at than the ordered structure. Delaire et al. [276] even reported negative vibrational entropies of mixing in V–6.25% Ni, Pd and Pt solid solution alloys. For V–6.25% Pt, the negative vibrational entropy of mixing even exceeds the conventional positive chemical entropy of mixing, resulting in lower Pt solubility in V.

The Helmholtz free energy, F(V,T), of a phase of an alloy can be determined according to:

$$F(V,T) = E_c(V) + F_{ph}(V,T) + F_{el}(V,T) + F_{conf}(V,T) + F_{mag}(V,T) + F_{ei\text{-}ph}(V,T) \tag{7-2}$$

where $E_c(V,T)$ is the cohesive energy at $T = 0$ K, $F_{ph}(V,T)$ is the vibrational free energy, $F_{el}(V,T)$ is the thermal electronic contribution to the free energy, $F_{conf}(V,T)$ is the contribution to the free energy from the configurational entropy, $F_{el\text{-}ph}(V,T)$ is the contribution to the free energy from the electron–phonon interaction, and P is pressure.

The electronic and vibrational contributions to entropy can be computed as follows [273,277]:

$$S_{el}(V,T) = -2k_B \int_{-\infty}^{\infty} n_{el}(\varepsilon,V)[f_{FD}\ln f_{FD} + (1-f_{FD})\ln(1-f_{FD})]d\varepsilon \tag{7-3}$$

$$S_{ph}(V,T) = 3k_B \int_{0}^{\infty} n_{ph}[(f_{BE}+1)\ln(f_{BE}+1) - f_{BE}\ln f_{BE}]d\varepsilon \tag{7-4}$$

where n_{el} is the electron density of states, n_{ph} is the phonon density of states, S_{ph} is the vibrational entropy, S_{el} is the entropy from conduction electrons, f_{BE} and f_{FD} are the Bose–Einstein and Fermi–Dirac distribution functions. If $n_{el}(\varepsilon,V)$ and $n_{ph}(\varepsilon,V)$ are known through neutron experiments or first-principles calculations, one can calculate the vibrational entropy and electronic entropy.

7.2. AIMD simulations

The significant advantage of AIMD simulations is their predictive nature, since they are based on quantum mechanics. Developing an empirical interaction potential is no longer needed, which is usually fitted to reproduce some experimental data in classical MD simulations. Since the DFT method calculates the instantaneous forces acting on atoms, AIMD simulations [278] can be used

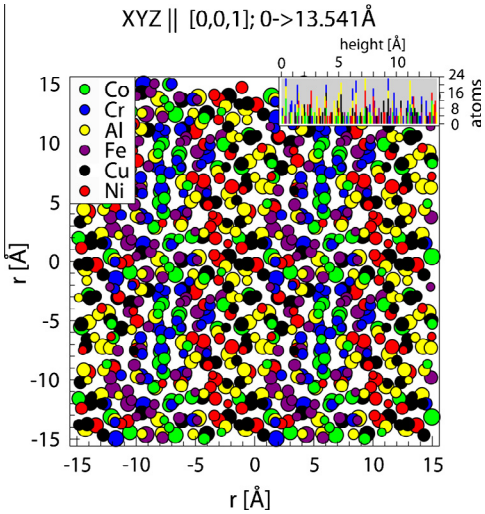

Fig. 7.3. [0 0 1] projected atomic structure of $Al_{1.3}CoCrCuFeNi$ in the liquid state after annealing at $T = 1873$ K for 30 ps [250]. Cu clustering is visible.

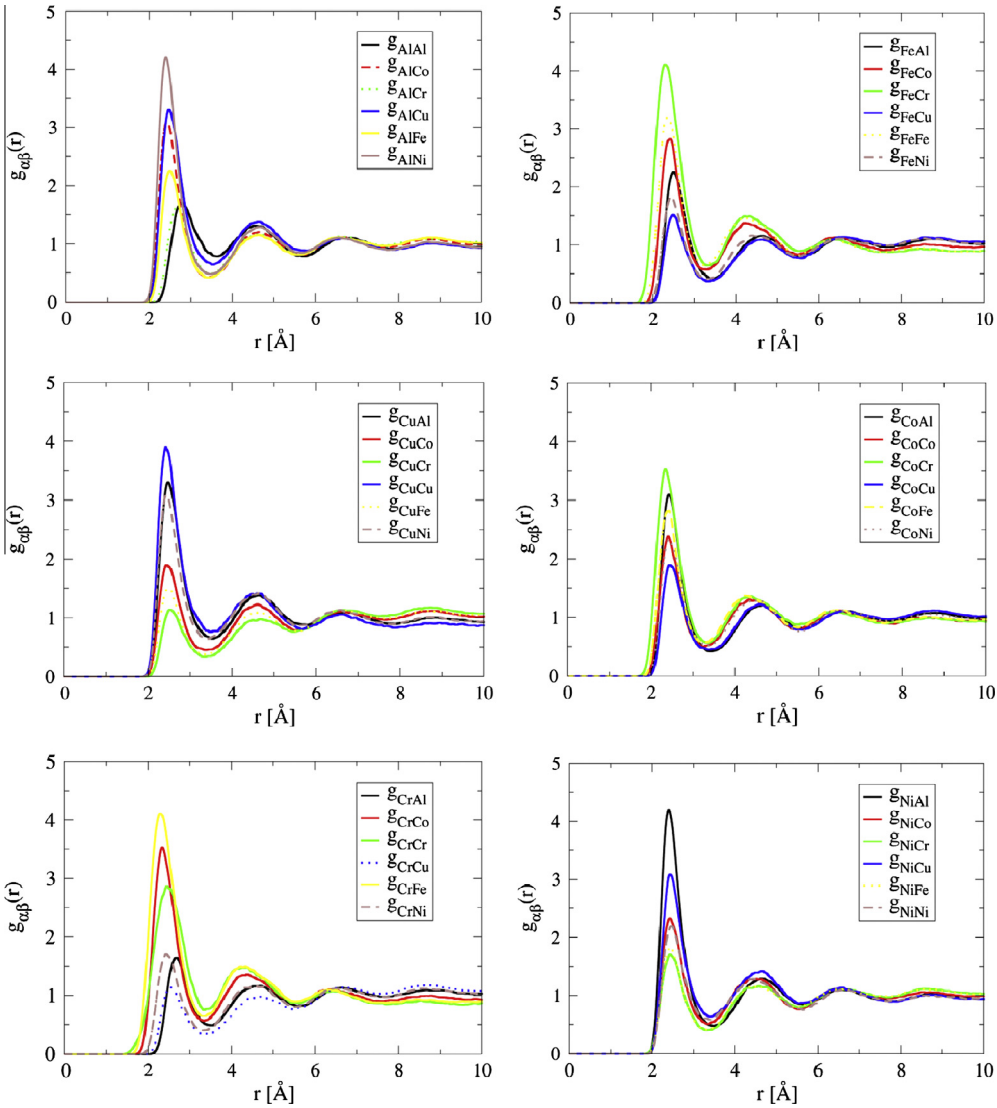

Fig. 7.4. AIMD-predicted partial pair correlation functions for $Al_{1.3}CoCrCuFeNi$ at T = 1873 K after the simulation time of 30 ps, showing Cu clustering, Al–Ni ordering, and Fe–Cr and Cr–Co ordering [250].

to predict individual atomic trajectories of solids or liquids held at a constant elevated temperature. As a matter of fact, AIMD simulations have been widely used to predict dynamic, structural, and thermodynamic properties (e.g., energy, pressure, and heat capacity) and diffusion constants at finite temperatures [279–285]. However, the tradeoff is the very high computational cost, limited to small systems (typically several hundred atoms) and a short period of time (~10–100 ps) in the solid state. The diffusion rate in the solid state is orders of magnitude smaller than that in the liquid state, and hence it is usually difficult to equilibrate the system at very low temperatures.

Using the tight-binding method, Kao et al. [82] (see Fig. 7.2) studied the structural evolution by a supercell of 4000 atoms under a constant pressure (zero applied pressure) and under periodic bound-

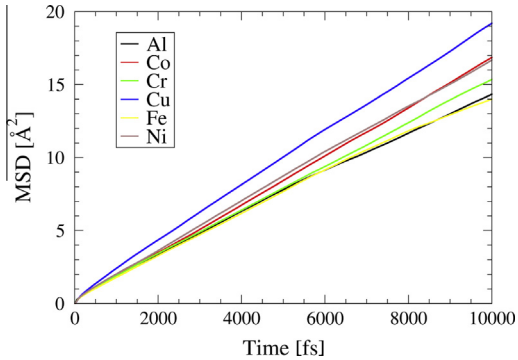

Fig. 7.5. AIMD predicted mean-square displacement for $Al_{1.3}CoCrCuFeNi$ at $T = 1873$ K after 30 ps simulation time [250]. The simulated diffusion constants at $T = 1873$ K are: Al: 2.44×10^{-5}, Co: 2.69×10^{-5}, Cr: 2.50×10^{-5}, Cu: 3.19×10^{-5}, Fe: 2.44×10^{-5}, and Ni: 2.80×10^{-5} cm^2/s.

ary conditions in the liquid, quenched, and annealed states. The systems that they studied include binary to eight-element alloys, with the elements in an equi-molar proportion and in the sequence of Ni, Al, Cu, Co, Ti, V, Zn, and Zr, i.e., the Ni–Al binary alloy, Ni–Al–Cu ternary alloy, Ni–Al–Cu–Co quaternary alloy, etc. Additional simulations on the single elements, V, Co, and Ni, were also simulated likewise for further comparison. Their work indicates that the melt-quenched alloys tend to form an amorphous structure when there are less than four elements, and that the alloys show a liquid-like solidified structure when there are five or more elements.

Gao et al. [250] has carried out AIMD simulations on $Al_xCoCrCuFeNi$ in an attempt to reveal structural evolution during solidification. The AIMD simulations were performed at a constant volume with zero pressure at various temperatures ($T = 2273$, 2073, 1873, 1673, 1523, 1273, and 1023 K) for $x = 0$, 0.5, 1, 1.3, and 3 respectively. The equilibrium volumes are determined by adjusting the supercall lattice parameter so that the thermodynamic pressure is zero at each temperature. Segregation of Cu is apparent in a [0 0 1] plane projection of $Al_{1.3}CoCrCuFeNi$ at $T = 1873$ K (see Fig. 7.3). Partial correlation function (see Fig. 7.4) shows relatively strong clustering of Cu, and ordering of Al–Ni, Fe–Cr, and Cr–Co developed in the liquid state. By examining the atomic trajectory, the diffusion constants can be obtained by plotting the mean square displacement (MSD) vs. time. It is shown that the MSD plot is quite linear and Cu diffuses fastest, about 31% faster than the slowest diffuser Al or Fe (Fig. 7.5). The simulated diffusion constants at $T = 1873$ K is: Al: 2.44×10^{-5}, Co: 2.69×10^{-5}, Cr: 2.50×10^{-5}, Cu: 3.19×10^{-5}, Fe: 2.44×10^{-5}, and Ni: 2.80×10^{-5} cm^2/s. A relatively strong Cu-clustering tendency along with the fastest Cu diffusivity qualitatively explains the experimentally-observed Cu-segregation phenomenon [248,263].

Their preliminary AIMD simulations on $Al_xCoCrCuFeNi$ HEAs [250] seems to suggest that the microstructure features observed experimentally [15,45] may be strongly correlated to the liquid-state structure. For example, the simulated partial correlation functions show relatively strong tendencies of Cu clustering and Al–Ni and Cr–Fe/Cr–Co ordering, which seems to be in agreement with experimental observations [15]. For example, the experimental study by Singh et al. [15] using three-dimensional atom probes confirmed the presence of Cu-rich precipitates, Al–Ni-rich plates, and Cr–Fe–rich interpolates of different morphologies in the cast AlCoCrCuFeNi HEA. An earlier experimental study by Tong et al. [45] also confirmed the Cu segregation that the Cu content is as high as 78.5 at.% in the interdendritic regions of small volume fractions for all seven $Al_xCoCrCuFeNi$ HEAs studied.

Gao et al. [250] has extended AIMD simulations to other HEA alloys, including TiZrHfTaNb (Fig. 7.6) and amorphous PdPtNiCuP (Fig. 7.7). Significant contrast was observed in their liquid structures. For example, all the partial correlation functions observed in TiZrHfTaNb indicates a fairly uniform chemical distribution in the liquid, e.g., lack of strong short-range ordering or segregation. Perhaps this trend contributes to a large degree to the uniform equi-axed microstructure experimentally observed by Senkov et al. [126]. In fact, the binary phase diagrams among the constituent elements show for-

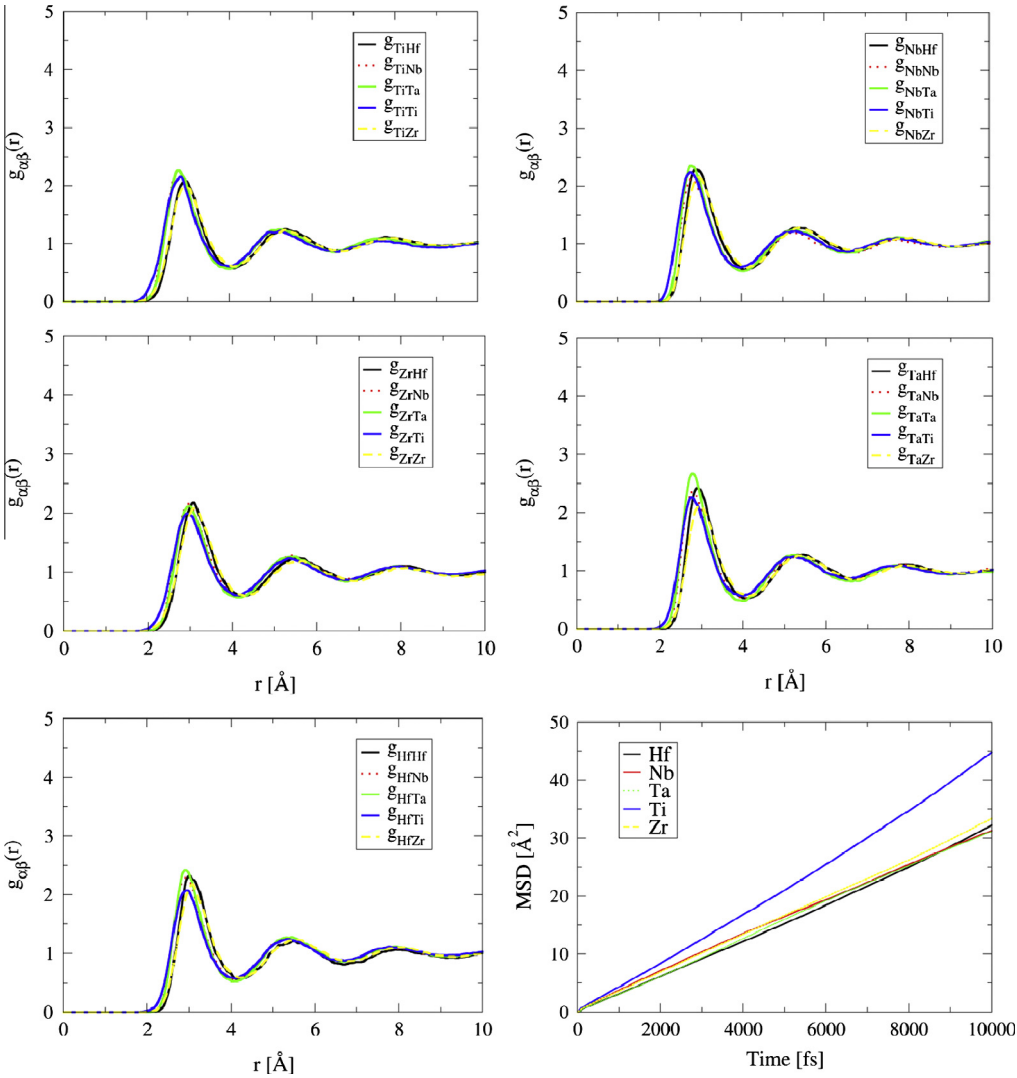

Fig. 7.6. AIMD-predicted partial pair correlation functions and mean square displacement plot for HEA TiZrHfTaNb at $T = 2773$ K after 35 ps simulation time, showing lack of short-range ordering or clustering [250]. The simulated diffusion constants are: Hf: 5.02×10^{-05}, Nb: 5.43×10^{-05}, Ta: 5.31×10^{-05}, Ti: 6.92×10^{-05}, and Zr: 5.44×10^{-05} cm^2/s.

mation of isomorphous solid solution and lack of intermetallic compounds. The simulated diffusion constants are: Hf: 5.02×10^{-05}, Nb: 5.43×10^{-05}, Ta: 5.31×10^{-05}, Ti: 6.92×10^{-05}, and Zr: 5.44×10^{-05} cm^2/s. The trend in the diffusion constants in the descending order (Ti > Nb ~ Zr > Ta > Hf) seems to follow the order of the atomic size and weight of the constituent elements, further confirming lack of strong chemical ordering.

Conversely, very strong short-range ordering of Ni–P, followed by Pt–P and Pd–P, were predicted in PdPtNiCuP at $T = 1200$ K. The ordering tendency becomes stronger as the temperature is lowered during solidification. As a result, quenching is required to suppress crystallization to form an amorphous state. The simulated diffusion constants are Cu: 1.01×10^{-5}, Ni: 8.10×10^{-6}, P: 8.81×10^{-6}, Pd: 7.36×10^{-6}, Pt: 7.70×10^{-6} cm^2/s. Although P atoms are 20% smaller than Cu atoms, Cu diffuses

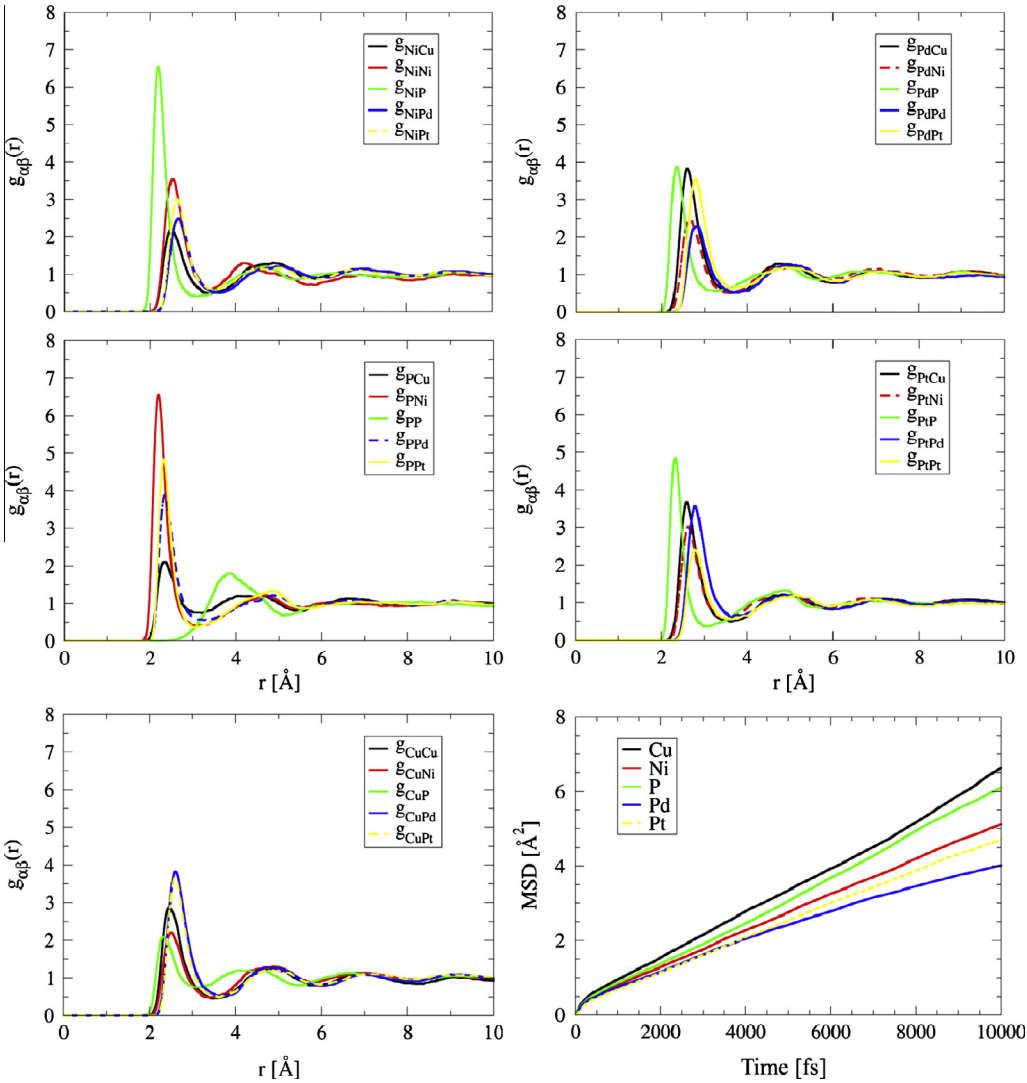

Fig. 7.7. AIMD-predicted partial pair correlation functions and mean square displacement plot for PdPtNiCuP at T = 1200 K after 30 ps simulation time, showing strong ordering between P and Ni [250]. The simulated diffusion constants are Cu: 1.01×10^{-5}, Ni: 8.10×10^{-6}, P: 8.81×10^{-6}, Pd: 7.36×10^{-6}, and Pt: 7.70×10^{-6} cm^2/s.

the fastest. The reason is due to formation of strong short range ordering of P–Ni pairs followed by P–Pt pairs while the correlations associated with Cu are the weakest overall.

Based on the present AIMD simulations of various HEAs in comparison with available experiments, it is tempting to suggest the following guidelines in searching for new HEAs with improved properties using AIMD simulations:

(1) Promote the formation of homogenous solid solutions by avoiding strong chemical segregation and formation of detrimental intermetallics, starting in the liquid state.

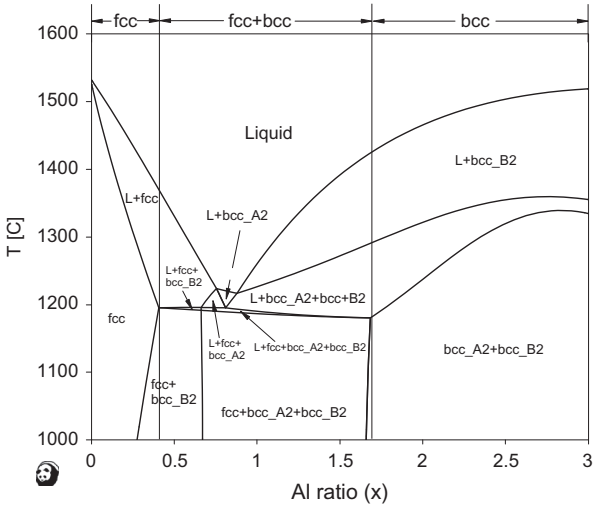

Fig. 7.8. the calculated isopleth of the $Al_xCoCrFeNi$ alloys with $x = 0–3$ using our current thermodynamic description [248].

(2) Maintain equivalent or comparable diffusivity among principal elements to control the kinetics of phase transformation aiming toward forming more or less homogenous microstructures during cooling.

These guidelines are complementary to the empirical rules (i.e. heat of mixing and atomic size difference) for HEA formation as addressed in Section 2. Combining them will accelerate design of new HEAs.

7.3. CALPHAD modeling

Compared to DFT calculations and AIMD simulations, the CALPHAD method allows users to perform thermodynamic and kinetic calculations based on the phenomenological approach [286–288] that are used to quantity Gibbs free energies of individual phases and mobility in a system. Typical thermodynamic calculations include but are not limited to phase compositions, phase fractions, and phase stability as a function of composition, temperature, and pressure.

Very recently, Zhang et al. [248] developed a thermodynamic database for the Al–Co–Cr–Fe–Ni system. Their emphasis was placed on the interaction parameters of lower-order constituent systems that are usually the most effective and important to obtain a reliable higher-order thermodynamic database. There are no higher-order (quaternary or quinary) interaction parameters used in their thermodynamic database [248] as a first approximation. Fig. 7.8 shows the vertical section of the $Al_xCoCrFeNi$ for the Al ratio from 0 to 3. This figure predicts the phase stability with respect to Al contents in the $Al_xCoCrFeNi$ alloy. It is seen that the primary solidified phase is FCC when $x < 0.75$, and it is BCC and B2, which solidifies first, when $x > 0.75$, which seem to be generally consistent with the experimental results [248].

Non-equilibrium solidification path simulations was performed [248] using the Scheil model, as shown in Fig. 7.9 to illustrate the fraction of solids during solidification in the $Al_xCoCrFeNi$ alloys. It is seen that the calculation predicts the formation of a BCC phase of 2.3% when $x = 0.3$, as experimentally observed by Kao et al. [146]. Fig. 7.10 presents the equilibrium phases change with respect to composition of the Al_xCoCr_yFeNi alloys homogenized at 1373 K. This trend indicates that the BCC phase region increases, and the FCC/FCC + BCC region decreases with increasing the Cr concentration, demonstrating that Cr stabilizes the BCC phase. When the Cr ratio, x, equals to 2.0, no pure FCC phase

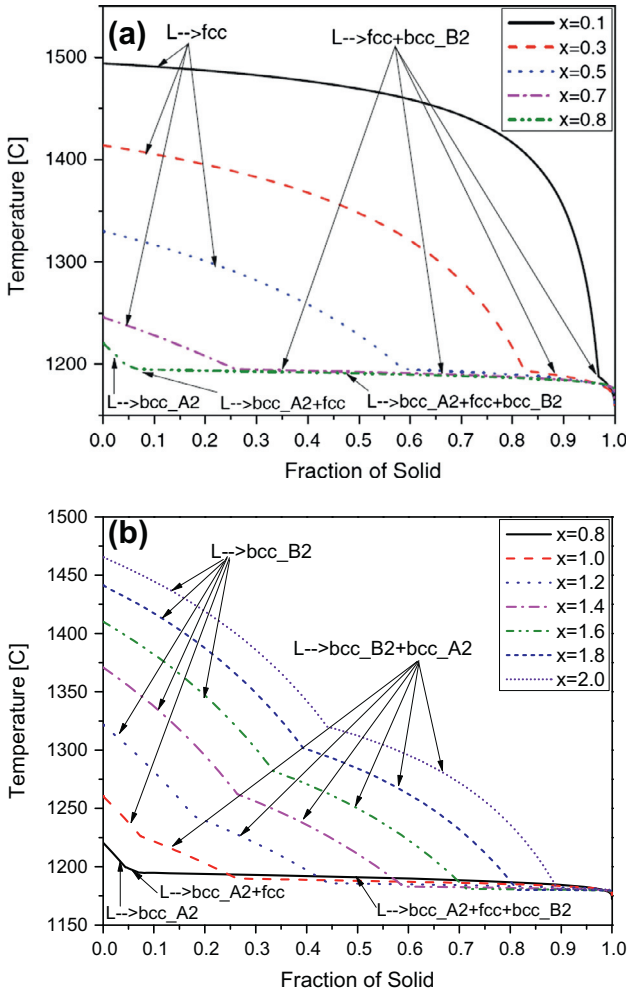

Fig. 7.9. Solidification paths calculated by the Scheil model for the $Al_xCoCrFeNi$ alloys using our current thermodynamic database: (a) $x = 0.1–0.8$; (b) $x = 0.8–2$ [231].

region can form within the Al_xCoCr_2FeNi alloys. The effect of other elements in the phase stability of BCC/FCC is also calculated in the paper [248].

8. Future development and research

HEAs are based on the multi-principal elements concept, which has stimulated rising interests for basic science and applications. The potential applications of HEAs are mainly based on their unique properties. Their excellent high-temperature properties may provide the potential to replace the Ni-based superalloy, e.g., AlCoCrFeNi, which is expected to be of lighter weight and lower cost. It is also reported that HEAs can be used as thermal barrier coatings for the Ti-based alloys and a diffusion barrier between Cu and Si in the integrated circuit (IC) industries. The excellent wear resistance makes HEAs useful for mold materials. There are also reports using HEAs in the 4-mode-ring laser Gyro. The HEAs carbides and nitrides are potentially applicable as coatings for the biomedical materials, and the near constant resistivity in 4.2–360 K could make the $Al_{2.08}CoCrFeNi$ HEA useful for electronic

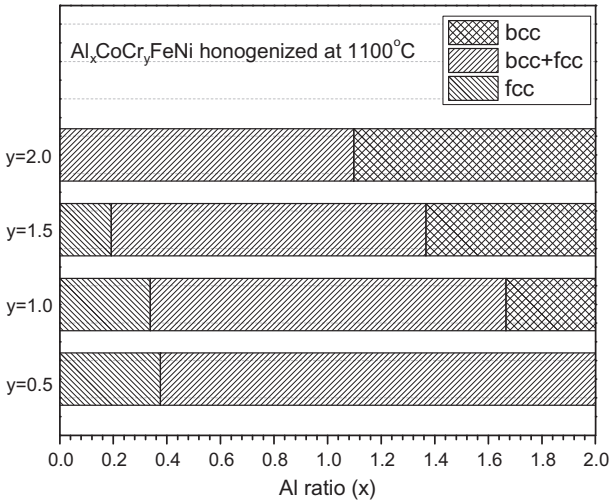

Fig. 7.10. the calculated transition ranges of the Al_xCoCr_yFeNi alloys homogenized at 1100 °C [248].

device parts. In this chapter, future directions are proposed in the broad areas of fundamental understanding, processing and applications.

8.1. Fundamental understanding of HEAs

Quantifying the entropy sources of HEAs remains to be the most important topic in fundamental understanding of HEA formation. In this regard, inelastic neutron scattering and nuclear resonant inelastic X-ray scattering will be very useful techniques to measure phonon spectra as demonstrated by Fultz et al. in a number of ordered and disordered alloys [272–276,289–291]. In real solid solution alloys ordering and/or clustering always destroy configurational entropy of mixing, so precise calculation of configurational entropy of mixing in HEAs is needed. Typical methods for this purpose include cluster variation method (CVM), general algorithms, and Monte Carlo simulations.

From the point of view of materials design, one needs phase diagram information, e.g. the phase field of a high-entropy phase in the space of composition and temperature as well as important competing ordered compounds phase(s). In order to expedite phase diagram determination, the approach that combines DFT calculations, high-throughput experiments [292,293] and CALPHAD modeling is a wise choice as reported previously [38,294–298]. Establishing reliable self-consistent thermodynamic database using the CALPHAD method not only facilitates phase diagram visualization for more than 5 component systems but also can be used to directly calculate the entropy, enthalpy and Gibbs free energy of the high-entropy phase as a function of temperature and composition.

It has been critically claimed there exist severe lattice distortion effect and sluggish diffusion effect in HEAs. However, precise measurements to quantify these effects are still lacking. Computer simulations in this regard will be important. However, calculating the diffusion coefficient of HEAs using DFT methods can be a daunting task due to the large configurational space in the highly concentrated alloys.

Additional topics in addressing fundamental understanding of HEAs are:

(1) Quantifying the enthalpy of the high-entropy phase since it is the Gibbs free energy that determines the phase stability at constant temperature and pressure. Experimental measurements such as heat of solution and heat capacity are important. Computational study using DFT and CALPHAD will be very useful to calculate how enthalpy of mixing changes with composition, which in turn can help identify HEA composition.

(2) HEAs have the high chemical disorder. Amorphous alloys have high topological disorder. Hence, HEAs are alloys just in between the conventional alloys and the amorphous alloys. The plastic deformation structural units are typically dislocations and twins in the conventional crystalline alloys, and typically STZs and TTZs in the amorphous alloys. Thus, what would be the deformation mechanism in HEAs? Dedicated experiments and simulations on plastic deformation of HEAs are needed, for example, using the single-crystal of HEAs with BCC and FCC structures, although there have accumulated reports on tension, compression, and hardness experiments on HEAs.
(3) The micro- and nano-structures of HEAs after plastic deformation may require further study by the high-resolution TEM, neutron diffraction, and synchrotron high-energy X-ray diffractions, etc., to provide the deformation mechanism of HEAs.
(4) Limited results about the fatigue behaviors for the HEAs have been obtained. More work on the BCC, BCC + FCC, and FCC structured HEAs needs to be done, especially the high-temperature fatigue properties.
(5) To study the environmental properties of HEAs, dedicated experiments in air, moisture air, water vapor, CO, hydrogen, H_2S etc. at elevated temperature need to be conducted.
(6) Creep performance of HEAs as structural materials need to be studied.

8.2. Processing and characterization of HEAs

Materials properties are dictated by their microstructure. There is no exception for HEAs. The microstructure can be manipulated by fabrication methods (see Section 3), plastic deformation (e.g. rolling, forging), and heat treatment. Casting and powder metallurgy can be employed to obtain near net shape products. Thorough characterization of the microstructure of HEAs in 3-dimension are important in interpreting materials properties such as fracture toughness and fracture mechanisms. The progress in 3D microstructure characterization and digital construction can be found in review articles [299,300]). In this regard, grain boundary character and chemistry distribution (for reviews see [299,301]) are important future research topics for HEAs. For example, controlled thermo-mechanical processing can be used to promote formation of preferred grain texture and/or grain boundary character distribution. In addition, listed below are some useful topics:

(1) The nano-sized pillars can be fabricated from the as-prepared HEAs using focus ion beams (FIB), and the pillars of single phase with desirable properties can be manufactured, and they can be the Genes for the materials. Then the new materials can be designed based on the properties of the Genes.
(2) Large plastic deformation can be used to refine the structure to submicro- or nano-scale using equal channel angular pressing method. Porous HEAs materials with controllable pore sizes in micro- to nano-sized scale can be processed using chemical or casting methods. The porous HEAs would be used as robust filters for purifying the water and air or the hot smokes at elevated temperatures and hostile environment.
(3) Detailed deformation and fracture mechanisms have not been clearly identified. The dislocation structures before and after the fracture will need to be investigated. Understanding the interaction between dislocations and solutes will provide insights into the effects of the alloying elements on the ductility of the alloy. In addition, for fatigue study, only limited data were reported and only at room temperature, but fatigue behavior at elevated temperatures needs to be explored. It is believed that a reduction in the number of the defects, such as aluminum oxide inclusions and micro-cracks, may result in a strong fatigue behavior. How to reduce these defects is particularly crucial for improving the fatigue resistance of HEAs.

8.3. Applications of HEAs

HEAs hold the potential in a wide range of applications such as functional and structural materials. The concept of HEAs can also be applied to ceramics, polymer and even liquid. As an extension to Section 4, here are some promising opportunities for HEAs:

(1) HEAs can be used as the transitional layer between the two types of alloys, e.g., the HEA solder used for welding pure titanium and chromium–nickel–titanium stainless steel [302]; and HEAs brazing filler metal used for welding cemented carbide and steel, which provides good flexibility of the brazing filler metal and favorable manufacture and installation process [303].
(2) HEAs can exhibit excellent super-paramagnetic properties, ferromagnetic properties, and soft magnetic properties.
(3) HEAs could be used in the nuclear industries. Their much high irradiation resistance and high corrosion resistance would make HEAs potential candidates for the cladding materials used for the nuclear fuels and high pressure vessels.
(4) The high-entropy concept could be used to simulate the fission process of nuclear reactors. The nuclear fission process is a process with entropy increasing, because the types of the elements are increasing with the nuclear fission reactions.
(5) HEAs may be used as heat-resistant or wear-resistant coatings. New technologies are needed to make the HEAs coating more uniform and with high cohesion with substrates.
(6) The refractory metal HEAs may be used as thermal barrier coatings, which needs to be investigated.
(7) HEAs carbides and nitrides would also be interesting for their unique properties. They may have the structures of amorphous or solid solutions, and with high hardness and strength. They may potentially be usable as diffusion barriers, and hard coatings on the tool cutting steels or the high speed steels. Recent work also shows that the high-entropy carbides and nitrides can potentially be used as biomedical coatings [151]
(8) The special physical properties of the HEAs, e.g., $Al_{2.08}CoCrFeNi$, with near constant resistivity would make them useful for electronic applications. Thus, this kind of HEAs needs to be further studied.
(9) Light-weight HEAs could be used as casings for the mobile facilities, battery anode materials, and transportation industry.

9. Summary

As a new class of materials that contain multi-principal-elements, HEAs have demonstrated unique and attractive engineering properties. The present paper has reviewed the formation criteria, thermodynamics, processing, kinetics, mechanical properties, and computer modeling of HEAs, as summarized as follows:

The four core effects of the HEAs have been summarized to understand the HEAs; the parameters, such as, enthalpy of mixing, atomic size difference, Ω, VEC, have been used to predict the phase formation for the HEAs.

Multiple-processing methods, such as arc melting, inductive melting, sputter, laser cladding, and electrochemical, have been summarized.

The HEAs with special properties have been elaborated one by one, e.g., the super high strength of BCC HEAs, and high wear resistance HEAs, high strength HEAs at high temperatures, Kondo-like behaviors HEAs, good fatigue resistance, etc.

The plastic deformation and fracture mechanism of HEAs have been discussed from the stand points of the crackling noise and the serrations on the stress–strain curves.

High-entropy BMGs lack both long-range chemical order and the topological order, which enable them possess special structures and properties. Understanding the formation mechanism of high-entropy BMGs is helpful to gain new insights into the formation mechanism of metallic glasses and others in the materials.

Preliminary computer simulations and modeling work have been briefly summarized, and more efforts in this topic need to be carried out so that the fundamentals and structures of the HEAs can be well understood.

In summary, HEAs provide a new challenge to the materials scientists. With the in-depth work on HEAs, more and more special properties of HAEs will be characterized and developed in the future. With the advanced technologies developed for the processing and characterizations of HEAs, 1-dimensional (1-d), HEA wires; 2-dimensional (2-d), HEA films; and 3-dimensional (3-d), bulk HEA samples

will be fabricated and studied. The phase-formation thermodynamics, kinetics and processing, and computer modeling and simulations, etc., for HEAs will be extensively studied, which will lead the materials scientists into a new and wonderful materials-science world.

Disclaimer

This report was prepared as an account of work sponsored by an agency of the United States Government. Neither the United States Government nor any agency thereof, nor any of their employees, makes any warranty, express or implied, or assumes any legal liability or responsibility for the accuracy, completeness, or usefulness of any information, apparatus, product, or process disclosed, or represents that its use would not infringe privately owned rights. Reference herein to any specific commercial product, process, or service by trade name, trademark, manufacturer, or otherwise does not necessarily constitute or imply its endorsement, recommendation, or favoring by the United States Government or any agency thereof. The views and opinions of authors expressed herein do not necessarily state or reflect those of the United States Government or any agency thereof.

Acknowledgements

The authors are indebted to Prof. G.L. Chen, who passed away in 2011, for his pioneering work in HEAs and academic guidance. The authors are also grateful to Prof. W.K. Wang, Prof. W.H. Wang, Prof. Y. Li, Prof. H.A. Davies, Prof. Z.Q. Sun, Prof. T.G. Nieh, Prof. X.D. Hui, Prof. J.P. Lin, Dr. Y.Q. Cheng, and Dr. G.Y. Wang for valuable discussion, comments and advices. Z.Y. is grateful to the financial support of the National Natural Science Foundation of China (Grant Nos. 50971019, 51010001 and 51001009), 111 Project (B07003) and Program for Changjiang Scholars and Innovative Research Team in University. P.K.L. appreciates the support from the US National Science Foundation (DMR-0909037, CMMI-0900271, and CMMI-1100080), the Department of Energy (DOE), Office of Nuclear Energy's Nuclear Energy University Program (NEUP) 00119262, and the DOE, Office of Fossil Energy, National Energy Technology Laboratory (DE-FE-0008855). K.A.D and P.K.L thank DOE for the support through project DE-FE-0011194 with the project manager, S. Markovich. M.C.G and P.K.L very much appreciates the support from the U.S. Army Research Office project (W911NF-13-1-0438) with the program manager, S.N. Mathaudhu. M.C.G. acknowledges support of the Innovative Processing and Technologies Program of the National Energy Technology Laboratory's (NETL) Strategic Center for Coal under the RES contract DE-FE-0004000. This work used the computing facility at Texas Advanced Computing Center (TACC) through Award# DMR120048 by the Extreme Science and Engineering Discovery Environment (XSEDE), which is supported by National Science Foundation grant number OCI-1053575.

References

[1] Cantor B, Chang ITH, Knight P, Vincent AJB. Microstructural development in equiatomic multicomponent alloys. Mater Sci Eng, A 2004;375–377:213–8.
[2] Yeh JW, Chen SK, Lin SJ, Gan JY, Chin TS, Shun TT, et al. Nanostructured high-entropy alloys with multiple principal elements: novel alloy design concepts and outcomes. Adv Eng Mater 2004;6(5):299–303.
[3] Ma D, Tan H, Zhang Y, Li Y. Correlation between glass formation and type of eutectic coupled zone in eutectic alloys. Mater Trans 2003;44(10):2007–10.
[4] Zhang Y, Yang X, Liaw PK. Alloy design and properties optimization of high-entropy alloys. JOM 2012;64(7):830–8.
[5] Zhang Y, Ma SG, Liaw PK, Tang Z, Cheng YQ. Broad guidelines in predicting phase formation of high-entropy alloys, MRS Communications, submitted for publication.
[6] Ma SG, Zhang Y, Liaw PK. Damping behaviors of $Al_xCoCrFeNi$ high-entropy alloys by a dynamic mechanical analyzer, J Alloy Compd, in preparation.
[7] Zhang Y, Zuo TT, Liaw PK, Cheng YQ. High-entropy alloys with high saturation magnetization and electrical resistivity. Sci Rep 2013;3:1455. http://dx.doi.org/10.1038/srep01455.
[8] Yang X, Zhang Y, Liaw PK. Microstructure and compressive properties of TiZrNbMoVx high-entropy alloys. Proc Eng 2012:292–8.
[9] Yeh JW. Recent progress in high-entropy alloys. Presentation at Changsha meeting; 2011.
[10] Zhang Y, Wang XF, Chen GL, Qiao Y. Effect of Ti on microstructure and properties of $CoCrCuFeNiTi_x$ high-entropy alloys. Ann Chim Sci Matér 2006;31(6):699–709.
[11] Yeh JW, Lin SJ, Chin TS, Gan JY, Chen SK, Shun TT, et al. Formation of simple crystal structures in Cu–Co–Ni–Cr–Al–Fe–Ti–V alloys with multiprincipal metallic elements. Metall Mater Trans A 2004;35(8):2533–6.

[12] Zhou YJ, Zhang Y, Wang YL, Chen GL. Solid solution alloys of $AlCoCrFeNiTi_x$ with excellent room-temperature mechanical properties. Appl Phys Lett 2007;90(18):181904.
[13] Wang XF, Zhang Y, Qiao Y, Chen GL. Novel microstructure and properties of multicomponent $CoCrCuFeNiTi_x$ alloys. Intermetallics 2007;15(3):357–62.
[14] Senkov ON, Wilks GB, Scott JM, Miracle DB. Mechanical properties of $Nb_{25}Mo_{25}Ta_{25}W_{25}$ and $V_{20}Nb_{20}Mo_{20}Ta_{20}W_{20}$ refractory high entropy alloys. Intermetallics 2011;19:698–706.
[15] Singh S, Wanderka N, Murty BS, Glatzel U, Banhart J. Decomposition in multi-component AlCoCrCuFeNi high-entropy alloy. Acta Mater 2011;59:182–90.
[16] Senkov ON, Wilks GB, Miracle DB, Chuang CP, Liaw PK. Refractory high-entropy alloys. Intermetallics 2010;18(9):1758–65.
[17] Zhang Y, Zhou YJ, Lin JP, Chen GL, Liaw PK. Solid-solution phase formation rules for multi-component alloys. Adv Eng Mater 2008;10(6):534–8.
[18] Li C, Li JC, Zhao M, Jiang Q. Effect of alloying elements on microstructure and properties of multiprincipal elements high-entropy alloys. J Alloy Compd 2009;475(1–2):752–7.
[19] Chang HW, Huang PK, Davison A, Yeh JW, Tsau CH, Yang CC. Nitride films deposited from an equimolar AlCrMoSiTi alloy target by reactive direct current magnetron sputtering. Thin Solid Films 2008;516(18):6402–8.
[20] Zhang Y, Chen GL, Gan CL. Phase change and mechanical behaviors of $Ti_xCoCrFeNiCu_{1-y}Al_y$ high entropy alloys. J ASTM Int 2010;7(5):102527.
[21] Zhang Y. Mechanical properties and structures of high entropy alloys and bulk metallic glasses composites. Mater Sci Forum 2010;654–656:1058–61.
[22] Zhang Y, Zhou YJ. Solid solution formation criteria for high entropy alloys. Mater Sci Forum 2007;561–565:1731–9.
[23] Zhang Y, Zhou YJ, Hui XD, Wang ML, Chen GL. Minor alloying behavior in bulk metallic glasses and high-entropy alloys. Sci China, Ser G 2008;51(4):427–37.
[24] Cai H, Zhang H, Zheng H. Soft magnetic devices applied for low zero excursion four-mode ring laser gyro. IEEE Trans Magn 2007;43(6):2686–8.
[25] Zhang H, Pan Y, He Y, Jiao H. Microstructure and properties of 6FeNiCoSiCrAlTi high-entropy alloy coating. Appl Surf Sci 2011;257(6):2259–63.
[26] Lin C, Tsai H, Bor H. Effect of aging treatment on microstructure and properties of high-entropy $Cu_{0.5}CoCrFeNi$ alloy. Intermetallics 2010;18:1244–50.
[27] Lin C, Tsai H. Evolution of microstructure, hardness, and corrosion properties of high-entropy $Al_{0.5}CoCrFeNi$ alloy. Intermetallics 2011;19(3):288–94.
[28] Yang X, Zhang Y. Prediction of high-entropy stabilized solid solution in multi-component alloys. Mater Phys Chem 2012;132(2–3):233–8.
[29] Greer AL. Confusion by design. Nature 1993;366:303.
[30] Canton B, Audebert F, Galano M, Kim KB, Warren PJ. Novel multicomponent alloys. Warren J Metastable Nanocryst Mater 2005;24–25:1–6.
[31] Canton B. Stable and metastable multicomponent alloys. Ann Chim Sci Mater 2007;32:245–56.
[32] Yeh JW. Private discussion; 2012.
[33] Cantor B. High-entropy alloys. In: Buschow KHJ, Cahn RW, Flemings MC, Ilschner B, Kramer EJ, Mahajan S, Veyssière P, editors. Encyclopedia of materials: science and technology. ISBN 978-0-08-043152-9 (last update October 2011).
[34] Takeuchi A, Chen N, Wada T, Yokoyama Y, Kato H, Inoue A, et al. $Pd_{20}Pt_{20}Cu_{20}Ni_{20}P_{20}$ high-entropy alloy as a bulk metallic glass in the centimeter. Intermetallics 2011;19(10):1546–54.
[35] Zhao K, Xia XX, Bai HY, Zhao DQ, Wang WH. Room temperature homogeneous flow in a bulk metallic glass with low glass transition temperature. Appl Phys Lett 2011;98:141913.
[36] Gao XQ, Zhao K, Ke HB, Ding DW, Wang WH, Bai HY. High mixing entropy bulk metallic glasses. J Non-Cryst Solids 2011;357:3557–60.
[37] Yeh JW. Recent progress in high-entropy alloys. Ann Chim Sci Mater 2006;31(6):633–48.
[38] Gao MC, Ünlü N, Mihalkovic M, Widom M, Shiflet GJ. Glass formation, phase equilibria, and thermodynamic assessment of the Al–Ce–Co system assisted by first-principles energy calculations. Metall Mater Trans A 2007;38(10):2540–51.
[39] Martyushev LM, Seleznev VD. Maximum entropy production principle in physics, chemistry and biology. Phys Rep 2006;426:1–45.
[40] Lucas MS, Wilks GB, Mauger L, Munoz JA, Senkov ON, Michel E, et al. Absence of long-range chemical ordering in equimolar FeCoCrNi. Appl Phys Lett 2012;100(25). 251907-4.
[41] Yeh JW, Chang SY, Hong YD, Chen SK, Lin SJ. Anomalous decrease in X-ray diffraction intensities of CuNiAlCoCrFeSi alloy systems with multi-principal elements. Mater Chem Phys 2007;103:41–6.
[42] Ranganathan S. Alloyed pleasures: multimetallic cocktails. Curr Sci 2003;8:1404–6.
[43] Yang X, Zhang Y. Cryogenic resistivities of NbTiAlVTaLax, CoCrFeNiCu and CoCrFeNiAl high entropy alloys. In: Zhang YF, Su CW, Xia H, Xiao PF, editors. Advanced materials and processing 2010, proceedings of the 6th international conference on ICAMP, Yunnan, 19–3 July 2010.
[44] Kao YF, Chen TJ, Chen SK, Yeh JW. Microstructure and mechanical property of As-cast, homogenized, and deformed $Al_xCoCrFeNi$ ($0 \leqslant x \leqslant 2$) high-entropy alloys. J Alloy Compd 2009;488:57–64.
[45] Tong CJ, Chen YL, Yeh JW, Lin SJ, Chen SK, Shun TT, et al. Microstructure characterization of $Al_xCoCrCuFeNi$ high-entropy alloy system with multiprincipal elements. Metall Mater Trans A 2005;36(4):881–93.
[46] Kao YF, Chen SK, Sheu JH, Lin JT, Lin WE, Yeh JW, et al. Hydrogen storage properties of multi-principal-component $CoFeMnTi_xV_yZr_z$ alloys. Int J Hydrogen Energy 2010;35:9046–59.
[47] Ukai S, Mizuta S, Fujiwara M, Okuda T, Kobayashi T. Development of 9Cr-ODS martensitic steel claddings for fuel pins by means of ferrite to austenite transformation. J Nucl Sci Technol 2002;39(7):778–88.
[48] Tomota Y, Suzuki T, Kanie A, Shiota Y, Uno M, Moriai A, et al. In situ neutron diffraction of heavily drawn steel wires with ultra-high strength under tensile loading. Acta Mater 2005;53:463–7.

[49] Choi JK, Seo DH, Lee JS, Um KK, Wung-Yong Choo WY. Formation of ultrafine ferrite by strain-induced dynamic transformation in plain low carbon steel. ISIJ Int 2003;43(5):746–54.
[50] Teng ZK, Liu CT, Ghosh G, Liaw PK, Fine ME. Effects of Al on the microstructure and ductility of NiAl-strengthened ferritic steels at room temperature. Intermetallics 2010;18:1437–43.
[51] Teng ZK, Miller MK, Ghosh G, Liu CT, Huang S, Russell KF, et al. Characterization of nanoscale NiAl-type precipitates in a ferritic steel by electron microscopy and atom probe tomography. Scripta Mater 2010;63:61–4.
[52] Huang S, Worthington DL, Asta M, Ozolins V, Ghosh G, Liaw PK. Calculation of impurity diffusivities in α-Fe using first-principles methods. Acta Mater 2010;58:1982–93.
[53] Teng ZK, Liu CT, Miller MK, Ghosh G, Kenik EA, Huang S, et al. Room temperature ductility of NiAl-strengthened ferritic steels: effects of precipitate microstructure. Mater Sci Eng, A 2012;54:22–7.
[54] Teng ZK, Zhang F, Miller MK, Liu CT, Huang S, Chou YT, et al. Thermodynamic modeling and experimental validation of the Fe–Al–Ni–Cr–Mo alloy system. Mater Lett 2012;71:36–40.
[55] Huang S, Brown D, Clausen B, Teng ZK, Gao YF, Liaw PK. In situ neutron-diffraction studies on the creep behavior of a ferritic superalloy. Metall Mater Trans A 2012;43:1497–508.
[56] Huang S, Ghosh G, Li X, Ilavsky J, Teng ZK, Liaw PK. Effect of Al on the NiAl-type B2 Precipitates in Ferritic Superalloys. Metall Mater Trans A 2012;43:3423–7.
[57] Teng ZK, Ghosh G, Miller MK, Huang S, Clausen B, Brown DW, et al. Neutron-diffraction study and modeling of the lattice parameters on a NiAl-precipitate strengthened Fe-based alloy. Acta Mater 2012;60:5362–9.
[58] Teng ZK, Zhang F, Miller MK, Liu CT, Huang S, Chou YT, et al. New NiAl-strengthened ferritic steels with balanced creep resistance and ductility, designed by coupling thermodynamic calculations with focused experiments. Intermetallics 2012;29:110–5.
[59] Ding H, Huang S, Ghosh G, Liaw PK, Asta M. A Computational Study of ImpurityDiusivities for 5d Transition Metal Solutes in -Fe. Scripta Mater 2012;67:732–5.
[60] Miao WF, Laughlin DE. Precipitation hardening in aluminum alloy 6022. Scripta Mater 1999;40:7.
[61] Deligianni DD, Katsala N, Ladas S, Sotiropoulou D, Amedee J, Missirlis YF. Effect of surface roughness of the titanium alloy Ti–6Al–4V on human bone marrow cell response and on protein adsorption. Biomaterials 2001;22:1241–51.
[62] Aoki K. Ductilization of L12 intermetallic compound Ni_3Al by microalloying with boron. Mater Trans, JIM 1990;31:443–8.
[63] Sun C, Guo JT, Tan M, Li H, Wang S. Effect of Cr and Nb on microstructures and mechanical properties of Fe_3Al alloys. Acta Metall Sin 1993;6:157–60.
[64] Kuc D, Bednarczyk I, Niewieski G. The influence of deformation on the plasticity and structure of Fe_3Al–5Cr alloy. J Achiev Mater Manuf Eng 2007;22:27–30.
[65] Inoue A. Stabilization of metallic supercooled liquid and bulk amorphous alloys. Acta Mater 2000;48:279–306.
[66] Johnson WL. Bulk glass-forming metallic alloys: science and technology. MRS Bull 1999:24.
[67] Wang WH, Dong C, Shek CH. Bulk metallic glasses. Mater Sci Eng R 2004;44:45–89.
[68] Schuh CA, Hufnagel TC, Ramamurty U. Mechanical behavior of amorphous alloys. Acta Mater 2007;55:4067–109.
[69] Miller MK, Liaw PK. Bulk metallic glasses. New York: Springer; 2007.
[70] Huang R, Suo Z, Prevost JH, Nix WD. Inhomogeneous deformation in metallic glasses. J Mech Phys Solids 2002;50:1011–27.
[71] Yu HB, Wang WH, Bai HY, Wu Y, Chen MW. Relating activation of shear transformation zones to relaxations in metallic glasses. Phys Rev B 2010;81:220201R.
[72] Trexler MM, Thadhani NN. Mechanical properties of bulk metallic glasses. Prog Mater Sci 2010;55:759–839.
[73] Vitek V, Egami T. Atomic level stresses in solids and liquids. Phys Status Solidi B 1987;144:145–56.
[74] Egami T. Atomic level stresses. Prog Mater Sci 2011;56:637–53.
[75] Schroers J. Processing of bulk metallic glass. Adv Mater 2010;22:1566–97.
[76] Hofmann DC, Suh JY, Wiest A, Duan G, Lind ML, Demetriou MD, et al. Designing metallic glass matrix composites with high toughness and tensile ductility. Nature 2008;451:1085–9.
[77] Qiao JW, Sun AC, Huang EW, Zhang Y, Liaw PK, Chuang CP. Tensile deformation micromechanisms for bulk metallic glass matrix composites: from work-hardening to softening. Acta Mater 2011;59:4126–37.
[78] Qiao JW, Zhang Y, Jia HL, Yang HJ, Liaw PK, Xu BS. Tensile softening of metallic-glass-matrix composites in the supercooled liquid region. Appl Phys Lett 2012;100. 121902-4.
[79] Wang FJ, Zhang Y, Chen GL, Davies HA. Tensile and compressive mechanical behavior of a $CoCrCuFeNiAl_{0.5}$ high entropy alloy. Int J Mod Phys B 2009;23:1254–9.
[80] Oliver WC, Pharr GM. An improved technique for determining hardness and elastic modulus using load and displacement sensing indentation experiments. J Mater Res 1992;7:1564–83.
[81] Guo W, Dmowski W, Noh JY, Rack P, Liaw PK, Egami T. Local Atomic Structure of a High-entropy Alloy: An X-ray and neutron scattering study. Metall Mater Trans A 2013;44:1994–7.
[82] Kao SW, Yeh JW, Chin TS. Rapidly solidified structure of alloys with up to eight equal-molar elements – a simulation by molecular dynamics. J Phys – Condens Matter 2008:20.
[83] Grosso MF, Bozzolo G, Mosca HO. Modeling of high entropy alloys of refractory elements. Physica B 2012;407(16):3285–7.
[84] Hill TL. An introduction to statistical thermodynamics. New York: Dover Publications Inc; 1986.
[85] Gearhart CA. Einstein before 1905: the early papers on statistical mechanics. Am J Phys 1990;58(5):468–80.
[86] Ruffa AR. Thermal potential, mechanical instability, and melting entropy. Phys Rev B 1982;25(9):5895–900.
[87] Oriani RA. Thermodynamics of metallic solutions. Adv Chem Phys 2007;2:119–46.
[88] Takeuchi A, Inoue A. Calculations of mixing enthalpy and mismatch entropy for ternary amorphous alloys. Mater Trans, JIM 2000;41(11):1372–8.
[89] Takeuchi A, Inoue A. Quantitative evaluation of critical cooling rate for metallic glasses. Mater Sci Eng, A 2001;304–306:446–51.
[90] Guo S, Liu CT. Phase stability in high entropy alloys: formation of solid-solution phase or amorphous phase. Prog Nat Sci: Mater Int 2012;21:433–46.

[91] Miracle DB, Sander WS, Senkov ON. The influence of efficient atomic packing on the constitution of metallic glasses. Philos Mag 2003;83(20):2409–28.
[92] Takeuchi A, Inoue A. Classification of bulk metallic glasses by atomic size difference, heat of mixing and period of constituent elements and its application to characterization of the main alloying element. Mater Trans 2005;46(12):2817–29.
[93] Ren B, Liu ZX, Li DM, Shi L, Cai B, Wang MX. Effect of elemental interaction on microstructure of CuCrFeNiMn high entropy alloy system. J Alloy Compd 2010;493:148–53.
[94] Zhang KB, Fu Z. Effects of annealing treatment on phase composition and microstructure of $CoCrFeNiTiAl_x$ high-entropy alloys. Intermetallics 2012;22:24–32.
[95] Hume-Rothery W, Smallman RE, Haworth CW. The structure of metals and alloys. The Institute of Metals, 1 Carlton House Terrace, London SW1Y 5DB, UK, 1988.
[96] Gschneidner KA, Subramanian PR. In: Massalski TB, editor. Binary alloy phase diagrams. Metals Park (OH): ASM; 1986.
[97] Guo S, Ng C, Lu J, Liu CT. Effect of valence electron concentration on stability of fcc or bcc phase in high entropy alloys. J Appl Phys 2011;109:103505.
[98] Wilke CR, Chang P. Correlation of diffusion coefficients in dilute solutions. AIChE J 1955;1:264–70.
[99] Chen YY, Duval T, Hung UD, Yeh JW, Shih HC. Microstructure and electrochemical properties of high entropy alloys—a comparison with type-304 stainless steel. Corros Sci 2005;47(9):2257–79.
[100] Tsai CW, Tsai MH, Yeh JW, Yang CC. Effect of temperature on mechanical properties of $Al_{0.5}CoCrCuFeNi$ wrought alloy. J Alloy Compd 2010;490(1–2):160–5.
[101] Distanov VE, Nenashev BG, Kirdyashkin AG, Serboulenko MG. Proustite single-crystal growth by the Bridgman-Stockbarger method using ACRT. J Cryst Growth 2002;235:457–64.
[102] Volza MP, Schweizerb M, Kaiserc N, Cobba SD, Vujisicd L, Motakefd S, et al. Bridgman growth of detached GeSi crystals. J Cryst Growth 2002;237–239:1844–8.
[103] Walkera JS, Henry D, BenHadid H. Magnetic stabilization of the Buoyant convection in the liquid-encapsulated Czochralski process. J Cryst Growth 2002;243:108–16.
[104] Li X, Fautrelle Y, Ren ZM. Influence of an axial high magnetic field on the liquid–solid transformation in Al–Cu hypoeutectic alloys and on the microstructure of the solid. Acta Mater 2007;55(4):1377–86.
[105] Zhang Y, Ma SG, Qiao JW. Morphology transition from dendrites to equiaxed grains for AlCoCrFeNi high-entropy alloys by copper mold casting and Bridgman solidification. Metall Mater Trans A 2011;43(8):2625–30.
[106] Zhang Y. Processing and properties of high entropy alloys. TMS 2011 anual meeting and exhibition 2011. Invited presentation.
[107] Wang LM, Chen CC, Yeh JW, Ke ST. The microstructure and strengthening mechanism of thermal spray coating $Ni_xCo_{0.6}Fe_{0.2}Cr_ySi_zAlTi_{0.2}$ high-entropy alloys. Mater Chem Phys 2011;126:880–5.
[108] http://www.tsetinc.com/ceramicoat.htm.
[109] https://wwwliaorg/laserinsights/tag/laser-cladding/.
[110] Zhang H, Pan Y, He Y. Effects of annealing on the microstructure and properties of 6FeNiCoCrAlTiSi high-entropy alloy coating prepared by laser cladding. J Therm Spray Technol 2011;20(5):1049–55.
[111] https://www.lia.org/blog/2011/05/high-performance-laser-cladding/#more-1035.
[112] Schnell A, Kurz W. Epitaxial deposition of MCrAlY coatings on a Ni-base superalloy by laser cladding. Scripta Mater 2003;49:705–9.
[113] Man HC, Zhang S, Cheng FT, Yue TM. Microstructure and formation mechanism of in situ syntheiszed TiC/Ti surface MMC on Ti–6Al–4V by laser cladding. Scripta Mater 2001;44:2801–7.
[114] Suryanarayana C. Mechanical alloying and milling. Prog Mater Sci 2001;46:1–184.
[115] Murty BS, Ranganathan S. Novel materials synthesis by mechanical alloying milling. Int Mater Rev 1998;43(3):101–41.
[116] http://what-when-how.com/materialsparts-and-finishes/mechanical-alloying/.
[117] Chen YL, Tsai CW, Juan CC, Chuang MH, Yeh JW, Chin TS, et al. Amorphization of equimolar alloys with HCP elements during mechanical alloying. J Alloy Compd 2010;506:210–5.
[118] Weeber AW, Bakker H, Heijligers HJM, Bastin GF. Compositional analysis of NiZr powder during amorphization by mechanical alloying. Europhys Lett 1987;3(12):1261–5.
[119] Zhou GF, Bakker H. Influence of mechanical milling on magnetic properties of intermetallic compounds. Mater Trans, JIM 1995;36(2):329–40.
[120] Varalakshmi S, Kamaraj M, Murty BS. Formation and stability of equiatomic and nonequiatomic nanocrystalline CuNiCoZnAlTi high-entropy alloys by mechanical alloying. Metall Mater Trans A 2010;41A:2703–9.
[121] Chang SY, Lin SY, Huang YC, Wu CL. Mechanical properties, deformation behaviors and interface adhesion of $(AlCrTaTiZr)N_x$ multi-component coatings. Surf Coat Technol 2010;204:3307–14.
[122] Dolique V, Thomann AL, Brault P. High-entropy alloys deposited by magnetron sputtering. IEEE Trans Plasma Sci 2011;39(11):2478–9.
[123] http://www.tcbonding.com/sputtering.html.
[124] Lin MI, Tsai MH, Shen WJ, Yeh JW. Evolution of structure and properties of multi-component $(AlCrTaTiZr)O_x$ films. Thin Solid Films 2010;518:2732–7.
[125] Yao CZ, Zhang P, Liu M, Li GR, Ye JQ, Liu P, et al. Electrochemical preparation and magnetic study of Bi–Fe–Co–Ni–Mn high entropy alloy. Electrochim Acta 2008;53:8359–65.
[126] Senkov ON, Scott JM, Senkova SV, Miraclea DB, Woodward CF. Microstructure and room temperature properties of a high-entropy TaNbHfZrTi alloy. J Alloy Compd 2011;509:6043–8.
[127] Senkov ON, Woodward CF. Microstructure and properties of a refractory $NbCrMo_{0.5}Ta_{0.5}TiZr$ alloy. Mater Sci Eng, A 2011;529:311–20.
[128] Senkov ON, Scott J, Senkova S, Meisenkothen F, Miracle D, Woodward C. Microstructure and elevated temperature properties of a refractory TaNbHfZrTi alloy. J Mater Sci 2012;47(9):4062–74.
[129] Wang FJ, Zhang Y, Chen GL, Davies HA. Cooling rate and size effect on the microstructure and mechanical properties of AlCoCrFeNi high entropy alloy. J Eng Mater Technol 2009;131:034501–3.

[130] Tong CJ, Chen MR, Chen SK, Yeh JW, Shun TT, Lin SJ, et al. Mechanical performance of the $Al_xCoCrCuFeNi$ high-entropy alloy system with multiprincipal elements. Metall Mater Trans A 2005;36:1263–71.
[131] Kuznetsov AV, Shaysultanov DG, Stepanov ND, Salishchev GA, Senkov ON. Tensile properties of an AlCrCuNiFeCo high-entropy alloy in As-cast and wrought conditions. Mater Sci Eng, A 2012;533:107–18.
[132] Shun TT, Du YC. Microstructure and tensile behaviors of FCC $Al_{0.3}CoCrFeNi$ high entropy alloy. J Alloy Compd 2009;479(1–2):157–60.
[133] Zhu JM, Fu HM, Zhang HF, Wang AM, Li H, Hu ZQ. Microstructures and compressive properties of multicomponent $AlCoCrFeNiMo_x$ alloys. Mater Sci Eng, A 2010;527(26):6975–9.
[134] Zhu JM, Fu HM, Zhang HF, Wang AM, Li H, Hu ZQ. Microstructure and compressive properties of multiprincipal component $AlCoCrFeNiC_x$ alloys. J Alloy Compd 2011;509(8):3476–80.
[135] Ma SG, Zhang Y. Effect of Nb addition on the microstructure and properties of AlCoCrFeNi high entropy alloys. Mater Sci Eng, A 2012;532:480–6.
[136] Zhou YJ, Zhang Y, Kim TN, Chen GL. Microstructure characterizations and strengthening mechanism of multi-principal component $AlCoCrFeNiTi_{0.5}$ solid solution alloy with excellent mechanical properties. Mater Lett 2008;62:2673–6.
[137] Qiao JW, Ma SG, Huang EW, Chuang CP, Liaw PK, Zhang Y. Microstructural characteristics and mechanical behaviors of AlCoCrFeNi high-entropy alloys at ambient and cryogenic temperatures. Mater Sci Forum 2011;688:419–25.
[138] Laktionova MA, Tabchnikova ED, Tang Z, Liaw PK. Mechanical properties of the high-entropy alloy Ag0.5CoCrCuFeNi at temperatures of 4.2-300 K. Low Temp Phys 2013;39:630–2.
[139] Hemphill MA, Yuan T, Wang GY, Yeh JW, Tsai CW, Chuang A, et al. Fatigue behavior of $Al_{0.5}CoCrCuFeNi$ high-entropy alloys. Acta Mater 2012;60(16):5723–34.
[140] Chuang MH, Tsai MH, Wang WR, Lin SJ, Yeh JW. Microstructure and wear behavior of $Al_xCo_{1.5}CrFeNi_{1.5}Ti_y$ high-entropy alloys. Acta Mater 2011;59:6308–17.
[141] Wu JM, Lin SJ, Yeh JW, Chen SK, Huang YS. Adhesive wear behavior of $Al_xCoCrCuFeNi$ high-entropy alloys as a function of aluminum content. Wear 2006;261:513–9.
[142] Zhang KB, Fu ZY, Zhang JY, Shi J, Wang WM, Wang H, et al. Annealing on the structure and properties evolution of the CoCrFeNiCuAl high-entropy alloy. J Alloy Compd 2010;502:295–9.
[143] Chen SK, Kao YF. Near-constant resistivity in 4.2–360 K in a B2 $Al_{2.08}CoCrFeNi$. AIP Adv 2012;2(1). 012111-5.
[144] Chou HP, Chang YS, Chen SK, Yeh JW. Microstructure, thermophysical and electrical properties in $Al_xCoCrFeNi$ ($0 \leqslant x \leqslant 2$) high-entropy alloys. Mater Sci Eng B – Adv Funct Solid-State Mater 2009;163(3):184–9.
[145] Yang X, Zhang Y. Cryogenic resistivities of $NbTiAlVTaLa_x$, CoCrFeNiCu and CoCrFeNiAl high entropy alloys. Adv Mater Process 2010:51–4.
[146] Kao YF, Chen SK, Chen TJ, Chu PC, Yeh JW, Lin SJ. Electrical, magnetic, and hall properties of $Al_xCoCrFeNi$ high-entropy alloys. J Alloy Compd 2011;509(5):1607–14.
[147] Lucas MS, Mauger L, Munoz JA, Xiao Y, Sheets AO, Semiatin SL, et al. Magnetic and vibrational properties of high-entropy alloys. J Appl Phys 2011;109(7):07E307.
[148] Singh S, Wanderka N, Kiefer K, Siemensmeyer K, Banhart J. Effect of decomposition of the Cr–Fe–Co rich phase of AlCoCrCuFeNi high entropy alloy on magnetic properties. Ultramicroscopy 2011;111(6):619–22.
[149] Braic V, Balaceanu M, Braic M, Vladescu A, Panseri S, Russo A. Characterization of multi-principal-element (TiZrNbHfTa)N and (TiZrNbHfTa)C coatings for biomedical applications. J Mech Behav Biomed Mater 2012;10:197–205.
[150] Lee CP, Chen YY, Hsu CY, Yeh JW, Shih HC. The effect of boron on the corrosion resistance of the high entropy alloys $Al_{0.5}CoCrCuFeNiB_x$. J Electrochem Soc 2007;154(8):C424–30.
[151] Chen ST, Tang WY, Kuo YF, Chen SY, Tsau CH, Shun TT, et al. Microstructure and properties of age-hardenable $Al_xCrFe_{1.5}MnNi_{0.5}$ alloys. Mater Sci Eng, A 2010;527:5818–25.
[152] Tsao LC, Chen CS, Chu CP. Age hardening reaction of the $Al_{0.3}CrFe_{1.5}MnNi_{0.5}$ high entropy alloy. Mater Des 2012;36:854–8.
[153] Tsai MH, Wang CW, Tsai CW, Shen WJ, Yeh JW, Gan JY, et al. Thermal stability and performance of NbSiTaTiZr high-entropy alloy barrier for copper metallization. J Electrochem Soc 2011;158(11):H1161–5.
[154] Chang SY, Chen MK, Chen DS. Multiprincipal-element AlCrTaTiZr-nitride nanocomposite film of extremely high thermal stability as diffusion barrier for Cu metallization. J Electrochem Soc 2009;156(5):G37–42.
[155] Sethna JP, Dahmen KA, Myers CR. Crackling noise. Nature 2001;410:242–50.
[156] Dahmen KA, Ben-Zion Y, Uhl JT. Micromechanical model for deformation in solids with universal predictions for stress–strain curves and slip avalanches. Phys Rev Lett 2009;102:175501.
[157] Dahmen KA, Ben-Zion Y. The physics of jerky motion in slowly driven magnetic and earthquake fault systems. Encyclopedia of Complexity and System Science 2009;5:5021–37.
[158] Carpenter JH, Dahmen KA. Barkhausen noise and critical scaling in the demagnetization curve. Phys Rev B 2003;67:020412.
[159] Carpenter JH, Dahmen KA, Mills AC, Weissman MB, Berger A, Hellwig O. History-induced critical behavior in disordered systems. Phys Rev B 2005;72:052410.
[160] White RA, Dahmen KA. Driving rate effects on crackling noise. Phys Rev Lett 2003;91(8):085702.
[161] Zaiser M. Scale invariance in plastic flow of crystalline solids. Adv Phys 2006;55(1–2):185–245.
[162] Miguel MC, Vespignani A, Zapperi S, Weiss J, Grasso JR. Intermittent dislocation flow in viscoplastic deformation. Nature 2001;410(6829):667–71.
[163] Weiss J, Grasso JR, Miguel MC, Vespignani A, Zapperi S. Complexity in dislocation dynamics: experiments. Mater Sci Eng, A 2001;309–310:360–4.
[164] Richeton T, Dobron P, Chmelik F, Weiss J, Louchet F. On the critical character of plasticity in metallic single crystals. Mater Sci Eng, A 2006;424(1–2):190–5.
[165] Richeton T, Weiss J, Louchet F. Dislocation avalanches: role of temperature, grain size and strain hardening. Acta Mater 2005;53(16):4463–71.
[166] Weiss J Lahaie F, Grasso JR. Statistical analysis of dislocation dynamics during viscoplastic deformation from acoustic emission. J Geophys Res 2000;105(B1):433–42.

[167] Dimiduk DM, Woodward C, LeSar R, Uchic MD. Scale-free intermittent flow in crystal plasticity. Science 2006;312(5777):1188–90.
[168] Brinckmann S, Kim JY, Greer JR. Fundamental differences in mechanical behavior between two types of crystals at the nanoscale. Phys Rev Lett 2008;100(15):155502.
[169] Greer JR, De Hosson JTM. Plasticity in small-sized metallic systems: intrinsic versus extrinsic size effect. Prog Mater Sci 2011;56(6):654–724.
[170] Uchic MD, Shade PA, Dimiduk DM. Plasticity of micrometer-scale single crystals in compression. Annu Rev Mater Res 2009;39(1):361–86.
[171] Kraft O, Gruber PA, Mönig R, Weygand D. Plasticity in confined dimensions. Annu Rev Mater Res 2010;40(1):293–317.
[172] Ngan AHW, Ng KS. Transition from deterministic to stochastic deformation. Philos Mag 2010;90(14):1937–54.
[173] Zaiser M, Schwerdtfeger J, Schneider AS, Frick CP, Clark BG, Gruber PA, et al. Strain bursts in plastically deforming molybdenum micro- and nanopillars. Philos Mag 2008;88(30–32):3861–74.
[174] Kim JY, Greer JR. Tensile and compressive behavior of gold and molybdenum single crystals at the nano-scale. Acta Mater 2009;57(17):5245–53.
[175] Kim JY, Jang D, Greer JR. Tensile and compressive behavior of tungsten, molybdenum, tantalum and niobium at the nanoscale. Acta Mater 2010;58(7):2355–63.
[176] Weinberger CR, Cai W. Surface-controlled dislocation multiplication in metal micropillars. Proc Natl Acad Sci 2008;105(38):14304–7.
[177] Dehm G. Miniaturized single-crystalline FCC metals deformed in tension: new insights in size-dependent plasticity. Prog Mater Sci 2009;54(6):664–88.
[178] Friedman N, Jennings AT, Tsekenis G, Kim JY, Tao M, Uhl JT, et al. Statistics of dislocation slip avalanches in nanosized single crystals show tuned critical behavior predicted by a simple mean field model. Phys Rev Lett 2012;109:095507.
[179] Dahmen KA, Ben-Zion Y, Uhl JT. A simple analytic theory for the statistics of avalanches in sheared granular materials. Nat Phys 2011;7:554–7.
[180] Petri A, Baldassarri A, Dalton F, Pontuale G, Pietronero L, Zapperi S. Stochastic dynamics of a sheared granular medium. Eur Phys J B 2008;64:531–5.
[181] Baldassarri A, Dalton F, Petri A, Zapperi S, Pontuale G, Pietronero L. Brownian forces in sheared granular matter. Phys Rev Lett 2006;96:118002.
[182] Hartley R. PhD thesis, Physics, Duke University; 2005.
[183] Daniels KE, Hayman NW. Force chains in seismogenic faults visualized with photoelastic granular shear experiments. J Geophys Res 2008;113:B11411.
[184] Aharonov E, Sparks D. Shear profiles and localization in simulations of granular materials. Phys Rev E 2002;65:051302.
[185] Sun BA, Yu HB, Jiao W, Bai HY, Zhao DQ, Wang WH. Plasticity of ductile metallic glasses: a self-organized critical state. Phys Rev Lett 2010;105(3):035501.
[186] Kim JY, Gu X, Wraith M, Uhl JT, Dahmen KA, Greer JR. Suppression of catastrophic failure in metallic glass–polyisoprene nanolaminate containing nanopillars. Adv Funct Mater 2012;22(9):1972–80.
[187] Antonaglia J, Liaw PK, Dahmen KA, in preparation.
[188] Ortín J, Ràfols I, Carrillo L, Goicoechea J, Vives E, Mañosa L, et al. Experiments and models of avalanches in martensites. J Phys IV 1995;5. C8209–14.
[189] Qiao JW, Yang FQ, Wang GY, Liaw PK, Zhang Y. Jerky-flow characteristics for a Zr-based bulk metallic glass. Scripta Mater 2010;63:1081–4.
[190] Qiao JW, Zhang Y, Liaw PK. Serrated flow kinetics in a Zr-based bulk metallic glass. Intermetallics 2010;18:2057–64.
[191] Zhang Y, Zhang WG, Lin JP, Hao GJ, Chen GL, Liaw PK. Glass-forming ability and competitive crystalline phases for lightweight Ti–Be-based alloys. Metall Mater Trans A 2010;41:1670–6.
[192] Qiao JW, Wang S, Zhang Y, Liaw PK, Chen GL. Large plasticity and tensile necking of Zr-based bulk-metallic-glass-matrix composites synthesized by the Bridgman solidification. Appl Phys Lett 2009;94:151905.
[193] Willcox M, Mysak T. An introduction to Barkhausen noise and its applications. Insight NDT; 2004.
[194] Zaiser M, Marmo B, Moretti P. The 'yielding transition' in crystal plasticity – discrete dislocations and continuum models. In: International conference on statistical mechanics of plasticity and related instabilities; 2005.
[195] Miguel MC, Vespignani A, Zapperi S, Weiss J, Grasso JR. Complexity in dislocation dynamics: model. Mater Sci Eng, A 2001;309–310:324–7.
[196] Laurson L, Alava MJ. 1/*f* Noise and avalanche scaling in plastic deformation. Phys Rev E 2006;74(6):066106.
[197] Csikor FF, Motz C, Weygand D, Zaiser M, Zapperi S. Dislocation avalanches, strain bursts, and the problem of plastic forming at the micrometer scale. Science 2007;318(12):251–4.
[198] Ispanovity PD, Groma I, Györgyi G, Csikor FF, Weygand D. Submicron plasticity: yield stress, dislocation avalanches, and velocity distribution. Phys Rev Lett 2010;105:085503.
[199] Tsekenis G, Goldenfeld N, Dahmen KA. Dislocations jam at any density. Phys Rev Lett 2011;106:105501.
[200] Tsekenis G, Uhl JT, Goldenfeld N, Dahmen KA. Determination of the universality class of crystal plasticity. Europhysics Letters 2013;101:36003.
[201] Koslowski M. Scaling laws in plastic deformation. Philos Mag 2007;87(8–9):1175–84.
[202] Chan PY, Tsekenis G, Dantzig J, Dahmen KA, Goldenfeld N. Plasticity and dislocation dynamics in a phase field crystal model. Phys Rev Lett 2010;105:015502.
[203] Dahmen K, Ertaş D, Ben-Zion Y. Gutenberg-Richter and characteristic earthquake behavior in simple mean-field models of heterogeneous faults. Phys Rev E 1998;58(2):1494–501.
[204] Dubois JM. Complex metallic alloys: clarity through complexity. Nat Mater 2010;9:287–8.
[205] Lebyodkin MA, Kobelev NP, Bougherira Y, Entemeyer D, Fressengeas C, Lebedkina TA, et al. On the similarity of plastic flow processes during smooth and jerky flow in dilute alloys. Acta Mater 2012;60(3):844–50.
[206] Vinogradov A, Lazarev A. Continuous acoustic emission during intermittent plastic flow in alpha-brass. Scripta Mater 2012;66(10):745–8.

[207] Cui C, Jin T, Sun X. Effects of heat treatments on the serrated flow in a Ni–Co–Cr-base superalloy. J Mater Sci 2011;46(16):5546–52.
[208] Hale CL, Rollings WS, Weaver ML. Activation energy calculations for discontinuous yielding in Inconel 718SPF. Mater Sci Eng, A 2001;300(1–2):153–64.
[209] De Cooman BC, Kim J, Lee S. Heterogeneous deformation in twinning-induced plasticity steel. Scripta Mater 2012;66(12):986–91.
[210] Song SX, Nieh TG. Direct measurements of shear band propagation in metallic glasses – an overview. Intermetallics 2011;19(12):1968–77.
[211] Rice JR. The localization of plastic deformation. North-Holland Publishing Company; 1976. p. 207–20.
[212] Klement W, Willens RH, Duwez POL. Non-crystalline structure in solidified gold–silicon alloys. Nature 1960;187(4740):869–70.
[213] Zhang Y, Tan H, Kong HZ, Yao B, Li Y. Glass forming ability of Pr–(Cu, Ni)–Al alloys in eutectic system. J Mater Res 2003;18(3):664–71.
[214] Li Y, Poon SJ, Shiflet GJ, Xu J, Kim DH, Loeffler JF. Formation of bulk metallic glasses and their composites. MRS Bull 2007;32:624–8.
[215] Li Y. Bulk metallic glasses: eutectic coupled zone and amorphous formation. JOM 2005(March):60–3.
[216] Zhang Y, Zhao DQ, Wei BC, Wen P, Pan MX, Wang WH. Formation and properties of $Zr_{48}Nb_8Fe_8Cu_{12}Be_{24}$ bulk metallic glass. J Mater Res 2001;16(6):1675–9.
[217] Zhang Y, Zhao DQ, Wang RJ, Wang WH. Formation and properties of $Zr_{48}Nb_8Cu_{14}Ni_{12}Be_{18}$ bulk metallic glass. Acta Mater 2003;51:1971–9.
[218] Tan H, Zhang Y, Ma D, Feng YP, Li Y. Optimum glass formation at off-eutectic composition and its relation to skewed eutectic coupled zone in the La based La–Al–(Cu, Ni) pseudo ternary system. Acta Mater 2003;51:4551–61.
[219] Tan H, Zhang Y, Feng YP, Li Y. Synthesis of a La-based bulk metallic glass matrix composite. Philos Mag Lett 2004;84(1):53–61.
[220] Zhang Y, Tan H, Li Y. Bulk glass formation of 12 mm rod in La–Cu–Ni–Al alloys. Mater Sci Eng, A 2004;375–377:436–9.
[221] Jing Q, Zhang Y, Wang D, Li Y. A study of the glass forming ability in ZrNiAl alloys. Mater Sci Eng, A 2006;441:106–11.
[222] Turnbull D. Under what conditions can a glass be formed? Contemp Phys 1969;10(5):473–88.
[223] Kim KB, Warren PJ, Cantor B, Eckert J. Structural evolution of nano-scale icosahedral phase in novel multicomponent amorphous alloys. Philos Mag 2006;86:281–6.
[224] Boettinger WJ. Growth kinetic limitations during rapid solidification. Rapidly solidified amorphous and crystalline alloys. In: Proceedings of the materials research society annual meeting; 1982.
[225] Li Y, Guo Q, Kalb JA, Thompson CV. Matching glass-forming ability with density of amorphous phase. Science 2008;322:1816–9.
[226] Mihalkovic M, Widom M. Ab initio calculations of cohensive energies of Fe-based glass-forming alloys. Phys Rev B 2004;70. 1441071-12.
[227] Greer AL, Ma E. Bulk metallic glasses: at the cutting edge of metals research. MRS Bull 2007;32:611–9.
[228] Busch R, Schroers J, Wang WH. Thermodynamics and kinetics of bulk metallic glass. MRS Bull 2007;32(8):620–3.
[229] Zhang T, Li R, Pang SJ. Effect of similar elements on improving glass-forming ability of La–Ce-based alloys. J Alloy Compd 2009;483:60–3.
[230] Li R, Pang SJ, Men H, Ma CL, Zhang T. Formation and mechanical properties of (Ce–La–Pr–Nd)–Co–Al bulk glassy alloys with super glass-forming ability. Scripta Mater 2006;54:1123–6.
[231] Kim KB, Warren PJ, Cantor B. Glass-forming ability of novel multicomponent $(Ti_{33}Zr_{33}Hf_{33})$–$(Ni_{50}Cu_{50})$–Al alloys developed by equiatomic substitution. Mater Sci Eng, A 2004;375–377:317–21.
[232] Kim KB. Devitrification of nano-scale icosahedral phase in $(Ti_{0.33}Zr_{0.33}Hf_{0.33})_{50}(Ni_{0.5}Cu_{0.5})_{40}Al_{10}$ alloy with enlarging supercooled liquid region. Mater Lett 2005;59:1771–4.
[233] Kim KB, Warren PJ, Cantor B. Metallic glass formation in multicomponent (Ti, Zr, Hf, Nb)–(Ni, Cu, Ag)–Al alloys. J Non-Cryst Solids 2003;317:17–22.
[234] Zhang LC, Xu J. Glass forming ability of melt-spun multicomponent (Ti, Zr, Hf)–(Cu, Ni, Co)–Al alloys with equiatomic substitution. J Non-Cryst Solids 2004;347:166–72.
[235] Kim KB, Zhang Y, Warren PJ, Cantor B. Crystallization behavior in a new multicomponent $Ti_{16.6}Zr_{16.6}Hf_{16.6}Ni_{20}Cu_{20}Al_{10}$ metallic glass developed by equiatomic substitution technique. Philos Mag 2003;83(20):2371–81.
[236] Kim KB, Warren PJ, Cantor B. Formation of metallic glasses in novel $(Ti_{33}Zr_{33}Hf_{33})_{100-x-y}(Ni_{50}Cu_{50})_xAl_y$ alloys. Mater Trans 2003;44(3):411–3.
[237] Kim KB, Yi S, Hwang IS, Eckert J. Effect of cooling rate on microstructure and glass-forming ability of a $(Ti_{33}Zr_{33}Hf_{33})_{70}(Ni_{50}Cu_{50})_{20}Al_{10}$ alloy. Intermetallics 2006;14:972–7.
[238] Zhang LC, Kim KB, Yu P, Zhang WY, Kunz U, Eckert J. Amorphization in mechanically alloyed (Ti, Zr, Nb)–(Ni, Cu)–Al equiatomic alloys. J Alloy Compd 2007;428:157–63.
[239] Kim KB, Warren PJ, Cantor B. Structural relaxation and glass transition behavior of novel $(Ti_{33}Zr_{33}Hf_{33})_{50}(Ni_{50}Cu_{50})_{40}Al_{10}$ alloy developed by equiatomic substitution. J Non-Cryst Solids 2007;353:3338–41.
[240] Basu J, Ranganathan S. Glass forming ability and stability of ternary Ni-early transition metal (Ti/Zr/Hf) alloys. Acta Mater 2008;56:1899–907.
[241] Zhang Y, Cantor B, Kim KB, Warren PJ. Crystallization behaviour in a new multicomponent $Ti_{16.6}Zr_{16.6}Hf_{16.6}Ni_{20}Cu_{20}Al_{10}$ metallic glass developed by the equiatomic substitution technique. Philos Mag 2003;83:2371–81.
[242] Kim KB, Warren PJ, Cantor B, Eckert J. Crystallization behaviour of novel $(Ti_{33}Zr_{33}Hf_{33})_{100-x}(Ni_{50}Cu_{50})_x$ alloys with $X = 48$ to 55. J Metastable Nanocryst Mater 2005;24–25:657–60.
[243] Inoue A, Zhang T, Koshiba H, Makino A. New bulk amorphous Fe–(Co, Ni)–M–B (M = Zr, Hf, Nb, Ta, Mo, W) alloys with good soft magnetic properties. J Appl Phys 1998;83(11):6326–8.
[244] Zhang T, Inoue A. Bulk glassy alloys in (Fe, Co, Ni)–Si–B system. Mater Trans 2001;42(6):1015–8.
[245] Chen YY, Hong UT, Yeh JW, SHih HC. Mechanical properties of a bulk $Cu_{0.5}NiAlCoCrFeSi$ glassy alloy in 288 °C high purity water. Appl Phys Lett 2005;87:261918.

[246] Kim KB, Warren PJ, Cantor B, Eckert J. Enhanced thermal stability of the devitrified nanoscale icosahedral phase in novel multicomponent amorphous alloys. J Mater Res 2006;21:823–30.
[247] Zaddach AJ, Niu C, Koch C, Irving DL. Mechanical properties and stacking fault energies of NiFeCrCoMn high-entropy alloy. JOM 2013. http://dx.doi.org/10.1007/s11837-013-0771-4.
[248] Zhang C, Zhang F, Chen S, Cao W. Computational thermodynamics aided high-entropy alloy design. JOM 2012;64(7):839–45.
[249] Kohn W, Sham LJ. Self-consistent equations including exchange and correlation effects. Phys Rev 1965;140:A1133–8.
[250] Gao MC, Alman DE. Searching for next single-phase high-entropy alloy compositions. Entropy 2013;15(10):4504–19.
[251] Wei SH, Ferreira LG, Bernard JE, Zunger A. Electronic properties of random alloys: special quasirandom structures. Phys Rev B 1990;42(15):9622–49.
[252] Zunger A, Wei SH, Ferreira LG, Bernard JE. Special quasirandom structures. Phys Rev Lett 1990;65(3):353–6.
[253] Jiang C, Wolverton C, Sofo J, Chen LQ, Liu ZK. First-principles study of binary BCC alloys using special quasirandom structures. Phys Rev B 2004;69(21):214202.
[254] Jiang C, Wolverton C, Sofo J, Chen LQ, Liu ZK. First-principles study of constitutional point defects in B2 NiAl using special quasirandom structures. Acta Mater 2005;53(9):2643–52.
[255] Wang A et al. First-principles study of binary special quasirandom structures for the Al–Cu, Al–Si, Cu–Si, and Mg–Si systems. Calphad 2009;33(4):769–73.
[256] Jiang C. First-principles study of ternary BCC alloys using special quasi-random structures. Acta Mater 2009;57(16):4716–26.
[257] Shin D, Liu ZK. Enthalpy of mixing for ternary FCC solid solutions from special quasirandom structures. Calphad 2008;32(1):74–81.
[258] Jiang C. First-principles study of Co_3(Al, W) alloys using special quasi-random structures. Scripta Mater 2008;59(10):1075–8.
[259] Soven P. Coherent-potential model of substitutional disordered alloys. Phys Rev 1967;156(3):809–13.
[260] Stocks GM, Temmerman WM, Gyorffy BL. Complete solution of the Korringa-Kohn-Rostoker coherent-potential-approximation equations: Cu–Ni alloys. Phys Rev Lett 1978;41(5):339–43.
[261] Soven P. Application of the coherent potential approximation to a system of muffin-tin potentials. Phys Rev B 1970;2(12):4715–22.
[262] Abrikosov IA, Ruban AV, Johansson B, Skriver HL. Total energy calculations of random alloys: supercell, Connolly–Williams, and CPA methods. Comput Mater Sci 1998;10(1–4):302–5.
[263] Vitos L, Abrikosov IA, Johansson B. Anisotropic lattice distortions in random alloys from first-principles theory. Phys Rev Lett 2001;87(15):156401.
[264] Huang L, Vitos L, Kwon SK, Johansson B, Ahuja R. Thermoelastic properties of random alloys from first-principles theory. Phys Rev B 2006;73(10):104203.
[265] Zach R, Tobola J, Średniawa B, Kaprzyk S, Guillot M, Fruchart D, et al. Magnetic interactions in the $MnFe_{1-x}Co_xP$ series of solid solutions. J Phys: Condens Matter 2007;19(37):376201.
[266] Masuda-Jindo K, Hung VV, Hoa NT, Turchi PEA. First principles calculations of thermodynamic and mechanical properties of high temperature BCC Ta–W and Mo–Ta alloys. J Alloy Compd 2008;452(1):127–32.
[267] Hlil EK, Stadnyk Y, Gorelenko Y, Romaka L, Horyń A, Fruchart D. Synthesis, electronic transport and magnetic properties of $Zr_{1-x}Y_xNiSn$, (x = 0–0.25) solid solutions. J Solid State Chem 2010;183(3):521–6.
[268] Razumovskiy VI, Ruban AV, Korzhavyi PA. First-principles study of elastic properties of Cr- and Fe-rich Fe–Cr alloys. Phys Rev B 2011;84(2):024106.
[269] Li XQ, Zhang HL, Lu S, Li W, Zhao JJ, Johansson B, et al. Elastic properties of vanadium-based alloys from first-principles theory. Phys Rev B 2012;86(1):014105.
[270] Wang Y, Gao MC. An ab initio approach to the study of high entropy alloys. Unpublished work; 2012.
[271] Shang SL, Wang Y, Liu ZK. Thermodynamic fluctuations between magnetic states from first-principles phonon calculations: the case of BCC Fe. Phys Rev B 2010;82(1):014425.
[272] Ravelo R, Aguilar J, Baskes M, Angelo JE, Fultz B, Holian BL. Free energy and vibrational entropy difference between ordered and disordered Ni_3Al. Phys Rev B 1998;57(2):862–9.
[273] Fultz B. Vibrational thermodynamics of materials. Prog Mater Sci 2010;55(4):247–352.
[274] Muñoz JA, Lucas MS, Delaire O, Winterrose ML, Mauger L, Li CW, et al. Positive vibrational entropy of chemical ordering in FeV. Phys Rev Lett 2011;107(11):115501.
[275] Fultz B, Anthony L, Nagel LJ, Nicklow RM, Spooner S. Phonon densities of states and vibrational entropies of ordered and disordered Ni_3Al. Phys Rev B 1995;52(5):3315–21.
[276] Delaire O, Swan-Wood T, Fultz B. Negative entropy of mixing for vanadium–platinum solutions. Phys Rev Lett 2004;93:185704.
[277] Grimvall G. Thermophysical properties of materials. Amsterdam: North-Holland Publishing Company; 1999.
[278] Kresse G. Ab initio molecular dynamics for liquid metals. J Non-Cryst Solids 1995;192–193:222–9.
[279] Hass KC, Schneider WF, Curioni A, Andreoni W. First-principles molecular dynamics simulations of H_2O on α-Al_2O_3 (0001). J Phys Chem B 2000;104(23):5527–40.
[280] Alfe D, Gillan MJ, Price GD. Ab initio chemical potentials of solid and liquid solutions and the chemistry of the Earth's core. J Chem Phys 2002;116(16).
[281] Zhang Y, Guo G. Partitioning of Si and O between liquid iron and silicate melt: a two-phase ab-initio molecular dynamics study. Geophys Res Lett 2009:36.
[282] Calderin L, Gonzalez DJ, Gonzalez LE, Lopez JM. Structural, dynamic, and electronic properties of liquid tin: an ab initio molecular dynamics study. J Chem Phys 2008;129(19).
[283] Ganesh P, Widom M. Ab initio simulations of geometrical frustration in supercooled liquid Fe and Fe-based metallic glass. Phys Rev B 2008;77(1).
[284] Sheng HW, Luo WK, Alamgir FM, Bai JM, Ma E. Atomic packing and short-to-medium-range order in metallic glasses. Nature 2006;439(7075):419–25.

[285] Ganesh P, Widom M. Liquid–liquid transition in supercooled silicon determined by first-principles simulation. Phys Rev Lett 2009;102:075701.
[286] Chang YA, Chen SL, Zhang F, Yan XY, Xie FY, Schmid-Fetzer R, et al. Phase diagram calculation: past, present and future. Prog Mater Sci 2004;49(3–4):313–45.
[287] Kattner U. The thermodynamic modeling of multicomponent phase equilibria. JOM 1997;49(12):14–9.
[288] Kaufman L. Computer calculation of phase diagrams. New York: Academic Press; 1970.
[289] Anthony L, Nagel LJ, Okamoto JK, Fultz B. Magnitude and origin of the difference in vibrational entropy between ordered and disordered Fe_[308]Al. Phys Rev Lett 1994;73(22):3034–7.
[290] Fultz B, Anthony L, Robertson JL, Nicklow RM, Spooner S, Mostoller M. Phonon modes and vibrational entropy of mixing in Fe–Cr. Phys Rev B 1995;52(5):3280–5.
[291] Bogdanoff PD, Swan-Wood TL, Fultz B. Phonon entropy of alloying and ordering of Cu–Au. Phys Rev B 2003;68(1):014301.
[292] Zhao JC. Combinatorial approaches as effective tools in the study of phase diagrams and composition–structure–property relationships. Prog Mater Sci 2006;51(5):557–631.
[293] Zhao JC. The diffusion-multiple approach to designing alloys. annual review of materials research; annual reviews. Palo Alto; 2005. p. 51–73.
[294] Gao MC, Unlu N, Shiflet GJ, Mihalkovic M, Widom M. Re-assessment of Al–Ce and Al–Nd systems integrated with first-principle energy calculations and critical experiments. Metall Mater Trans A 2005;36A:3269–79.
[295] Shang S, Liu ZJ, Liu ZK. Thermodynamic modeling of the Ba–Ni–Ti system. J Alloy Compd 2007;430(1–2):188–93.
[296] Zhou SH, Wang Y, Chen LQ, Liu ZK, Napolitano RE. Solution-based thermodynamic modeling of the Ni–Ta and Ni–Mo–Ta systems using first-principle calculations. Calphad 2009;33(4):631–41.
[297] Zhang LJ, Wang J, Du Y, Hu RX, Nash P, Lu XG, et al. Thermodynamic properties of the Al–Fe–Ni system acquired via a hybrid approach combining calorimetry, first-principles and CALPHAD. Acta Mater 2009;57(18):5324–41.
[298] Hu RX, Gao MC, Doğan ÖN, King P, Widom M. Thermodynamic modeling of the Pd–S system supported by first-principles calculations. Calphad 2010;34(3):324–31.
[299] Rollett AD, Lee SB, Campman R, Rohrer GS. Three-dimensional characterization of microstructure by electron back-scatter diffraction. Annual review of materials research; annual reviews. Palo Alto; 2007. p. 627–58.
[300] Robertson IM, Schuh CA, Vetrano JS, Browning N, Field DP, Jensen DJ, et al. Towards an integrated materials characterization toolbox. J Mater Res 2011;26(11):1341–83.
[301] Patala S, Mason JK, Schuh CA. Improved representations of misorientation information for grain boundary science and engineering. Prog Mater Sci 2012;57(8):1383–425.
[302] Qu Q, Xu J. Patent CN101554686-A.
[303] Chen K, Xu J, Zhai Q. Patent CN101590574-A; CN101590574-B.